A wave of WNT signalling balanced by secreted inhibitors controls primitive streak formation in micropattern colonies of human embryonic stem cells

Martyn I.[1,2], Brivanlou A.H.[1†], & Siggia E.D.[2,3†]

[1]Laboratory of Molecular Vertebrate Embryology
[2]Center for Studies in Physics and Biology,
The Rockefeller University, New York, NY 10065, USA
[3]Lead Contact
[†]Correspondence and requests for materials should be addressed to A.H.B. (brvnlou@rockefeller.edu) or E.D.S. (siggiae@rockefeller.edu).

Abstract

Long range signalling by morphogens and their inhibitors define embryonic patterning yet quantitative data and models are rare, especially in humans. Here we use a human embryonic stem cell micropattern system to model formation of the primitive streak (PS) by WNT. In the pluripotent state E-CADHERIN (E-CAD) transduces boundary forces to focus WNT signalling to colony border. Following application of WNT ligand, E-CAD mediates a front or wave of epithelial-to-mesenchymal (EMT) conversion analogous to PS extension in an embryo. By knocking out the secreted WNT inhibitors active in our system, we show that DKK1 alone controls the extent and duration of patterning. The NODAL inhibitor CERBERUS1 acts downstream of WNT to refine the endoderm versus mesoderm fate choice. Our EMT wave is a generic property of a bistable system with diffusion and a single quantitative model describes both the wave and our knockout data.

Development • Accepted manuscript

© 2019. Published by The Company of Biologists Ltd.

Introduction

The WNT, BMP, and ACTIVIN/NODAL signalling pathways play a dominant and largely conserved role in vertebrate development. Despite extensive knowledge of the intracellular aspects of these pathways, however, many quantitative aspects of how they create and mediate large-scale patterns remain unknown, especially in the context of human development. A prime example of this is the patterning of the human epiblast, where in a period of approximately two days, and on a millimeter length scale, these three pathways overlap and create the necessary instructions to form and pattern the primitive streak (PS), from which the embryonic germ layers and future anterior-posterior axis of the human embryo emerges. While mouse studies have shed some light on the involvement of these pathways in the patterning processes, differences in architecture, timing, and juxtaposition of extraembryonic and embryonic tissues makes the direct comparison difficult[1,2]. Because of these differences and because the interactions of the aforementioned pathways are complex, with multiple morphogens and secreted inhibitors from overlapping regions acting at the same time, there is a need for an assay that allows for their control in a model human epiblast that also permits a dynamic readout on the scale of single cells.

We have previously shown that human embryonic stem cells (hESCs) confined to micropatterned colonies of 1 millimeter diameter can be used as *in vitro* assay to model the human epiblast[3,4]. These micropatterns self-organize in response to WNT, BMP, and ACTIVIN/NODAL signalling and recapitulate the patterning of germ layers observed during mammalian gastrulation. For example, stimulation with BMP4 for 48 hours results in concentric rings corresponding to ectoderm, mesoderm, endoderm, and extraembryonic tissue arranged from the center to edge. As current guidelines prohibit the studies of human embryos after 14 days (the 14 day guideline) these models currently remain the best alternative to direct *in vivo* studies. More importantly, these models allow single-cell quantification and control over geometry, density, signalling strength, and genetics.

In subsequent work we exploited this assay to uncover how the BMP pathway contributes to this patterning[5]. Briefly, cells in the colonies are apically-basally polarized and BMP4 receptors are located on the baso-lateral sides of the cells, restricting access to the apically supplied medium except near the edges. This receptor mediated prepattern, already present in the pluripotent state, is reinforced by the secreted BMP inhibitor NOGGIN, which in humans is directly induced by BMP4. Due to diffusion and boundary conditions, NOGGIN is highest in the center and lowest at the colony edges, resulting in an effective gradient of BMP response across the colony.

Development • Accepted manuscript

We have also shown that BMP4 induces WNT ligand and that this WNT is necessary for the mesoderm and endoderm part of the pattern[6]. Additionally, we have shown that WNT signaling is sufficient to induce the self-organization of a human PS at the edge of colonies, and that co-presentation of WNT3A and ACTIVIN leads to the induction of functional human organizer cells that can induce an ectopic secondary axis in chick embryos. Since here again there is a self-organized patterned response to a uniformly presented ligand, our system offers an ideal environment to explore how WNT signalling leads to spatial organization, and specifically how the human PS forms and is spatially confined.

Here we address the molecular mechanisms underlying WNT-mediated self-organization of human PS. We show that two primary factors control patterning: E-CADHERIN (E-CAD) and DKK1. First, E-CAD establishes a pre-pattern by limiting the initial WNT response to the boundary. Secondly, and in parallel to the NOGGIN dynamics in the BMP case, the secreted inhibitor DKK1 is upregulated by a combination of WNT and NODAL signalling and is required to ultimately confine the PS to the colony boundary. Multiple single and double combinations of homozygous CRISPR/Cas9 knockouts of secreted inhibitors of the WNT and NODAL pathways confirmed that only DKK1 plays a major role in the spatial restriction of the PS. We found that CERBERUS1 (CER1) is also highly upregulated by a combination of WNT and NODAL signalling, but that in our cells it functions as a NODAL inhibitor rather than dual WNT/NODAL inhibitor. CER1 thus does not influence the size of the PS, but instead serves to bias the mesoderm versus endoderm fate decision in this region. We found also that in our DKK1$^{-/-}$ cells E-CAD not only establishes a pre-pattern, but, via its mutual antagonism with WNT, generates a cooperative EMT wave that travels from the micropattern periphery to the center.

Results

WNT response is edge and density dependent and apically-basally symmetric

We previously showed that uniform application of WNT3A ligand to hESC micropatterns is sufficient to self-organize a PS-like structure, with mesoderm and endoderm emerging from an EMT on the colony periphery after 48 hours and with ACTIVIN/NODAL level biasing the choice of endoderm versus mesoderm[6] (Figure 1A). During this time the transcription factor SOX17 demarcates the endoderm and the transcription factor BRACHURY (BRA) demarcates mesoderm. Changes in the EMT markers SNAIL, E-CAD, and N-CAD can also be used to identify the PS, but since these markers are more transient and harder to measure than BRA or SOX17[6], we will use the union of SOX17 and BRA to define the spatial extent of the induced PS. We also showed previously that despite the uniform application of WNT, the interior of the colony remains pluripotent, expressing both NANOG and SOX2[6]. This pattern, with pluripotent cells on the interior and mesoderm and endoderm cells on the periphery, represents the terminal spatial pattern we seek to understand.

Development • Accepted manuscript

In order to decipher the molecular mechanism underlying this spatial pattern, we first attempted to use the detection of nuclear β-CATENIN (β-CAT) as an early readout for canonical WNT signalling[7–9]. However, commercially available antibodies did not have adequate resolution on our dense epithelia (Figure S1A), so instead we used LEF1, a co-factor of β-CAT that is a direct target of WNT signalling with the same response profile as AXIN2 (Figure S1B) and is localized to the nucleus[10,11]. We found that the LEF1 response profile depended on colony density, with nuclear expression throughout the colonies at low density and restriction to the periphery at high density (Figure 1B). Co-presentation of the SMAD2 pathway inhibitor SB-431542, together with WNT3A did not change the outcome, demonstrating that the density dependence of the LEF1 pattern is specifically due to WNT, and not caused by secondary ACTIVIN/NODAL signaling.

Similar to previous work studying the effect of colony density on BMP signalling[5], low density represents a pre-epithelial state before tight junctions have completely established themselves, while high density represents an epithelial state with complete tight junctions (Figure 1C) where the SMAD1 response due to BMP stimulation would also be edge restricted (Figure S2C). Because density is an important variable, for all experiments in this study we consistently use two defined values of seeding density “low” or “high” (Figure S2B).

As one of the factors involved in BMP4- induced self-organization was due to polarized signal reception, we first examined the localization of the WNT receptors[12] FRIZZLED and LRP5/6 in our micropatterns. We find that while some WNT-receptors were detected on the apical side, they were predominantly and homogenously located basolaterally underneath the tight junctions (Figure 1D). We also find little distinction between edge and center. To functionally test for signal reception, we cultured cells on transwell-filter culture dishes, where cells can be selectively stimulated from the apical or basal side. Cells were cultured at the same density as the high density micropatterns and stimulated them with WNT3A for 12 hours. While a stronger response was detected with basal rather than apical stimulation, the mean basal response on filters, however fell below the edge response on colonies (Figure 1E and F), suggesting that additional factors were involved in setting up the WNT response on the colony boundary.

E-CAD knockdown sensitizes cells to WNT

Given the fact that E-CAD is classically considered to antagonize WNT signalling via its binding and sequestration of β-CAT[13–16], and the fact that cells on the periphery of our micropatterns have fewer neighbouring cells and so presumably fewer E-CAD junctions, we hypothesized that E-CAD may contribute to the early WNT pattern. To test this hypothesis we made clonal CRISPR/Cas9 E-CAD knockout cell lines. We used a guide RNA targeting a region present in all isoforms of the protein and confirmed the result with western blot and immunofluorescence using two separate antibodies (Figure

Development • Accepted manuscript

S2F-H). We found that E-CAD$^{-/-}$ hESCs could be passaged and seeded as per normal hESC culture, grew at the same rate as wild type cells, maintained pluripotency markers as single cells, unpatterned colonies, and micropatterned colonies, and still apical-basally polarized at high density to form intact epithelia (Figure S2A-D). E-CAD$^{-/-}$ WNT receptor localization was indistinguishable from wild type (Figure S2E), and the response to BMP4 continued to be edge only. Interestingly, N-CADHERIN (N-CAD) protein was up regulated in the knockout (Figure S3), and in other contexts can substitute for the loss of E-CAD[17].

The most striking phenotype of the E-CAD$^{-/-}$ cells, however, was that the early WNT pattern was abolished in E-CAD$^{-/-}$ micropatterns (Figure 2). Cells at the center of high density colonies now showed nuclear localization of LEF1. Quantifying our results over multiple micropatterns, we observed that the WNT response is modestly biased to the edge, and generally comparable to the level in low density colonies (Figure 2D). Our transwell filter assay still showed an apical-basal asymmetry, but now the basal response was elevated to match the edge response of the parental cells (Figure 1E and F). These results demonstrate that the early WNT pattern is primarily due to E-CAD activity, and a minor influence exerted by WNT receptor accessibility.

If all cells express E-CAD why are there spatial differences in the WNT response? We hypothesized that spatial differences in E-CAD localization or in the state of E-CAD junctions and their binding partners could account for spatial WNT signalling differences. E-CAD and β-CAT stains support this hypothesis as they show that in high density wild type micropatterns E-CAD is reduced in cells on the periphery and there is observable cytoplasmic β-CAT here as well (Figure 2A and B). Actin stress fibers have also been observed on hESC micropattern boundaries[18,19] and have been implicated in E-CAD dysregulation[20]. Phalloiden staining in our wild type micropatterns revealed that there were indeed actin stress fibers and they were restricted to the region that is WNT responsive. Furthermore, these stress fibers are absent from low density or E-CAD$^{-/-}$ micropatterns (Figure 2A), which suggests a connection between mechanics and WNT signalling.

Disruption of E-CAD/β-CAT binding or actin cytoskeleton also sensitizes cells to WNT

To further test whether the classical connection between E-CAD, β-CAT, and the actin cytoskeleton was responsible for our early WNT pattern we performed two additional experiments. In the first we inserted into our E-CAD$^{-/-}$ cells either constitutively expressed full length E-CAD or constitutively expressed E-CAD that lacked the β-CAT binding domain[21] into the AAVS1 locus using TALENS. Clonal lines were cultured in micropatterns and stimulated for 12 hours to examine the WNT response. We found that the constitutively expressed full length E-CAD rescued the edge restricted phenotype but that the E-CAD without the β-CAT binding domain did not (Figure 3A-B). This shows that E-CAD binding to β-CAT is essential for the early WNT pattern.

Development • Accepted manuscript

In the second experiment we disrupted the actin cytoskeleton across the entire micropattern with the small molecule inhibitors blebbistatin or cytochalasin B while stimulating with WNT3A. Blebbistatin has been shown to dislodge E-CAD from the membrane into the cytoplasm in hESCs in pluripotency[22], and cytochalasin B has an even more direct action on dissociating the actin cytoskeleton. We found that both reduced the edge restriction, with blebbistatin broadening the size of the LEF1 band and cytochalasin B permitting a WNT response even in the center of the colony (Figure 3C). Taken together, our results demonstrate that colony geometry acts via the cytoskeleton and E-CAD to bias WNT signalling to the colony boundary.

Self-organization of the PS to the edge occurs in E-CAD$^{-/-}$ cells

Having understood the reasons for the edge asymmetry in the initial response to WNT, we were surprised to see that the location of the PS was virtually the same in wild type and E-CAD$^{-/-}$ colonies at 48 hours (Figure 4A). Examination of LEF1, SOX2 and BRA expression at intermediate times showed that a homogenous early expression of these markers gradually becomes restricted to the edge (Figure 4B). Since cells in these colonies continue to grow and divide throughout this time course we checked whether increasing density could be responsible for this effect. However, E-CAD$^{-/-}$ colonies at a higher starting density (matching that of the Figure 4A colonies after 36 hours stimulation) also showed a WNT response in the center (Figure S3C). Thus we rule out cell proliferation and increasing density as a major contributing factor for the progressive edge restriction of the WNT response, and instead note that these dynamics are suggestive of a WNT induced secreted inhibitor of WNT that is highest in the center and progressively restricts WNT activity to the boundary.

We had previously shown that BMP4 directly induced the expression of its own inhibitor NOGGIN, which in turn was necessary and sufficient to restrict BMP signalling to the colony edge after 48 hours of stimulation[5]. To address if a similar mechanism of WNT3A inducing its own inhibitor was involved in this case as well, we activated the pathway with CHIR-99021, a small molecule compound that acts cell autonomously and will skip receptors and secreted inhibitors. After 48 hours stimulation the compound edge restriction was abolished (Figure 4C). This result strongly suggests the involvement of secreted inhibitors in WNT-mediated self-organization and PS formation.

WNT induces WNT and NODAL inhibitors

To further test this hypothesis, and identify the relevant inhibitors, we focused on WNT inhibitors whose loss-of-function leads to early gastrulation defects phenotypes in the mouse. These include SFRP1, SFRP2, DKK1, and DKK3[23]. Additionally, as WNT activates NODAL[6], and these the two ligands have been shown to act synergistically to induce mesendodermal genes[24], we also included LEFTY1,

Development • Accepted manuscript

LEFTY2, and CER1 on our list. qPCR was used to assess the induction of these inhibitors when cells were treated with WNT3A alone, or WNT3A+SB to distinguish direct versus indirect induction. After 12 and 24 hours of stimulation, expression of SFRP1, SFRP2, and DKK3 remain relatively unchanged regardless of WNT3A or WNT3A+SB treatment (Figure 4D). DKK1 expression, however, was highly up-regulated in response to WNT3A. Similar to what has been previously reported[24], this appears to depend on synergy between the WNT and NODAL pathways, since DKK1 induction is lower in WNT3A+SB conditions. A stronger dependence on SMAD2 signaling was observed for the WNT3A induction of CER1 expression. Finally, the expression of LEFTY1 and LEFTY2 depend even more on NODAL signalling since they are also down-regulated in WNT3A+SB and cannot be activated with WNT3A alone. Thus DKK1 and CER1 emerged as the leading candidates involved in WNT self-organization.

DKK1 controls the size of the PS

To test whether DKK1 and CER1 are required for the late time WNT pattern, we used CRISPR/Cas9 to generate DKK1 and CER1 knockouts. Each clonal line was stimulated with WNT3A and compared to wild type. After 12 hours of stimulation, DKK1$^{-/-}$ colonies showed no difference with the control (Figure 5A). After 48 hours of treatment, however, the size of the PS was dramatically increased when compared to the wild type and E-CAD$^{-/-}$ lines, with only a small center of SOX2+ undifferentiated cells remaining (Figure 5B and C). This result, which was confirmed in two additional clonal DKK1$^{-/-}$ lines (Figure S4A), demonstrates that DKK1 activity is required for WNT-mediated patterning, and is consistent with a reaction-diffusion model.

To further test this interpretation and see whether human DKK1 protein can protect cells from WNT ligand at a distance in a non-cell autonomous manner, we created a clonal RUES2 cell line that expresses human DKK1 tagged with V5 epitope under the control of a doxycycline promoter (Figure S4G). When these RUES2-DOX:DKK1-V5 cells are seeded sparsely into E-CAD$^{-/-}$ micropatterns and made to express DKK1, we can see that they can block BRA expression in cells up to ~5 cell lengths away from them, thus demonstrating that human DKK1 can act as a long-range diffusible WNT inhibitor (Figure S4H-I).

To test for epistasis between WNT inhibition at early times mediated by E-CAD, and at late times by DKK1, we generated a double E-CAD$^{-/-}$DKK1$^{-/-}$ knockout line. In response to WNT3A stimulation for 48 hours, all cells in the micropatterned colonies differentiated, with no SOX2+ cells left in the center (Figure 5B and C). This suggests that DKK1 and E-CAD are the two major players among the collection of WNT inhibitors that block differentiation in our micropatterns.

Development • Accepted manuscript

Comparison of the expanded PS in the single and double knockouts with wild type and classification of cell types (see Methods and Figure S5A-B) also established that both the total number and the ratio of BRA to SOX17 cells changed (Figure 5D). Whereas the proportion BRA+/SOX17- cells in RUES2 wild type line was ~10%, in DKK1$^{-/-}$ cells it doubled to 20%, and in E-CAD$^{-/-}$DKK1$^{-/-}$ it tripled to ~30%. The fraction of cells that express both BRA and SOX17 also greatly increases in the mutant lines. This suggests that in addition to determining the size of the PS, DKK1 may also be involved in the segregation of mesodermal and endodermal fates.

CER1 biases mesoderm versus endoderm fate decision

When stimulated with WNT3A, CER1$^{-/-}$ cells did not show any change in the size of the PS domain in comparison to wild type (Figure 5E). There was, however, a significant shift in the proportion of mesodermal versus endodermal fates. Unlike the DKK1$^{-/-}$ or E-CAD$^{-/-}$DKK1$^{-/-}$ cells, this time the shift was towards greater endoderm, with almost all differentiated cells expressing SOX17 and none expressing BRA (Figure 5D). This represents a similar phenotype to the WNT3A+ACTIVIN treatment (Figure 1A), and prompted us to investigate the status of NODAL/ACTIVIN signaling. We find that SMAD2 signalling is significantly enhanced in the CER1$^{-/-}$ knockout line (Figure 5F and G), penetrating farther into the colony from the edge and with a higher nuclear to cytoplasmic ratio. It is known in mouse that CER1 inhibits BMP and NODAL signalling but not WNT signalling[25] (at odds with other vertebrates systems where its tri-functionality motivates its name[23]). For human however it is only known that CER1 inhibits NODAL and a subset of BMP ligands, with a verdict on WNT inhibition still awaiting[26,27]. Since the size of the PS remains unchanged while SMAD2 signaling increases along with the proportion of endodermal cells in the CER1$^{-/-}$ colonies, our results suggest that in hESCs CER1 acts primarily as a NODAL inhibitor rather than a WNT inhibitor.

As it was previously shown in the mouse that the most dramatic CER1 phenotype is when it is doubly knocked out with LEFTY1[28], we also generated CER1$^{-/-}$LEFTY1$^{-/-}$ and LEFTY1$^{-/-}$ clonal cell lines. We detected no difference in the WNT response phenotype between wild type and LEFTY1$^{-/-}$ cells, and no difference between CER1$^{-/-}$ and CER1$^{-/-}$LEFTY1$^{-/-}$ cells (Figure S4B and C). In order to check for all other players identified in our RNA-seq and qPCR results, we generated DKK3$^{-/-}$ and SFRP1$^{-/-}$SFRP2$^{-/-}$ clonal cell lines. None of these lines displayed any phenotypic difference when compared to wild type (Figure S4D-F). We conclude that DKK1 and CER1 are the major secreted inhibitors that control WNT patterning in our model system.

Development • Accepted manuscript

An edge to center WNT/EMT wave

The size of the PS region in the DKK1$^{-/-}$ cell line at 48 hours is intermediate between the smaller wild type PS region and the fully converted PS region of the double E-CAD$^{-/-}$DKK1$^{-/-}$ cell line. Given that in both RUES2 and DKK1$^{-/-}$ colonies WNT signalling begins at the edge (Figure 5A), an important and relevant question is whether the 48 hour result is at steady-state, or if given more time the PS would eventually expand inward and consume the entire colony. To address this question we fixed and stained wild type and DKK1$^{-/-}$ micropatterns at 12, 24, 48, and 72 hours. We find that while differentiation starts similarly for both, the wild type micropatterns seems to reach a steady state by 24-48 hours while differentiation and EMT in the DKK1$^{-/-}$ colonies continues to proceeds inwards, eventually almost consuming the entire micropattern by 72 hours (Figure 6A). This is consistent with a wave of WNT differentiation proceeding from the outer edge to the center.

To confirm the existence of this wave and study it further, we knocked out DKK1 in a previously described RUES2-GLR (Germ Layer Reporter) cell line where ectoderm (SOX2), mesoderm (BRA), and endoderm (SOX17) germ layers are tagged with 3 separate fluorescent markers[6]. This enabled us to evaluate the change in differentiation and fate acquisition in the same micropattern across different times. Stimulation of the control RUES2-GLR with WNT3A leads to a downregulation of SOX2 and an upregulation of SOX17 that begins at the edge but stops a few cell layers inward, maintaining the PS at the periphery. RUES2-GLR colonies in which the DKK1$^{-/-}$ mutation is introduced, however, display a wave of progressive downregulation of SOX2 and upregulation of SOX17, which, as in the stained time-course, begins at the outer edge and does not stop (Figure 6B and C).

What is the mechanism for such a wave? Given that E-CAD expression recedes as the differentiation front advances (Figure 6A) we posit that the wave results from a positive EMT feedback loop. WNT3A is known to induce EMT and to down-regulate E-CAD through the transcription factor SNAIL[29,30]. As illustrated in Figure 6D, WNT3A first down-regulates E-CAD in WNT susceptible edge cells and causes them to go through EMT. In so doing, these cells destabilize their E-CAD junctions with their neighbours. This leads to a domino like propagation of EMT from cell to cell via shared cell contacts. If the differentiated cells were induced to secrete a diffusing and thus long-ranged WNT inhibitor, i.e. DKK1, then it will accumulate in the center more than the edges and the wave would be expected to halt[5]. This is how the wild type cells achieve the observed steady state we, and why the DKK1$^{-/-}$and GLR:DKK1$^{-/-}$ cells fail to do so.

In addition to these dynamics, previous results have shown that WNT ligand also upregulates WNT production in hESCs[6]. To test if this endogenous WNT signalling contributed to the dynamics we compared wild type and DKK1$^{-/-}$ micropatterns with and without IWP2, a small molecule that blocks all WNT ligand secretion. We find no significant differences (Figure S6A), most likely due to the fact that we were already stimulating our micropatterns with a high dose if WNT in the media and thus are in a saturated regime where endogenous WNT does not make any significant contribution to the dynamics.

Development • Accepted manuscript

We also tested the involvement of ACTIVIN/NODAL signalling (which has a baseline activity in our media) in this wave by comparing DKK1$^{-/-}$ micropatterns stimulated either with WNT3A or WNT3A+SB. Consistent with other studies of EMT[31], our wave stops when we block ACTIVIN/NODAL signalling with SB (Figure S6B).

A quantitative dynamic model

The spatial pattern of WNT signalling in our colonies is defined by inhibition from E-CAD at the earliest times and DKK1 at later times. These inhibitors operate very differently in space: E-CAD bridges adjacent cells, while DKK1 diffuses across the colony and also leaks out at the edges[5]. Downstream of WNT, NODAL and CER1 are produced and together with WNT generate mesoderm and endoderm fates. To fully unravel the complexity involved in this process we formulated a quantitative dynamic model.

A good model will use a portion of the data to fit parameters and then make testable informative predictions about the remainder of the data, and do this with as few variables as possible. With these criteria in mind we define a 2D partial differential equation (PDE) model where the intracellular WNT signal, *W(r,t)*, is normalized to [0,1] and where a simple Michaelis-Menten system of equations links it to DKK1 and E-CAD. One advantage of our formulation is that it is separable, so we can fit the DKK1 specific parameters to the E-CAD$^{-/-}$ data and vice versa (Figure 7A). Since we cannot directly measure WNT levels we use the immunofluorescence data for LEF1 at 12 hours and the percentage loss of SOX2 at 48 hours as surrogates, after normalizing to [0,1]. For the full list of equations, descriptions of the variables, and initial and boundary conditions, the reader is directed to the Supplemental Methods.

Figure 7C shows the quality of the fits to the immunofluorescence data at 12 and 48 hours in the two knockout lines that we consider quite acceptable (Suppl. Figures M2 and 4). Our model with no additional adjustments is then able to predict and reproduce the 72 hour data in Figure 7C as well as the EMT wave (in the DKK1$^{-/-}$ background with endogenous E-CAD), which is most visible in the GLR:DKK1$^{-/-}$ cell line (Figure 7D). This live data is somewhat variable due to density variation and phototoxicity (see Supplemental Methods) but the prediction of the shape of the wave front and where it should be at a specific time closely follows the observations. The collapse of the wave after it reaches a radius of about 200 µm is also predicted and the model agrees with both the live data and the immunofluorescence data in Figure 6A.

The model makes explicit and mathematically precise that the reciprocal inhibition between WNT and E-CAD (Figure 7A) can give rise to bistability, and how, in the absence of the long-range secreted inhibitor DKK1, the bistability resolves by an inward propagating wave that eliminates the epithelial state in favour of the PS mesenchyme. The model situates the WNT system within a general class of problems where waves result from bistability. The interest for development, elaborated in discussion,

Development • Accepted manuscript

is that waves propagate information faster than diffusion, and the proposed mechanism is generic and largely parameter independent.

Having captured the WNT response dynamics for the different cell lines, we can further model whether the differentiated cells become endoderm or mesoderm. To do so we assume that NODAL favours endoderm over mesoderm[6], and we describe this as a branching probability from an intermediate mesendoderm state (Figure 7B), since we lack more quantitative data about the genetic network for mesendoderm specification. As a surrogate for NODAL signalling we used measured SMAD2 profiles at 24 hours for each cell line (Figure 5G and Figure M5 in Supplemental Methods). Figure 7E shows the comparison of model and data. The conversion of mesoderm to endoderm due to up regulation of NODAL is clearly visible in the comparison of CER1$^{-/-}$ with wild type or E-CAD$^{-/-}$.

Discussion

Untangling the dynamics of early cell fate specification, and pattern formation during gastrulation remains a formidable challenge, especially during early human development. Using highly quantitative and standardized human gastruloids to model human gastrulation, we had previously shown the cascade of signaling begins with BMP4, which is sufficient to induce gastrulation and pattern all germ layers within 48 hours. We subsequently established that the mechanism underlying this BMP self-organization of gastrulation is based on two components: TGFβ receptors are only exposed to apical signals in a pre-pattern around the edge of the colony, and a Turing-like reaction-diffusion mechanism mediated by NOGGIN, which specifically in humans is induced directly by BMP4. We subsequently showed that the WNT pathway, operating downstream of BMP4, is necessary and sufficient for the mesoderm and endoderm layers and can self-organize its own pattern. In this work we have unraveled the molecular mechanism underlying this WNT-mediated self-organization.

This mechanism includes several elements. The first element is the “pre-pattern” of WNT sensitivity. Unlike the situation with BMP4 this pre-pattern is not imposed by polarity of receptor localization, but rather by β-CAT mechano-sensation via E-CAD, and the cytoskeleton, which is governed by tissue geometry. Given the importance of this pre-pattern for WNT patterning in a model human epiblast, how applicable might such pre-patterns be to gastrulation more generally? Gastrulation takes many forms across all animals, but a common theme is the correlation of WNT signalling with invagination[32] (such as for example through the PS in amniotes or through a blastopore in lower orders). Invagination necessarily involves a breaking of geometric symmetry and a concentration of mechanical forces in an area of high curvature, and it is tempting to think that β-CAT mechanosensation is also involved here in either pre-patterning or reinforcing a WNT signal. Other notable examples of β-CAT mechanosensation as a critical element for WNT patterning include are found *Drosophila* gastrulation[33], *Xenopus* embryonic explants[33], and avian follicles[34].

Development • Accepted manuscript

The second element in the WNT patterning process is the Turing-like activator-inhibitor pair of WNT and DKK1. In a manner similar to BMP4 which in species-specific manner induces NOGGIN, the WNT ligand also directly induces the expression of its own inhibitor: DKK1. In the mouse the anterior visceral endoderm (AVE) on the opposite side of the embryo from the PS is traditionally thought of as the major source of DKK1, with this inhibitor being produced in a WNT independent manner[1,35]. The expression of DKK1 by the AVE makes disentangling any intrinsic contribution of the epiblast to the position and control of the PS in the embryo difficult. Given that our synthetic epiblast achieves a stable pattern via the induction of DKK1 by WNT without external sources, however, we might expect to see DKK1 produced by cells in the PS. This is exactly what recent single cell and FACS sorted RNA-seq data shows[36,37]. Similarly, results from studies in rabbit gastrulation show that DKK1 is also expressed in cells in the PS, especially in epiblast cells undergoing EMT[38]. While expression of activator and inhibitor on opposite sides of an embryo (such as in PS and AVE) seems logical and necessary, the Turing mechanism requires production of the inhibitor where the activator is highest, since the inhibitor must also spread rapidly to confine the activator.

We discovered that the same is true for the CER1, the third major element in the WNT patterning process. Despite also being thought of as an AVE product, single cell RNA-seq studies show that CER1 is also expressed in the mouse and rabbit PS[36,38]. In our human model we find that CER1 acts as a NODAL inhibitor and controls the balance between mesodermal and endodermal fates emerging from the back of the EMT wave. Thus E-CAD, DKK1, and CER1 are the primary determinants of WNT-induced PS patterning in artificial human epiblasts.

Our knockouts of CER1 and DKK1 in hESCs also reveal possible species specific differences between human, mouse, chick, and rabbit. For example, a difference between human and other studied species is that the knockout of CER1, or even the double knockout of CER1 and LEFTY1, does not lead to an expansion of the PS in our model system. This is surprising since in mouse it leads to multiple streaks[28] and in the chick NODAL repression by Cerberus is thought to be the dominant repressor of ectopic streaks[39]. Another difference is that the mouse Dkk1 knockout does not broaden the PS as defined by Bra expression, though it does broaden the expression of a synthetic Wnt reporter[40]. This could suggest that PS formation in human is dominated more by WNT signals whereas in mouse the PS and Bra require other signals (such as NODAL) as well. Indeed, recent experiments with mouse epiblast-like cells (EpiLCs) on micropatterns[41] suggest that there is a stronger dependence on NODAL signalling to achieve a PS-like region and Bra positive cells than in hESCs. We hope that future comparative experiments will shed light on these apparent species specific differences, and will also test for possible confounding *in vitro* versus *in vivo* differences as well.

Our results for the DKK1 and CER1 knockouts have implications not just for the spatial control of the streak, but also for mesoderm versus endoderm cell fate decisions within the streak. We found a higher ratio of mesoderm to endoderm in DKK1$^{-/-}$ cells, which is consistent with the reduction in the

Development • Accepted manuscript

mouse of anterior endoderm in favour of mesoderm following the analogous knockout[40]. Conversely, removal of CER1 favors endoderm over mesoderm in our system, with up regulation of nuclear SMAD2 compared with wild type. Although less well understood than the appearance of multiple streaks, the elimination of CER1 and LEFTY in the mouse embryo also results in a marked conversion of BRA cells to more NODAL regulated fates, such as anterior endoderm and axial mesoderm[28]. Based on these observations, as well as the result that WNT induces both DKK1 and NODAL in hESCs, we speculate that mammalian anterior endoderm is specified by a transient WNT3 pulse terminated by self-induced DKK1 and followed by up regulation of NODAL signalling. In fact, a transient application of WNT followed by its removal and the addition of ACTIVIN is precisely the most efficient and commonly used endoderm differentiation protocol used for hESCs[4,42–44].

One of the more intriguing results to emerge from our investigation was the presence of a propagating EMT wave or front from the edge of our micropatterns towards the center. This wave is generated by downregulation of E-CAD by EMT and the negative regulation of WNT signalling by E-CAD, but also requires ACTIVIN/NODAL activity since SB treatment blocks the wave. As DKK1 acts as a negative feedback to halt the wave, the wave is much longer and more apparent in the DKK1$^{-/-}$ micropatterns than wild type micropatterns. This is not to say, however, that wild type cells could not undergo such a wave *in vivo*. For example, removal via of the DKK1 expressing cells from the wave front, as happens in migration of the mesenchmyl cells out of the PS *in vivo,* would allow the wave to continue progressing. This cannot take place in our system since cells are confined to the surface of the micropattern. We note that although it is harder to cleanly isolate, in mouse and chick embryos there is evidence for cooperative EMT in maintaining and extending the PS[45,46].

Traveling waves of activity have been seen in several other developmental contexts, but it is important to distinguish propagation of a front separating two states with phase waves such as in somitogenesis that spatially modulate the phase of an underlying autonomous cellular oscillator[47]. Calcium waves following fertilization or in large embryos that are presumably to synchronize tissues[48,49]. A wave of mitotic activity in frog extracts has also recently been observed and linked to bistability in the CDK system[50]. Why might a wave be useful for patterning? A wave is rationalized as way to spread information more rapidly than diffusion in a large system, and the hundred micron scale disk-shaped epiblast in rabbit and humans may require such a solution. Patterning via a wave may be a widespread mechanism for tissue patterning since it only requires a bistable system and some means for the favoured state to spread between cells.

Our hESC micropatterned PS model provides a platform where complex and developmentally relevant patterning dynamics can be followed, quantified, and ultimately deconstructed. It thus provides a means to understand how embryonic development can be both so robust and yet flexible, and to ultimately apply this understanding to engineer systems to further regenerative medicine.

Development • Accepted manuscript

METHODS

Cell Culture: All experiments used either the RUES2 hESC cell line, CRISPR/Cas9 edited cell lines based on this line, or CRISPR/Cas9 edited versions of the previously described RUES-GLR cell line[6]. hESCs were maintained in HUESM medium conditioned by mouse embryonic fibroblasts (MEF-CM) with additional 20 ng/mL bFGF. Mycoplasma testing was carried out before beginning experiments and again at regular 2-month intervals. Cells were grown on GelTrex (Invitrogen) coated tissue culture dishes (BD Biosciences, 1:40 dilution) for maintenance and expansion. Dishes were coated overnight at 4C and then incubated at 37C for at least 20 minutes before the cells were seeded onto the surface. Passaging was performed using Gentle Cell Dissociation Reagent (Stem Cell Technologies 07174).

Micropatterned Cell Culture: Micropatterns were created using glass coverslips from CYTOO. The coverslips were first coated with 10 ug/ml laminin 521 (Biolamina) then diluted in PBS with calcium and magnesium (PBS++) for 3 h at 37°C. hESCs were dissociated with StemPro Accutase (Life Technologies) for 7 minutes and then washed once with growth media, washed again with PBS, and then re-suspended in growth media with 10µM ROCK-inhibitor Y-27632 (Abcam) in 35mm tissue culture plastic dishes. For each coverslip $1x10^6$ cells in 2mL of media were used. After 1 h ROCK-inhibitor was removed and was replaced with standard growth media supplemented with Pen-Strep (Life Technologies). Cells were stimulated with the following ligands or small molecules 12 h after seeding: 100ng/mL WNT3A, 100ng/mL Activin-A, 10µM SB, 6µM CHIR.

Immunocytochemistry: Cells were fixed in 4% paraformaldehyde for 20 minutes at room temperature, washed twice and stored in PBS. Permeabilization (30 minutes at room temperature), primary antibody incubation (overnight at 4C), and secondary antibody incubation (30 minutes at room temperature) were carried out with blocking buffer (3% donkey serum and 0.1% Triton X-100 in PB). After the primary incubation cells were washed 3 times with PBST (PBS + 0.1% Tween-20) for 30 minutes each. After secondary incubation cells were washed twice more with PBS, and then mounted on glass slides for imaging. All of the primary antibodies used are listed in Table S1.

Microscopy and Image Analysis: All images used were acquired with a Zeiss Axio Observer using ZEN software and a 20x/0.8 numerical aperture (NA) lens. All image analysis was conducted using custom software written in Matlab. Images were first background subtracted and normalized and then stitched on a colony by colony basis. Scenes for background subtraction and normalization were acquired in the spaces between colonies where no cells were present. For segmentation of individual cells, we first used Ilastik classification to separate foreground from background. The classifier was trained for each experiment on the DAPI images of 4 randomly chosen colonies stitched colonies from that experiment. Once foreground and background were obtained, the DAPI channel was then filtered with a median and h-max filter and subtracted against a gradient of the image in order to identify the nuclei centers. These centers were then used as seeds for a watershed, against which the background

Development • Accepted manuscript

mask was applied to obtain the final segmentation. Using this segmentation mask we then obtained average intensities for each cell of the nuclear markers in the other channels. For radial plots, the intensity of IF signal for each marker was normalized to the DAPI intensity, and these corrected single-cell expressions were then radially binned and averaged. The final radial profile represents the average of the indicated number of colonies. For clustering and classification, single-cell intensities were log transformed and then clusters were fit with a Gaussian mixture model (see Figure S5 for example).

qPCR and RNA-seq: RNA was collected in Trizol at indicated time points from either micropatterned colonies or from small un-patterned colonies. Total RNA was purified using the RNeasy mini kit (Qiagen). qPCR was performed as described previously[5], and primer sequences are listed in Table S2. RNA-seq is from a previously published data set[5], and all raw data are available from the GEO database, accession number GSE77057.

Transwell Experiments: We used Costar Transwell 24-well plates with 0.4µm pore-sized clear polycarbonate membrane inserts (Fisher Scientific 07-200-147). Membranes were coated with 10 µg/mL of laminin 521 (Biolamina) diluted in PBS++ for 3 hr, followed by washing 3 times with PBS++. Single cells were collected and seeded as per micropattern protocol. To image the membrane the transwell was removed from the multi-well plate after fixing and staining and placed on top of a coverslip.

Generation of E-CAD insertion and DKK1 inducible cell lines: Full length E-CAD and E-CAD lacking β-CAT binding domain were amplified via PCR from hE-cadherin-pcDNA3 and hE-cadherin/Δβ-catenin-pcDNA3 plasmids (Addgene plasmids #45769 and #45772) and inserted downstream of a pCAG promoter and puromycin resistance cassette flanked by 1kb homology arms for the AAVS1 safe harbour locus. This plasmid and TALENS targeting the AAVS1 site were then nucleofected into $1x10^6$ pluripotent E-CAD$^{-/-}$ cells using the B-016 setting on an Amaxa Nucleofector II (Lonza). Nucleofected cells were then plated as per maintenance conditions, but supplemented with 10uM ROCK-inhibitor. Selection for both puromycin commenced after 2 days, and ROCK-inhibitor was maintained until colonies reached adequate size (typically 8-16 cells per colony). To derive pure clones, individual colonies were picked in an IVF hood with a 20uL pipette tip and seeded into separate wells with growth media and ROCK-inhibitor. Once successfully established, each clone was assayed functionally for brightness and homogeneity of the overexpressed E-CAD. The RUES2-DOX:DKK1-V5 cell line was obtained in an identical fashion, except for the use of a TRE promotor instead of a pCAG promoter and an rTA-T2A-puromycin element instead of only puromycin. The V5 tag was attached to the C terminal end of DKK1, and DKK1 itself was obtained from a commercially available cDNA plasmid (Thermfisher Scientific # MHS6278-202801665).

Development • Accepted manuscript

Generation of knockout lines: The CRISPR/Cas9 system was used to generate all knockout lines. Three rules of reproducibility and quality control were applied: (i) at least two independent clones for each gene clonal lines were isolated and studied in parallel; (ii) lack of off-target effects was assessed by qPCR; and (ii) their ability to maintain the pluripotent state as assessed by expression of NANOG, OCT4, and SOX2. For the E-CAD, DKK1, and CER1 knockouts one clone of each was also assessed for chromosomal integrity by karyotyping. The sgRNA target for each gene is listed in Table S3. A list of all knockout lines is given in Table S4. The sgRNAs were cloned into a pX330 plasmid[51] that we modified to co-express a puromycin-2A-EGFP cassette, as this strategy gave us a higher percentage of successfully targeted clones. Transfection was carried out using the B-016 setting of a Nucleofector II instrument and using the Cell Line Nucelofector Kit L (Lonza). Transfected cells were immediately seeded in ROCK-inhibitor on GelTrex coated culture dishes, and puromyacin was added after 24 h for 24 h. Cells were then passaged as single cells using Accutase (Stem Cell Technologies) and sparsely seeded to facilitate picking individual clones. Clones were handpicked with a 20uL pipette tip and once expanded genomic DNA from each clone was extracted with the DNeasy Blood & Tissue kit (Qiagen). The locus for each targeted gene was then PCR-amplified using the primers listed in Table S4, and submitted for Sanger sequencing. The resulting chromatograms for each clone were decomposed using the TIDE webtool[52] http://tide.nki.nl. Only clones that showed a high probability for both alleles of the gene of interest having a missense mutation leading to a premature stop codon were kept. Examples of these mutations are shown in Figure S7A. As a check on the integrity of our most critical knockout cell lines, the E-CAD$^{-/-}$ clone 1, DKK1$^{-/-}$ clone 1, and CER1$^{-/-}$ clone 1 cell lines were additionally sent for karyotyping and were found to be karyotypically normal (Figure S7B). In the case of E-CAD we note that although there are 4 recorded isoforms (https://www.ncbi.nlm.nih.gov/gene/999) our sgRNA target is after the start codon of each and is present in all of these isoforms. As an additional check to ensure that our CRISPR/Cas9 mutation results in a complete knockdown instead of a hypomorph, we note that the E-CAD antibody we use to check for E-CAD presence using immunofluorescence (Figure 2A) was produced by immunization with a synthetic peptide corresponding to the sequence surrounding Pro780 of human E-cadherin[53]. This corresponds to Exon 15, which is near the C-terminus of the final protein and is shared between all the E-CAD isoforms present in our cells (Figure S2F). Immunofluorescence tests with an antibody from a different supplier that targets a different conserved region (Abcam #ab40772 produced by immunization with synthetic peptide within human E CAD) aa 600-700[54]) also gave the same result (Figure S2G).

Mathematical Modelling: See Supplemental Materials and Methods for details of the mathematical modelling.

Development • Accepted manuscript

Acknowledgements hE-cadherin-pcDNA3 and hE-cadherin/Δβ-catenin-pcDNA3 were gifts from Barry Gumbiner (Addgene plasmids #45769 and #45772). This work was supported by grants R01 HD080699 and R01 GM101653, and NSF grant PHY 1502151 to E.D.S. We thank members of our lab for constructive comments, especially Sam Khodursky and Fred Etoc, and we thank the staff of the Rockefeller Bio-Imaging Resource Center (BIRC) for their guidance in live imaging of the GLR reporter cell lines.

Author Contributions Conceptualization and writing, I.M., A.H.B., and E.D.S.; Experiments and construction of knockout lines performed by I.M.; All authors reviewed the manuscript.

Author Information Correspondence should go to E.D.S. (siggiae@rockefeller.edu) or A.H.B. (brvnlou@rockefeller.edu). Material requests should be addressed to A.H.B.

Competing Interests E.D.S. and A.H.B. are co-founders of Rumi Scientific.

Development • Accepted manuscript

REFERENCES

1. Arnold, S. J. & Robertson, E. J. Making a commitment: cell lineage allocation and axis patterning in the early mouse embryo. *Nat. Rev. Mol. Cell Biol.* **10,** 91–103 (2009).
2. Tam, P. P. L. & Loebel, D. A. F. Gene function in mouse embryogenesis: get set for gastrulation. *Nat. Rev. Genet.* **8,** 368–81 (2007).
3. Warmflash, A., Sorre, B., Etoc, F., Siggia, E. D. & Brivanlou, A. H. A method to recapitulate early embryonic spatial patterning in human embryonic stem cells. *Nat. Methods* **11,** 847–54 (2014).
4. Deglincerti, A. *et al.* Self-organization of human embryonic stem cells on micropatterns. *Nat. Protoc.* **11,** 2223–2232 (2016).
5. Etoc, F. *et al.* A Balance between Secreted Inhibitors and Edge Sensing Controls Gastruloid Self-Organization. *Dev. Cell* **39,** 302–315 (2016).
6. Martyn, I., Kanno, T. Y., Ruzo, A., Siggia, E. D. & Brivanlou, A. H. Self-organization of a human organizer by combined Wnt and Nodal signalling. *Nature* **558,** 132–135 (2018).
7. Riggleman, B., Schedl, P. & Wieschaus, E. Spatial expression of the Drosophila segment polarity gene armadillo is posttranscriptionally regulated by wingless. *Cell* **63,** 549–560 (1990).
8. Valenta, T., Hausmann, G. & Basler, K. The many faces and functions of β-catenin. *EMBO J.* **31,** 2714–2736 (2012).
9. Cadigan, K. M. & Peifer, M. Wnt signaling from development to disease: insights from model systems. *Cold Spring Harb. Perspect. Biol.* **1,** a002881 (2009).
10. Cadigan, K. M. & Waterman, M. L. TCF / LEFs and Wnt Signaling in the Nucleus. *Cold Spring Harb. Perspect. Biol.* **4,** 105–126 (2012).
11. Estarás, C., Benner, C. & Jones, K. A. SMADs and YAP Compete to Control Elongation of β-Catenin: LEF-1-Recruited RNAPII during hESC Differentiation. *Mol. Cell* **58,** 780–793 (2014).
12. MacDonald, B. T. & He, X. Frizzled and LRP5/6 Receptors for Wnt/β-Catenin Signaling. *Cold Spring Harb. Perspect. Biol.* **4,** 65–87 (2013).
13. Nelson, W. J. & Nusse, R. Convergence of Wnt, β-Catenin, and Cadherin Pathways. *Science* **303,** 1483–1487 (2004).
14. Heuberger, J. & Birchmeier, W. Interplay of cadherin-mediated cell adhesion and canonical Wnt signaling. *Cold Spring Harb. Perspect. Biol.* **2,** 1–25 (2010).
15. Fagotto, F., Funayama, N., Glück, U. & Gumbiner, B. M. Binding to Cadherins Antagonizes the Signaling Activity of β-Catenin during Axis Formation in Xenopus. *J. Cell Biol.* **132,** 1105–1114 (1996).
16. Ozawa, M., Baribault, H. & Kemler, R. The cytoplasmic domain of the cell adhesion molecule uvomorulin associates with three independent proteins structurally related in different species. *EMBO J.* **8,** 1711–7 (1989).
17. Libusova, L., Stemmler, M. P., Hierholzer, A., Schwarz, H. & Kemler, R. N-cadherin can structurally substitute for E-cadherin during intestinal development but leads to polyp formation. *Development* **137,** 2297–2305 (2010).
18. Rosowski, K. A., Mertz, A. F., Norcross, S., Dufresne, E. R. & Horsley, V. Edges of human embryonic stem cell colonies display distinct mechanical properties and differentiation potential. *Sci. Rep.* **5,** 14218 (2015).
19. Przybyla, L., Lakins, J. N. & Weaver, V. M. Tissue Mechanics Orchestrate Wnt-Dependent Human Embryonic Stem Cell Differentiation. *Cell Stem Cell* **19,** 462–475 (2016).

Development • Accepted manuscript

20. Kanellos, G. *et al.* ADF and Cofilin1 Control Actin Stress Fibers, Nuclear Integrity, and Cell Survival. *Cell Rep.* **13,** 1949–1964 (2015).
21. Gottardi, C. J., Wong, E. & Gumbiner, B. M. E-cadherin suppresses cellular transformation by inhibiting β-catenin signaling in an adhesion-independent manner. *J. Cell Biol.* **153,** 1049–1059 (2001).
22. Li, D. *et al.* Integrated biochemical and mechanical signals regulate multifaceted human embryonic stem cell functions. *J. Cell Biol.* **191,** 631–644 (2010).
23. Cruciat, C. M. & Niehrs, C. Secreted and transmembrane wnt inhibitors and activators. *Cold Spring Harb. Perspect. Biol.* **5,** 39–64 (2013).
24. Funa, N. S. *et al.* β-Catenin Regulates Primitive Streak Induction through Collaborative Interactions with SMAD2/SMAD3 and OCT4. *Cell Stem Cell* **16,** 639–652 (2015).
25. Belo, J. A. *et al.* Cerberus-like is a secreted BMP and nodal antagonist not essential for mouse development. *Genesis (New York, N.Y. : 2000)* **26,** 265–270 (2000).
26. Aykul, S., Ni, W., Mutatu, W. & Martinez-Hackert, E. Human cerberus prevents nodal-receptor binding, inhibits nodal signaling, and suppresses nodal-mediated phenotypes. *PLoS One* **10,** 1–23 (2015).
27. Aykul, S. & Martinez-Hackert, E. New Ligand Binding Function of Human Cerberus and Role of Proteolytic Processing in Regulating Ligand-Receptor Interactions and Antagonist Activity. *J. Mol. Biol.* **428,** 590–602 (2016).
28. Perea-Gomez, A. *et al.* Nodal antaginists in the anterior visceral endoderm prevent the formation of multiple primitive streaks. *Dev. Cell* **3,** 745–756 (2002).
29. Batlle, E. *et al.* The transcription factor Snail is a repressor of E-cadherin gene expression in epithelial tumour cells. *Nat. Cell Biol.* **2,** 84–89 (2000).
30. Cano, A. *et al.* The transcription factor Snail controls epithelial–mesenchymal transitions by repressing E-cadherin expression. *Nat. Cell Biol.* **2,** 76–83 (2000).
31. Derynck, R., Muthusamy, B. P., Saeteurn, K. Y. & Biology, T. Signaling pathway cooperation in TGF-β-induced epithelial- mesenchymal transition. *Curr. Opin. Cell Biol.* **31,** 56–66 (2014).
32. Arendt, D. in *Gastrulation: From Cells to Embryo* (ed. Stern, C.) 679–693 (Cold Spring Harbor Laboratory Press, 2004).
33. Farge, E. Mechanotransduction in Development. *Curr. Top. Dev. Biol.* **95,** 243–265 (2011).
34. Shyer, A. E., Rodrigues, A. R., Schroeder, G. G., Kassianidou, E. & Harland, R. M. Emergent cellular self-organization and mechanosensation initiate follicle pattern in the avian skin. *Science* **357,** 811–815 (2018).
35. Kimura-Yoshida, C. *et al.* Canonical Wnt signaling and its antagonist regulate anterior-posterior axis polarization by guiding cell migration in mouse visceral endoderm. *Dev. Cell* **9,** 639–50 (2005).
36. Peng, G. *et al.* Spatial Transcriptome for the Molecular Annotation of Lineage Fates and Cell Identity in Mid-gastrula Mouse Embryo. *Dev. Cell* **36,** 681–697 (2016).
37. Simunovic, M. *et al.* Molecular mechanism of symmetry breaking in a 3D model of a human epiblast. *bioRxiv* 330704 (2018). doi:10.1101/330704
38. Idkowiak, J., Weisheit, G., Plitzner, J. & Viebahn, C. Hypoblast controls mesoderm generation and axial patterning in the gastrulating rabbit embryo. *Dev. Genes Evol.* **214,** 591–605 (2004).
39. Bertocchini, F. & Stern, C. D. The hypoblast of the chick embryo positions the primitive streak by antagonizing nodal signaling. *Dev. Cell* **3,** 735–744 (2002).

Development • Accepted manuscript

40. Lewis, S. L. *et al.* Dkk1 and Wnt3 interact to control head morphogenesis in the mouse. *Development* **135,** 1791–1801 (2008).
41. Morgani, S. M., Metzger, J. J., Nichols, J., Siggia, E. D. & Hadjantonakis, A.-K. Micropattern differentiation of mouse pluripotent stem cells recapitulates embryo regionalized cell fate patterning. *Elife* **7,** e32839 (2018).
42. D'Amour, K. A. *et al.* Production of pancreatic hormone–expressing endocrine cells from human embryonic stem cells. *Nat. Biotechnol.* **24,** 1392–1401 (2006).
43. Teo, A. K. K., Valdez, I. A., Dirice, E. & Kulkarni, R. N. Comparable generation of activin-induced definitive endoderm via additive Wnt or BMP signaling in absence of serum. *Stem Cell Reports* **3,** 5–14 (2014).
44. Yoney, A. *et al.* WNT signaling memory is required for ACTIVIN to function as a morphogen in human gastruloids. *Elife* **7,** e38279 (2018).
45. Voiculescu, O., Bodenstein, L., Lau, I. J. & Stern, C. D. Local cell interactions and self-amplifying individual cell ingression drive amniote gastrulation. *Elife* **3,** e01817 (2014).
46. Williams, M., Burdsal, C., Periasamy, A., Lewandoski, M. & Sutherland, A. Mouse primitive streak forms in situ by initiation of epithelial to mesenchymal transition without migration of a cell population. *Dev. Dyn.* **241,** 270–83 (2012).
47. Aulehla, A. & Pourquié, O. Signaling Gradients during Paraxial Mesoderm Development. *Cold Spring Harb. Perspect. Biol.* **2,** (2010).
48. Jaffe, L. F. Calcium waves. *Philos. Trans. R. Soc. B Biol. Sci.* **363,** 1311–1317 (2008).
49. Vergassola, M., Deneke, V. E. & Di Talia, S. Mitotic waves in the early embryogenesis of Drosophila: Bistability traded for speed. *Proc. Natl. Acad. Sci. U. S. A.* **115,** E2165–E2174 (2018).
50. Chang, J. B. & Ferrell Jr, J. E. Mitotic trigger waves and the spatial coordination of the Xenopus cell cycle. *Nature* **500,** 603–607 (2013).
51. Cong, L. *et al.* Multiplex Genome Engineering Using CRISPR/Cas Systems. *Science* **339,** 819–823 (2013).
52. Brinkman, E. K., Chen, T., Amendola, M. & Van Steensel, B. Easy quantitative assessment of genome editing by sequence trace decomposition. *Nucleic Acids Res.* **42,** (2014).
53. E-Cadherin (24E10) Rabbit mAb Datasheet. *Cell Signaling Technology* (2016). Available at: https://media.cellsignal.com/pdf/3195.pdf. (Accessed: 5th March 2017)
54. E-Cadeherin (EP700Y) Rabbit mAb Datasheet. *Abcam* Available at: https://www.abcam.com/e-cadherin-antibody-ep700y-intercellular-junction-marker-ab40772.html.

Development • Accepted manuscript

Figures

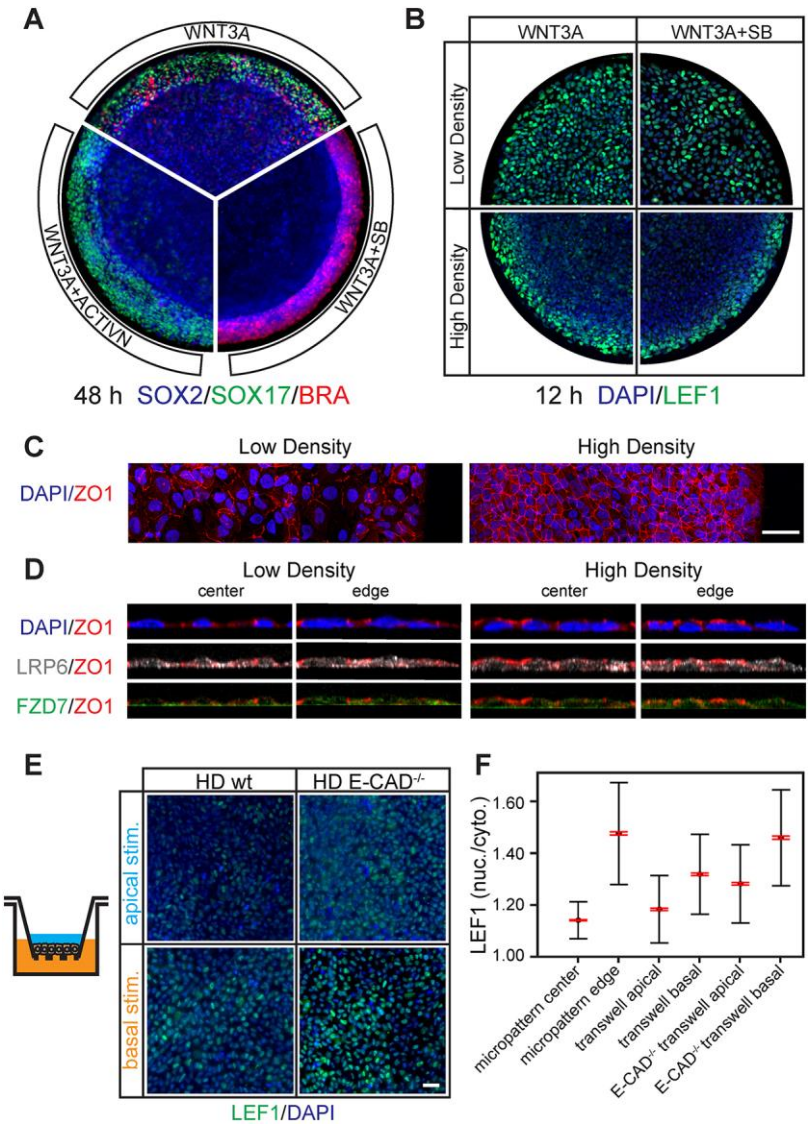

Figure 1 | WNT3A response is edge and density dependent

(A) Pie sections of representative 1,000µm diameter micropatterned hESC colonies stimulated with WNT3A, WNT3A+SB, or WNT3A+ACTIVIN and fixed and stained after 48h for germ layer markers. All micropattern experiments were performed on at least three separate occasions with similar results, and unless mentioned otherwise, all other micropatterns shown are 1,000 µm in diameter

Development • Accepted manuscript

(B) Micropatterns stimulated with WNT3A or WNT3A+SB at high density (22h after seeding, 3474 ± 430 cells/mm^2) or low density (8h after seeding, 1810 ± 236 cells/mm^2) and fixed and stained for LEF1 at 12h.

(C) Maximum intensity projection of tight junction marker ZO1 and nuclear marker DAPI in low density and high density micropatterns immediately prior to stimulation. Note that the network of tight junctions is only fully formed in the high density micropatterns. Scale bar, 50µm.

(D) Cross-sections showing the apical-basal position of WNT receptors relative to DAPI and ZO1 (apical marker). At high density the cells are in an apically-basally polarized epithelial state, as judged by the relative position ZO1 and DAPI. While not polarized themselves, the majority of the WNT receptors in this state do lie underneath the tight junctions, and so presumably are not be as accessible from the apical side as the basal side. This is in contrast to the low density state where cells are not epithelized and receptors are visible on both sides of ZO1. Additionally there is no significant edge-vs-center expression of the receptors at either density. Scale bar, 10µm.

(E) and (F). Basally stimulated high density hESCs in transwell filters show a higher WNT3A response than when apically stimulated. However, judging by the quantification of LEF1 nuclear to cytoplasmic ratio in (F), this difference is not enough to explain the edge-vs-center difference in micropatterns. It takes the knockout of E-CAD and basal stimulation to reach the micropattern edge level of WNT activation. The black error bars in (F) represent the standard deviation on 1,000 cells and the red error bars represent the standard error on the mean, illustrating the significant difference of the mean between each sample. The scale bar in (E) is 50µm.

Development • Accepted manuscript

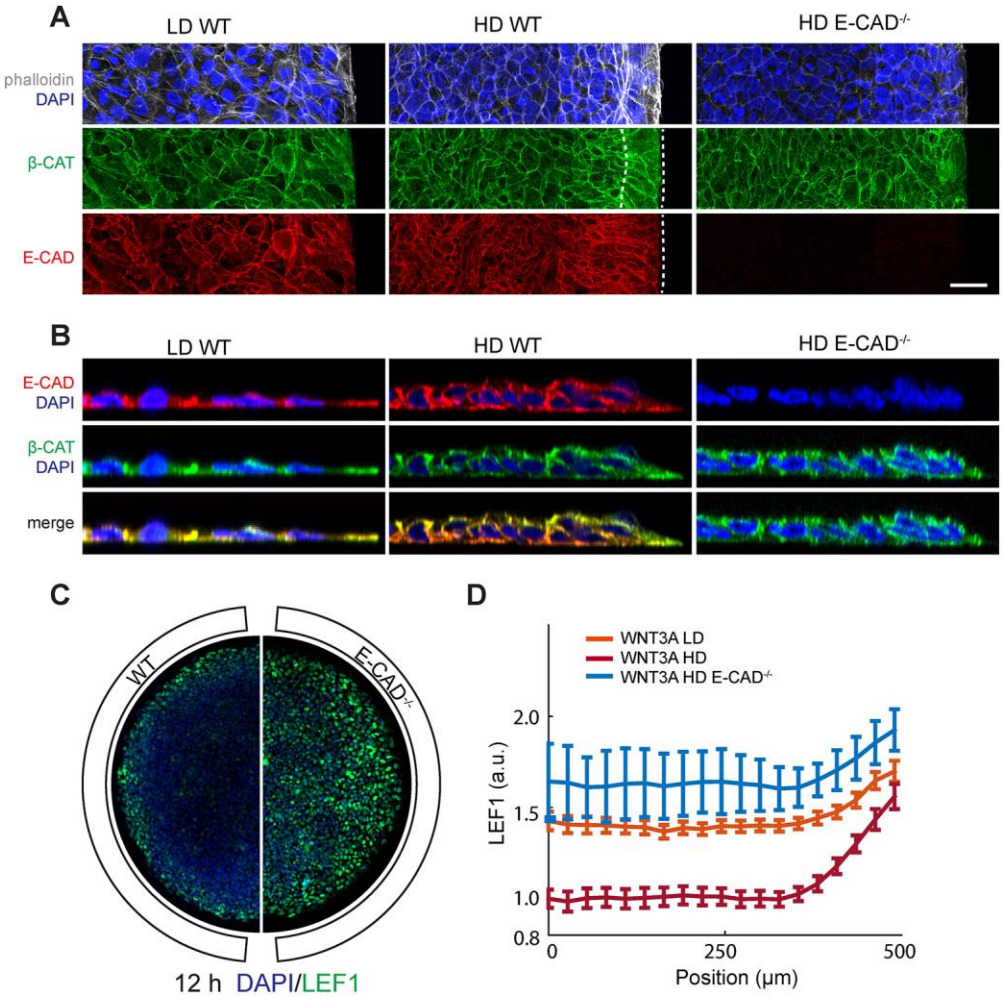

Figure 2 | E-CAD knockdown eliminates early WNT3A pattern

(A) Maximum intensity projection of DAPI, actin (marked via phalloiden), β-CAT, and E-CAD in low density wild type, high density wild type, and high density E-CAD$^{-/-}$ micropatterns immediately prior to WNT3A stimulation. Note the thick actin stress fibers (arrow) and cytoplasmic β-CAT (between the two dashed lines) only apparent on the edge of the high density wild type micropatterns, in the same region that shows the highest LEF1 response to WNT3A. Note also that outer facing side of cells on the micropattern edge are lower in E-CAD compared with sides of the same cells that that join with neighbouring cells (bottom dashed line). Scale bar, 50μm.

(B) Cross-section of micropatterns from (A) showing the overlap of E-CAD and β-CAT. In low density wild type micropatterns there is no significant asymmetry in E-CAD or β-CAT localization (superposition is yellow), but at high density one can see unmatched free β-CAT (green) on cells on the periphery of the micropattern (arrow). Scale bar, 10μm.

Development • Accepted manuscript

(C) 12h WNT3A response measure by LEF1 in high density wild type and E-CAD$^{-/-}$ micropatterns. Knockdown of E-CAD allows the WNT3A response to penetrate into the center of the micropattern.

(D) Quantification (C) and comparison to the low density wild type micropatterns. Single cell expression data was binned radially and averaged. The final radial profile represents the average of *n*=25 colonies. Error bars here and on all following graphs represents the standard deviation among colonies.

Development • Accepted manuscript

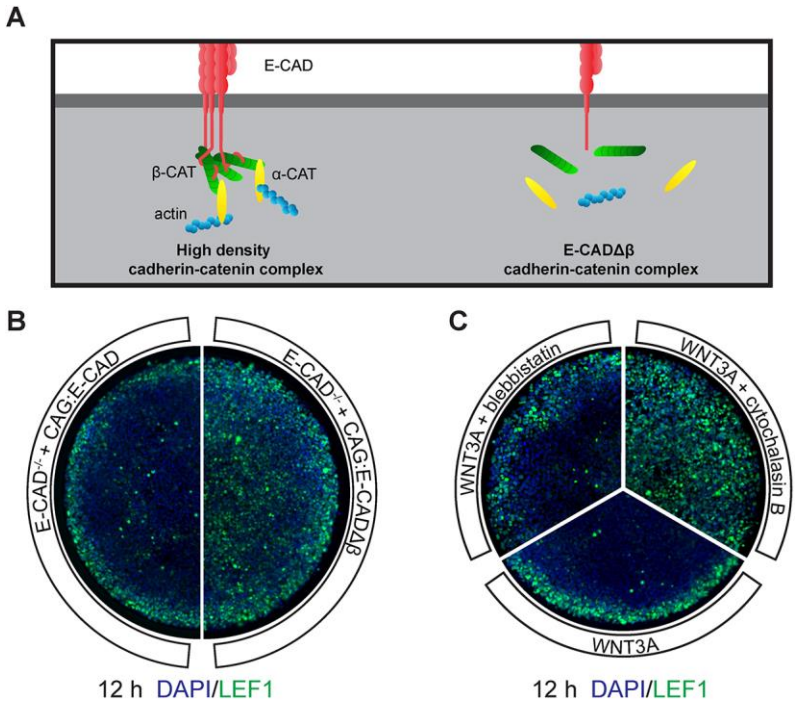

Figure 3 | Other perturbations to E-CAD-β-CAT-Actin connections also eliminate the early WNT3A pattern

(A) Cartoon showing the conventional model of how E-CAD, β-CAT, and the actin cytoskeleton connect to one another.

(B) E-CAD$^{-/-}$ cells rescued with constitutively expressed full length E-CAD or E-CADΔβ were put in high density micropatterns and stimulated with WNT3A for 12h and then stained for LEF1. The full length E-CAD micropatterns recovered the wild type phenotype whereas those with E-CADΔβ did not, showing that the β-CAT link to E-CAD is essential for the 12h WNT pattern.

(C) Wild type high density micropatterns stimulated with WNT3A, WNT3A+blebbistatin, or WNT3A+cytochalasin B, and stained for LEF1 after 12h. Blebbistatin blocks myosin II controlled actin contraction and cross-linking, whereas cytochalasin B more directly interferes with the actin cytoskeleton by reducing actin polymerization. Corresponding to this difference of degree of perturbation, we see a minor increase in the width of the LEF1 region with blebbistatin, and a more dramatic elimination of the LEF1 edge restriction with cytochalasin B.

Development • Accepted manuscript

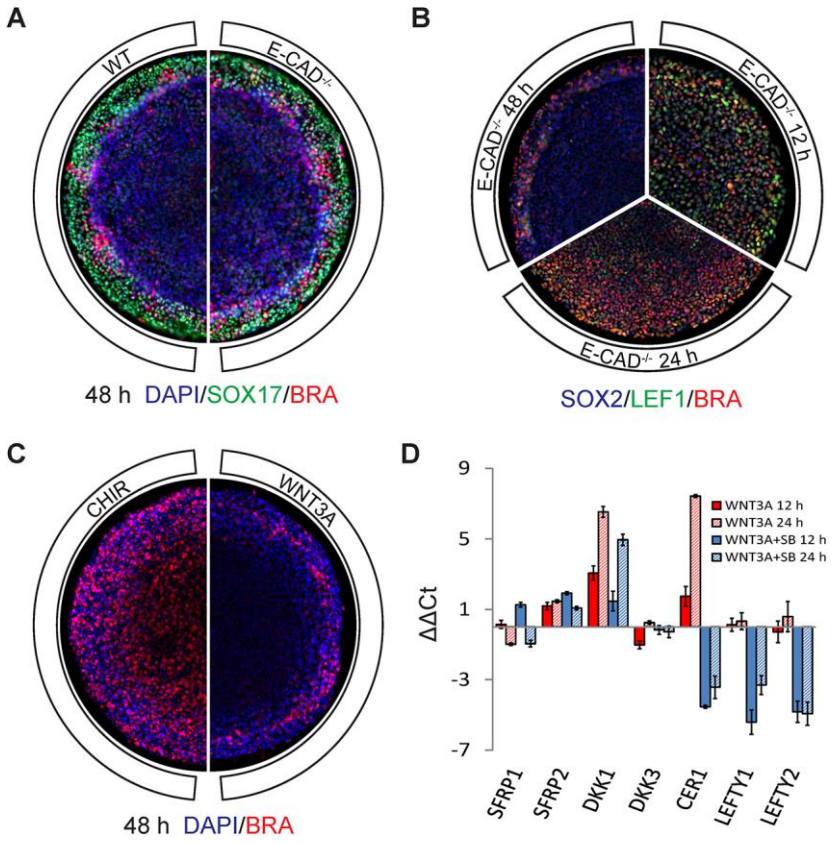

Figure 4 | E-CAD does not explain long term WNT patterning, WNT3A also induces WNT and NODAL inhibitors

(A) High density wild type and E-CAD$^{-/-}$ micropatterns fixed and stained for indicated markers after 48h of WNT3A stimulation.

(B) Time-course of LEF1 and BRA expression in high density E-CAD$^{-/-}$ micropatterns. Note that as time progresses the signalling response is gradually excluded from the colony center.

(C) High density E-CAD$^{-/-}$ micropatterned colonies stimulated with 6μM CHIR or WNT3A and fixed and stained for BRA after 48h. The dramatic difference between the two indicates that extra-cellular regulation of the WNT3A pathway may be a dominant factor, since CHIR is a small molecule and acts intercellularly, skipping extracellular regulation.

(D) qPCR of secreted inhibitors of interest upon 12 and 24h of WNT3A or WNT3A+SB stimulation in micropatterned colonies. Note that the NODAL inhibitors are all severely downregulated when one inhibits the NODAL receptor with SB. (Note also that Conditioned Media also has endogenous ACTIVIN/NODAL activity that would contribute to the effect seen with SB even though no additional ACTIVIN was added).

Development • Accepted manuscript

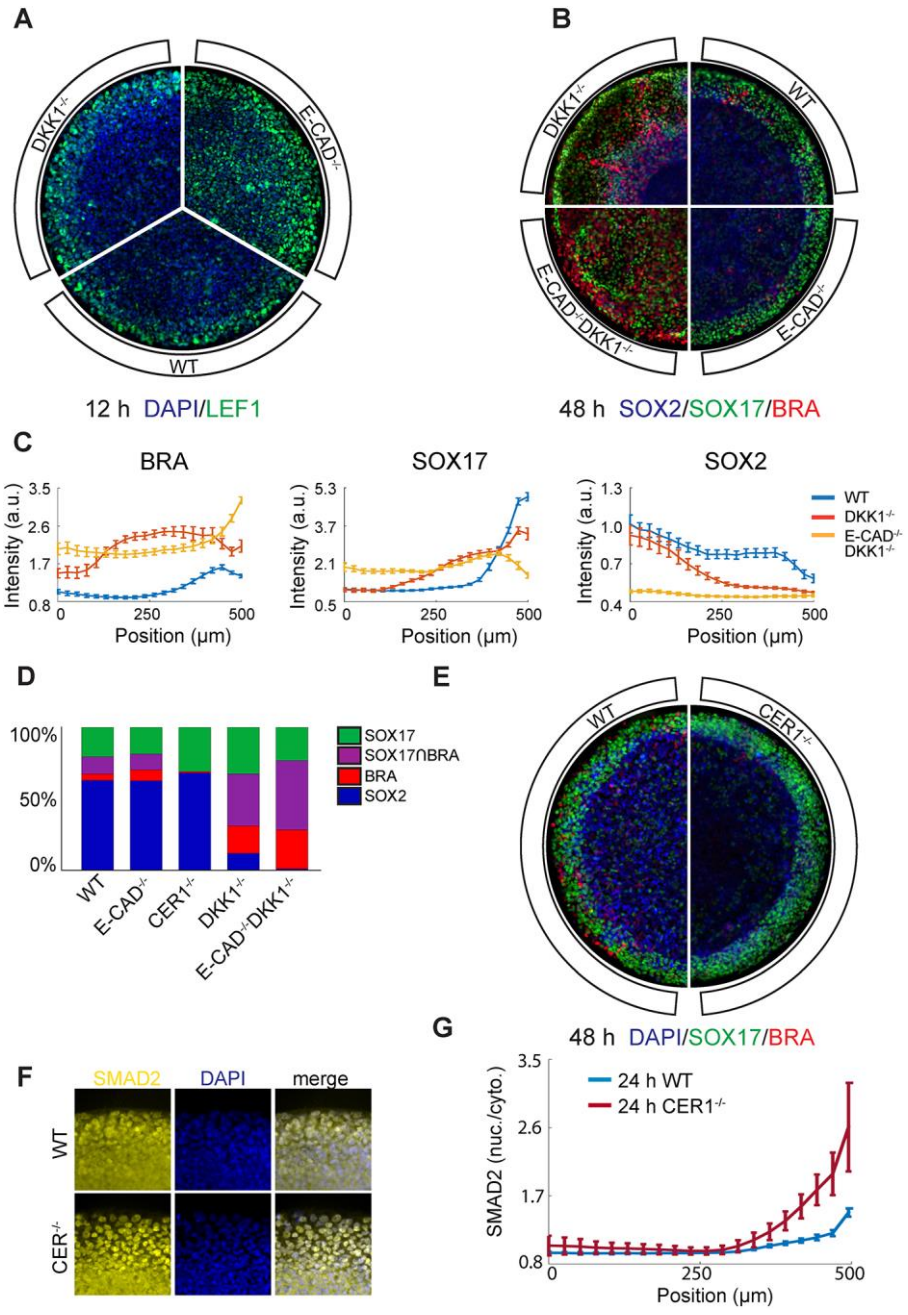

Figure 5 | DKK1 controls spatial extent of WNT3A patterning and CER1 influences the mesoderm vs endoderm fate decision

(A) Comparison of 12h WNT3A response in high density micropatterns of DKK1$^{-/-}$ cells vs E-CAD $^{-/-}$ cells vs wild type cells. As expected (since no DKK1 is transcribed in pluripotency) DKK1$^{-/-}$ micropatterns resemble wild type micropatterns and are less sensitive to WNT3A than E-CAD$^{-/-}$ cells.

Development • Accepted manuscript

(B) After 48h of WNT3A stimulation on high density micropatterns, DKK1$^{-/-}$ cells show a dramatic increase in WNT3A patterned region compared with E-CAD$^{-/-}$ and wild type cells. DKK1 and E-CAD also act synergistically, as loss of both genes cause complete loss in the edge restriction of WNT3A patterning.

(C) Quantification of IF for pluripotency marker SOX2 and differentiation markers SOX17 and BRA in DKK1$^{-/-}$, E-CAD$^{-/-}$, and DKK1$^{-/-}$E-CAD$^{-/-}$ cells (*n*=20 colonies per condition) following B.

(D) Classification of cells from wild type, CER1$^{-/-}$, DKK1$^{-/-}$, E-CAD$^{-/-}$, and DKK1$^{-/-}$E-CAD$^{-/-}$ micropatterns into 4 different subpopulations. Classification was performed by fitting single cell SOX17, BRA, and SOX2 levels to a Gaussian mixture model (See Methods and Figure S5). Note that in addition to increasing the spatial extent of WNT3A patterning, DKK1 also influences the proportion of differentiated cells that commit to either mesoderm (BRA) or endoderm (SOX17), with significantly more cells expressing BRA when DKK1 is knocked out. Note also the decline in BRA cells in the CER1$^{-/-}$ micropatterns compared to the wild type.

(E) Comparison of wild type and CER1$^{-/-}$ micropatterns after 48h of WNT3A stimulation. Notice the higher number of BRA cells in the wild type.

(F) SMAD2 levels and the ring of activity are increased in CER1$^{-/-}$ cells compared to wild type (micropatterns stimulated with WNT3A, fixed and stained after 48h). Scale bar, 50µm.

(G) Quantification of F, *n*=20 colonies per condition.

Development • Accepted manuscript

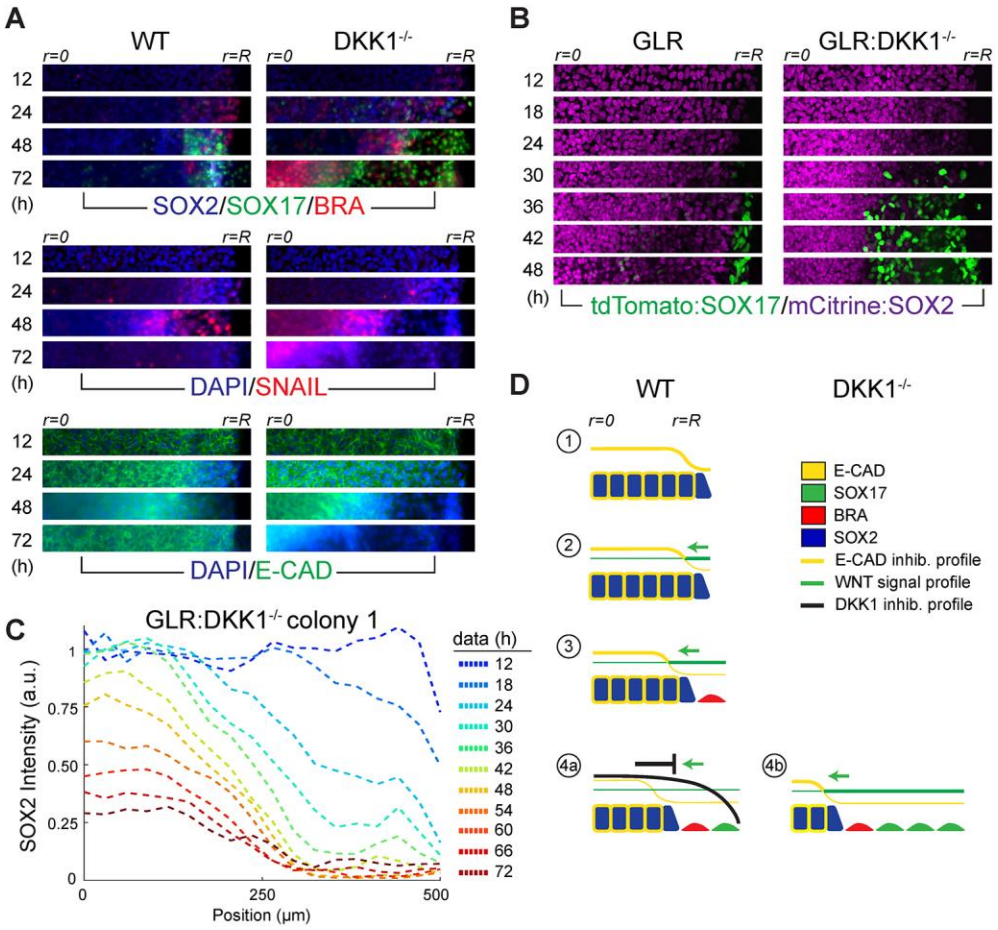

Figure 6 | Patterning via a WNT/EMT wave

(A) Radial sections of WNT3A stimulated high density wild type or DKK1$^{-/-}$ micropatterns fixed and stained for the indicated markers at the indicated times. Interior of each colony (r=0) is on the left of each section, the edge of the colony (r=R) is on the right.

(B) Time-lapse radial sections of WNT3A stimulated high density GLR micropattern and GLR:DKK1$^{-/-}$ micropattern. Ten micropatterns for each condition were imaged in the same session, and the examples shown here are representative. One notes that SOX17 turns on slightly earlier in the GLR:DKK1$^{-/-}$ micropatterns than in the GLR micropatterns, and that, as with the immunostaining data, a wave of SOX2 downregulation and differentiation starts on the periphery. This wave halts in the GLR line, but continues proceeding inward in the GLR:DKK1$^{-/-}$ micropatterns.

(C) Quantification of single-cell SOX2 expression in the same GLR:DKK1$^{-/-}$ micropattern shown in (B).

Development • Accepted manuscript

(D) Qualitative model of WNT/EMT wave spreading and stabilization. ①: prior to WNT3A stimulation E-CAD creates a bias so that only cells on the immediate periphery are sensitive to WNT ligand. ②: Application of WNT3A ligand results in only boundary cells responding and differentiating. ③: As these cells undergo EMT, they lose E-CAD junctions and expose interior cells, enabling them now to respond to the WNT ligand. ④: If checked by secreted DKK1 from the differentiating cells, however, the boundary cells become protected from WNT ligand and the wave stops, as illustrated in (a); if left unchecked, this cycle will enable a wave of differentiation to travel progressively across the colony from outside to inside, as illustrated in (b).

Development • Accepted manuscript

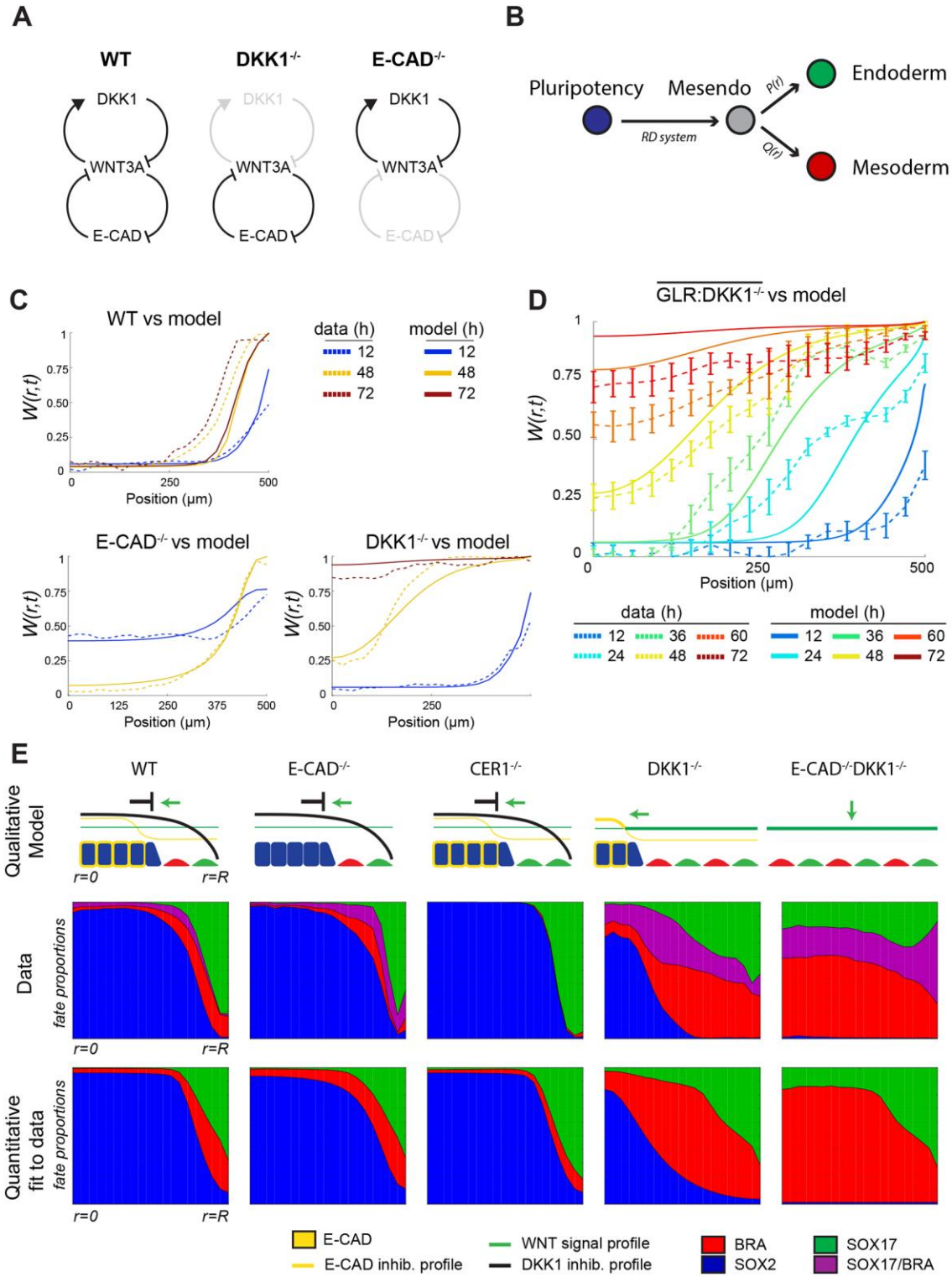

Development • Accepted manuscript

Figure 7 | A quantitative model of WNT patterning dynamics in the PS

(A) Gene regulatory network of WNT3A, E-CAD, and DKK1 used in the model. Note how the DKK1$^{-/-}$ and E-CAD$^{-/-}$ cell lines can be used to simplify this network and fit the subcomponents separately.

(B) Simple model of mesoderm versus endoderm fate decision. The reaction-diffusion (RD) system determines the probability that a cell at a given radius in a given background commits to differentiate by going from the pluripotent state to the intermediate mesdendo state. Once there, the probability *P(r),* which is a linearly rescaled function of radial nuclear SMAD2 profile, is used to determine the probability of cell going to endoderm versus mesodederm.

(C) Comparison of the simulated PDE model to the WT, DKK1$^{-/-}$, and E-CAD$^{-/-}$ data. The fit was made using the 12h LEF1 response (Figure 2D), the 48h differentiated cell response (i.e. 1–SOX2 population) shown in Figure S5C, and the 72h differentiated cell response (again 1–SOX2 population) shown in Figure S5D. The remaining data plotted are model predictions.

(D) WNT/EMT wave in the DKK1$^{-/-}$ micropatterns. Solid lines are the model predictions, dashed lines and error bars represent the average and standard deviation of 10 continuously imaged GLR:DKK1$^{-/-}$ micropatterns, respectively.

(E) Qualitative diagram of WNT patterning dynamics for each genetic background, and fit of quantitative model to the data. For the data, single cells from the 48h micropatterns of each genetic background were classified into 4 different subpopulations according to a Gaussian mixture model based on SOX17, BRA, and SOX2 levels (see Methods). Classified cells were then further subdivided according to their radial position and the population was normalized, allowing us thus to obtain the probability of belonging to a specific fate at a specific radii given a specific genetic background.

Development • Accepted manuscript

Supplementary Information: Supplemental Tables

Table S1: Antibody information

Antigen	Antibody	Dilution
Active β-CATENIN	Millipore 05-665	1:400
BRACHYURY	R&D Systems AF-2085	1:300
E-CADHERIN	Cell Signalling 3195	1:200
E-CADHERIN	Abcam 40772	1:400
FRZD7	R&D Systems MAB1981	1:200
LEF1	Cell Signalling 2230	1:200
LRP6	R&D Systems 1505	1:100
N-CADHERIN	BioLegend 350802	1:200
SMAD2	BD bioscience 610842	1:100
SOX17	R&D Systems AF-1924	1:200
SOX2	Cell Signalling 3579	1:200

Table S2: RT-QPCR Primer designs

Gene Symbol	Forward primer	Reverse Primer
AXIN2	ctccccaccttgaatgaaga	tggctggtgcaaagacatag
BRACHYURY	catgcaggtgagttgtcagaa	gctgtgacaggtacccaacc
CER1	gccatgaagtacattgggaga	cacagccttcgtgggttatag
DKK1	ccttggatgggtattccaga	cctgaggcacagtctgatga
DKK3	agagcctgatggagccttg	ggcttgcacacatacaccag
LEF1	agatcaccccacctcttgg	atgagggatgccagttgtgt
LEFTY1	ctgcacaccctggacctt	atcccctgcaggtcaatgta
LEFTY2	cctggacctcagggactatg	atcccctgcaggtcaatgta
SFRP1	gctggagcacgagaccat	tggcagttcttgttgagca
SFRP2	gctagcagcgaccacctc	tttttgcaggcttcacatacc

Development • Supplementary information

Table S3: sgRNA designs

Gene Symbol	Forward primer	Reverse Primer
CER1	caccgcttcctcatggttgcctgt	aaacacaggcaaccatgaggaagc
DKK1	caccgtctggtacttattcccgcc	aaacggcgggaataagtaccagac
DKK3	caccgtctcattgtgatagctggg	aaaccccagctatcacaatgagac
E-CAD	caccgcagcagcagcagcgccgag	aaacctcggcgctgctgctgctgc
LEFTY1	caccggtcatccccacccacgtga	aaactcacgtgggtggggatgacc
SFRP1	caccggagcacgagaccatggcgg	aaacccgccatggtctcgtgctcc
SFRP2	caccggtggtcgctgctagcgagg	aaaccctcgctagcagcgaccacc

Table S4: Knockout lines

Target	Separate clones
RUES2:DKK1$^{-/-}$	3
RUES2-GLR:DKK1$^{-/-}$	2
RUES2:DKK3$^{-/-}$	2
RUES2:E-CAD$^{-/-}$	2
RUES2:CER1$^{-/-}$	1
RUES2:LEFTY1$^{-/-}$	1
RUES2:SFRP1$^{-/-}$	1
RUES2:SFRP2$^{-/-}$	1
RUES2:SFRP1$^{-/-}$SFRP2$^{-/-}$	1
RUES2:LEFTY1$^{-/-}$CER1$^{-/-}$	1

Development • Supplementary information

Supplementary Information: Supplemental Figures

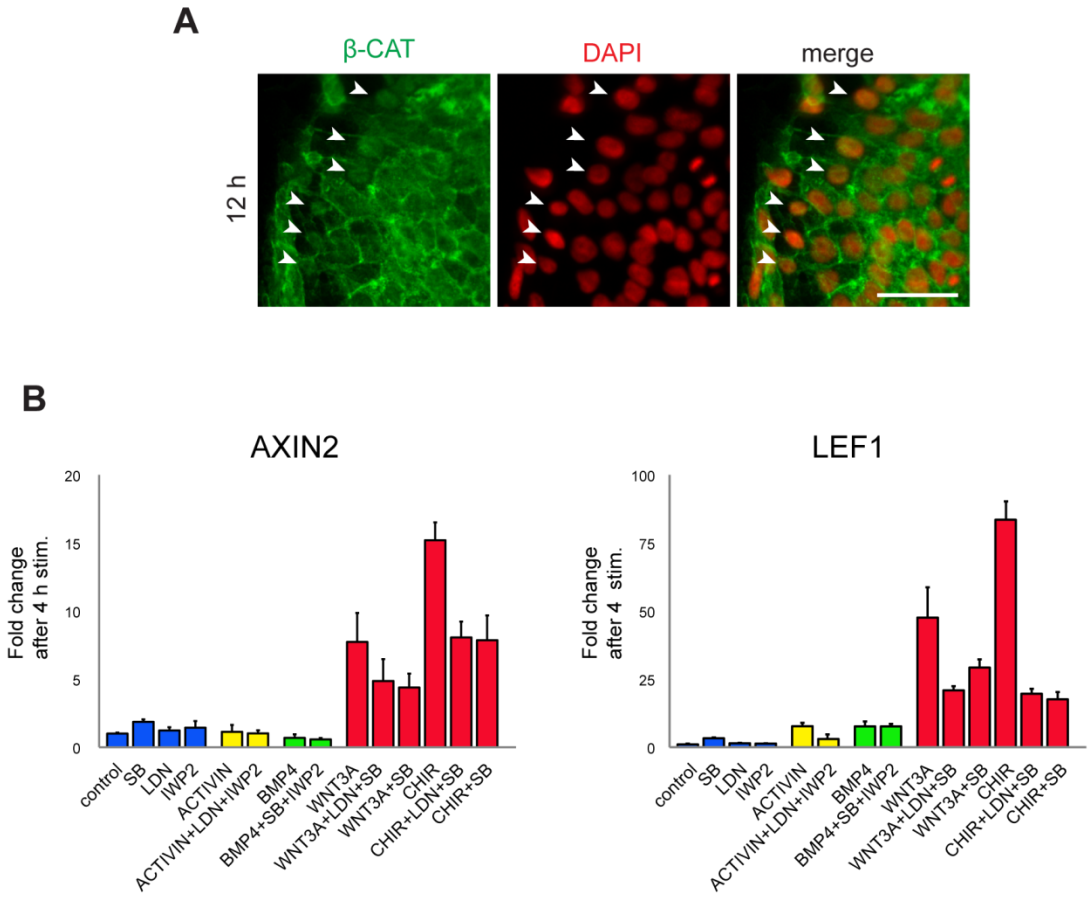

Figure S1 | WNT3A response markers

(A) Inset of an abnormally low density micropattern colony stimulated with WNT3A and fixed and stained at 12h for active β-CATENIN. Even at this low density (seeded with $6x10^5$ cells, stimulated 2 hours after seeding) an increase in β-CAT in the nucleus is only visible in loosely connected cells on the colony edge (arrows). Nuclear β-CATENIN in cells away from the periphery or at higher density (including standard low density conditions) is not easily observed, largely due to signal from membrane-bound or cytoplasmic regions. Scale bar, 50µm.

(B) qPCR of AXIN2 and LEF1 as a function of inputs arrayed on x-axis. The results show that the LEF1 and AXIN2 response is dominated by WNT3A, though synergism with the NODAL pathway is significant as well, as can be seen by comparing WNT3A or CHIR with WNT3A+SB or CHIR+SB. Thus LEF1 and AXIN2 can be used as proxies for early WNT3A response. Also note that LEF1 gives a greater positive signal than AXIN2, reaching 84-fold induction compared with 15 fold induction for CHIR condition.

Development • Supplementary information

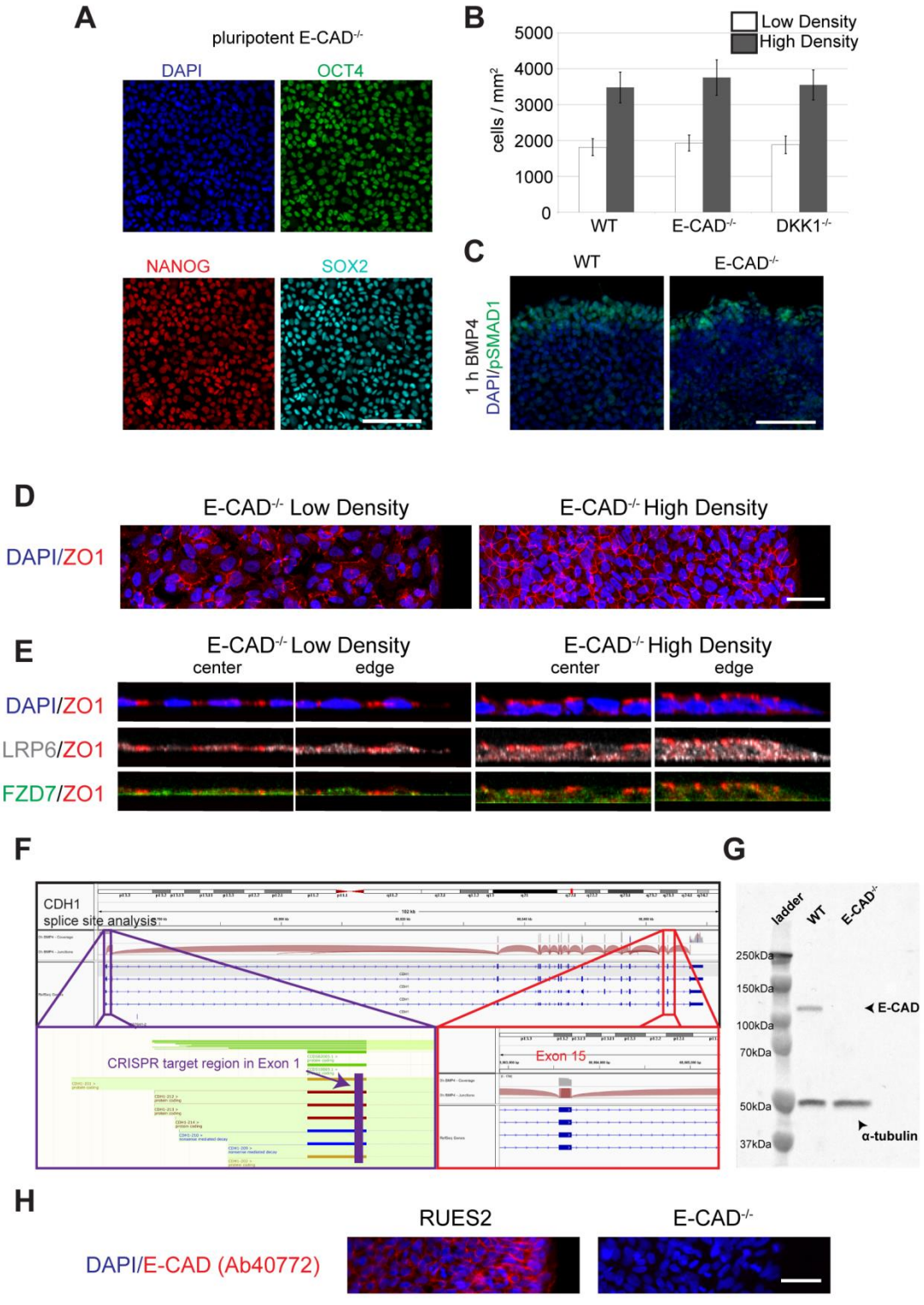

Development • Supplementary information

Figure S2 | Epithelial integrity is preserved in E-CAD$^{-/-}$ cells.

(A) E-CAD$^{-/-}$ cells maintain pluripotency markers even with continual passaging (i.e. >20 passages). Images are of unpatterned, standard hESC culture colonies. Scale bar, 100µm.

(B) E-CAD$^{-/-}$ cell seeding efficiency and growth is similar to wild type and DKK1-/- cell lines.

(C) Test of epithelial integrity and BMP4 response. Edge of high density wild type and E-CAD$^{-/-}$ micropatterns stimulated with BMP4 and fixed and stained for pSmad1 after 1h. As in the wild type, pSMAD1 expression is restricted to the periphery in E-CAD$^{-/-}$ colonies. Scale bar, 100µm.

(D) Maximum intensity projection of ZO1 and DAPI in low density and high density E-CAD$^{-/-}$ micropatterns immediately prior to stimulation. The network of tight junctions is the same as in the wild type (Figure 1C). Scale bar, 50µm.

(E) Cross-sections showing the apical-basal position of WNT receptors relative to DAPI and ZO1. Result is the same as for wild type micropaterns (Figure 1D). Scale bar, 10µm.

(F) Top: sashimi plot in Integrative Genomics Viewer of E-CAD region from previously published RNA-seq data set[1] showing exon splicing pattern observed in RUES2 cells in pluripotency conditions. Bottom left: zoom of Exon 1 region in Ensembl viewer showing the four different E-CAD isoforms and the sgRNA CRISPR targeting site used. Bottom right: zoom of Exon 15 region that the Cell Signalling 3195 E-CAD antibody targets. As one can see from the plot, there is no isoform that skips this exon.

(G) Western blot of pluripotent wild type and E-CAD$^{-/-}$ cells for E-CAD and α-tubulin. One can see that while E-CAD and α-tubulin are detected in the wild type cells, only α-tubulin is visible in the knockout cell line.

(H) Staining of pluripotent wild type and E-CAD$^{-/-}$ cells with Abcam anti-E-CADHERIN ab40772 antibody that targets amino acids 600-700. One can see that while E-CAD is detected in the wild type cells, no E-CAD is visible in the knockout cell line. Scale bar, 50µm.

Development • Supplementary information

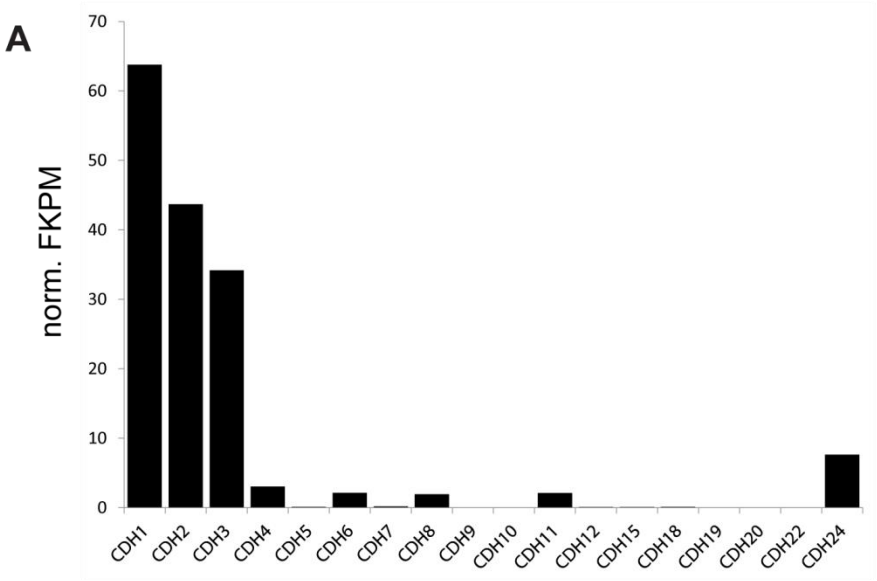

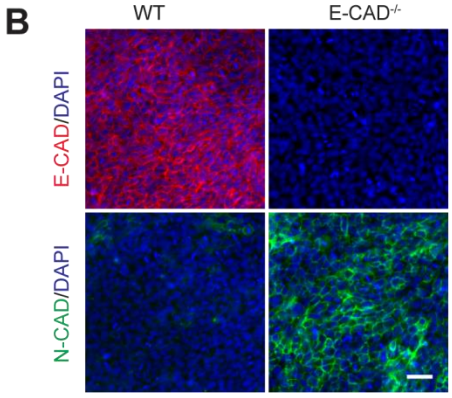

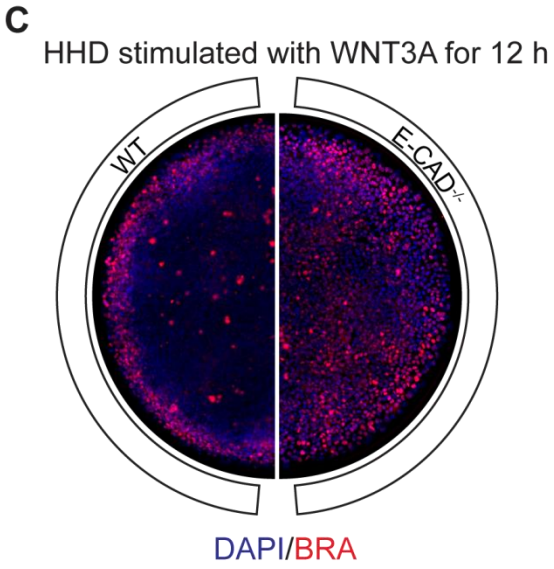

Development • Supplementary information

Figure S3 | A change in the protein expression profile of N-CADHERIN occurs in the E-CAD$^{-/-}$ cell line.

(A) RNA-seq profiling for all classic cadherins in pluripotent hESCs. Since the E-CAD (CDH1) knockout is lethal in mouse at the post-compaction stage, we were somewhat surprised at the lack of an E-CAD$^{-/-}$ pluripotent phenotype (Supplemental Figure 2). However both N-CADHERIN and P-CADHERIN (CDH2,CDH3) are substantially expressed at the mRNA level in hESCs in pluripotency.

(B) Stain for N-CAD and E-CAD in wild type and E-CAD$^{-/-}$ in unpatterned pluripotent colonies. Antibody stain for E-CAD confirms that gene is knocked out in E-CAD$^{-/-}$ cells. More interestingly, while N-CAD is barely visible in wild-type cells, N-CAD is highly expressed and membrane localized in E-CAD$^{-/-}$ cells. Thus there is a reservoir of N-CAD message in hESC that is only expressed in the absence of E-CAD, which may be a consequence of the same pathway that up regulates N-CAD during EMT when the transcription of E-CAD is abrogated by SNAIL. Interestingly, other research has shown that the artificial replacement E-CAD protein by N-CAD protein in the mouse intestine after gastrulation showed that N-CAD could fulfill the structural role of E-CAD, but the replacement lead to an up-regulation of WNT signalling that is also consistent with our findings[2]. Scale bar, 50µm.

(C) 12h WNT3A response measured by BRA in high high density (HHD) wild type and E-CAD$^{-/-}$ micropatterns. HHD micropatterns are left to grow for an additional 36h beyond that of HD micropatterns before stimulating with WNT3A. One sees that even at this extreme the knockdown of E-CAD allows a WNT3A response into the center of the micropattern.

Development • Supplementary information

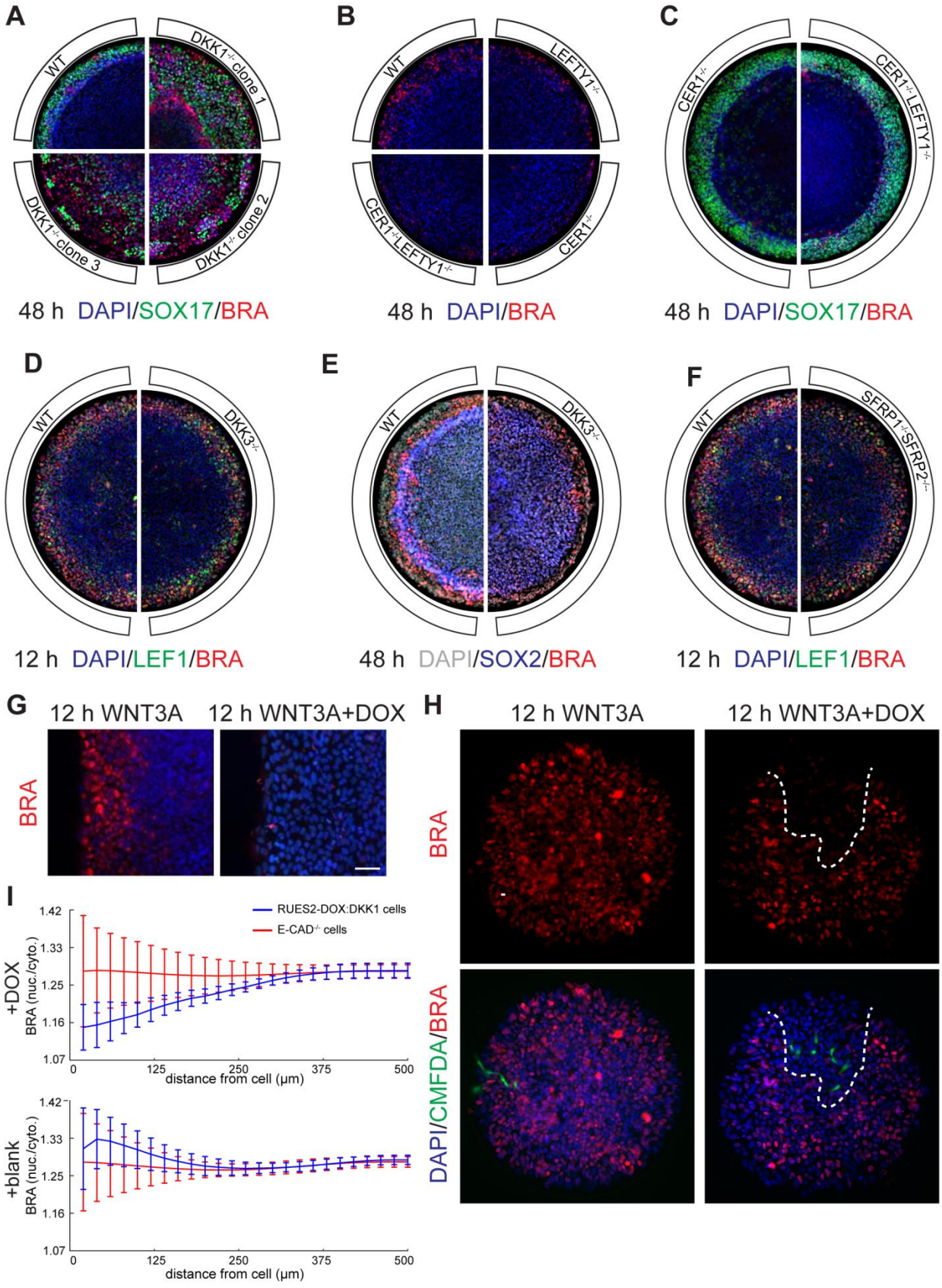

Development • Supplementary information

Figure S4 | Other inhibitor CRISPR knockout line and clones

(A) Other DKK1$^{-/-}$ clonal lines with different frameshift mutations also exhibit the same micropattern phenotype when stimulated with WNT3A at high density and fixed and stained after 48 hours.

(B) No discernible difference in SOX17 expression at 48h between CER1$^{-/-}$ and CER1$^{-/-}$LEFTY1$^{-/-}$ micropatterns under WNT3A stimulation.

(C) LEFTY1$^{-/-}$ micropatterns show no discernible difference with wild type micropatterns in number of BRA cells. However, both CER1$^{-/-}$ and CER1$^{-/-}$LEFTY1$^{-/-}$ (with a different CER1 frameshift mutation) show similar phenotype in having fewer BRA cells. Thus CER1$^{-/-}$ and not LEFTY1$^{-/-}$ is the main NODAL inhibitor during WNT induced patterning.

(D) and (E) No discernible difference at 12h or 48h between wild type and DKK3$^{-/-}$ micropatterns under WNT3A stimulation.

(F) No discernible difference at 12h between wild type and SFRP1$^{-/-}$SFRP2$^{-/-}$ micropatterns under WNT3A stimulation.

(G) Edge of a high density 1000µm diameter RUES2-DOX:DKK1-V5 micropattern. Cells were either given DOX or blank media for 12 h and then stimulated with WNT3A for a further 12 h (again with or without DOX continuing the pre-treatment). Cells were then stained for BRA. Scale bar, 50µm.

(H) 500µm diameter E-CAD$^{-/-}$ micropatterns seeded with 1% CMFDA cell tracker marked RUES2-DOX:DKK1-V5 cells (green). Cells were either given DOX or blank media for 12 h immediately after RI removal, and then stimulated with WNT3A for a further 12 h (again with or without DOX continuing the pre-treatment). Micropatterns were then fixed and stained for DAPI and BRA. In the DOX induced micropatterns one can see a BRA exclusion zone around the DKK1 expressing cells (marked roughly with dashed line).

(I) Quantification of (H). 5 DOX-induced and 5 blank stimulated micropatterns were segmented and all cells were first classified as either RUES2-DOX:DKK1-V5 (green) or E-CAD$^{-/-}$ cells. For each cell the nuclear to cytoplasmic ratio of BRA in all neighbouring cells within radius r (x-axis) was calculated and averaged. These averages were then averaged across all cells of their cell type (50 for RUES2-DOX:DKK1-V5, and 5000 for E-CAD$^{-/-}$) and plotted as shown with error bars indicating the standard deviation. One can see that in the DOX induced micropatterns the cells neighbouring the RUES2-DOX:DKK1-V5 cells show lower BRA than the average, and this effect is half-maximal at a distance of ~130µm, showing long-range action. This shielding does not happen when one looks at just neighbours of E-CAD$^{-/-}$cells, or in the blank stimulated micropatterns.

Development • Supplementary information

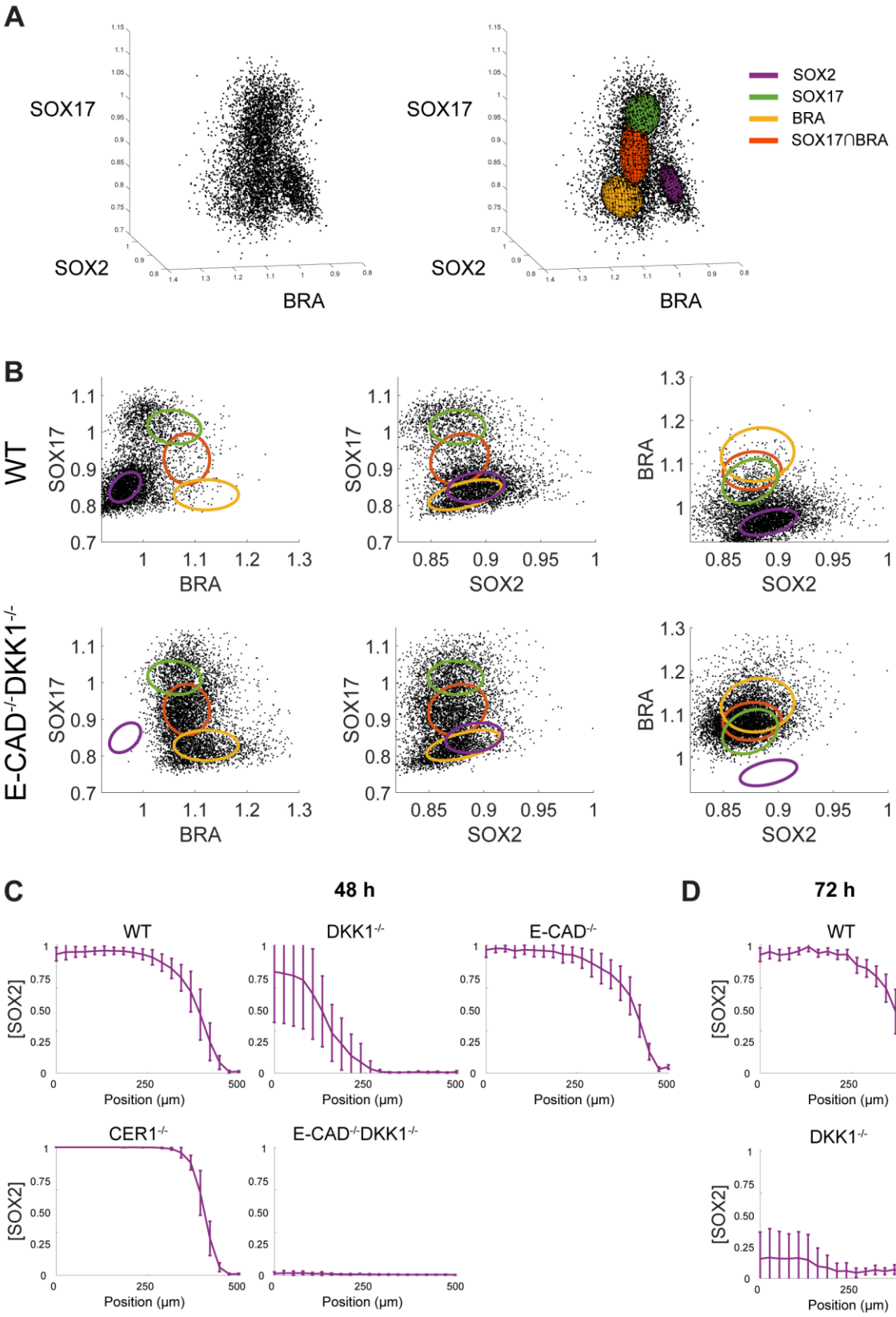

Development • Supplementary information

Figure S5 | Fate clustering and classification

(A) 3D scatterplots of combined cells from wild type, DKK1$^{-/-}$, E-CAD$^{-/-}$, E-CAD$^{-/-}$DKK1$^{-/-}$, and CER1$^{-/-}$ 48 h micropatterns data showing clustering into the Gaussian mixture model used for Figure 5D.

(B) Example scatterplots of cells from wild type and E-CAD$^{-/-}$DKK1$^{-/-}$ micropatterns projected into 2D for better visualization of the clustering.

(C) Proportion of cells classified as SOX2+ at 48 h plotted as a function of radius. Error bars represent the standard deviation of *n=20* colonies.

(D) Proportion of cells from micropatterns in Figure 6A classified as SOX2+ at 72 h plotted as a function of radius. Error bars represent the standard deviation of *n=20* colonies.

Development • Supplementary information

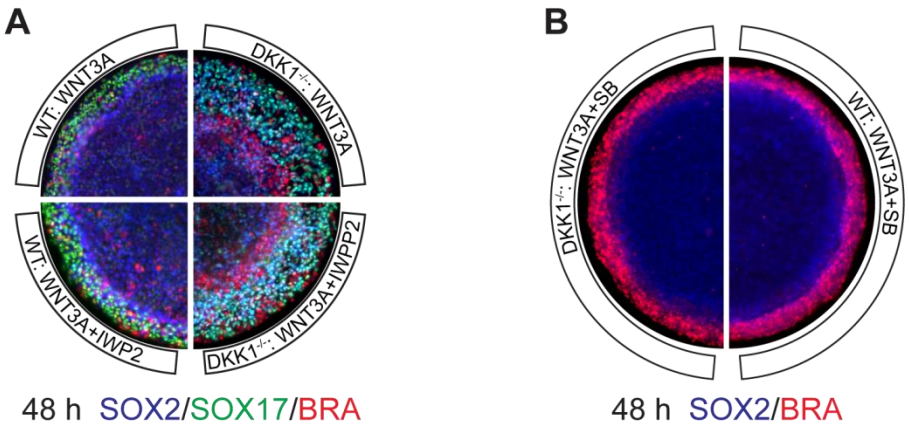

Figure S6 | Endogenous WNT signalling has little effect on patterning

(A) Wild type and DKK1$^{-/-}$ high density micropatterns stimulated with either WNT3A or WNT3A+IWP2 for 48h and stained for BRA, SOX2, and SOX17. No significant differences between wild type IWP2 and non-IWP2 or DKK1$^{-/-}$ IWP2 and non-IWP2 stimulated colonies were observed.

(B) Wild type and DKK1$^{-/-}$ high density micropatterns stimulated with WNT3A+SB for 48h and stained for BRA and SOX2.

Development • Supplementary information

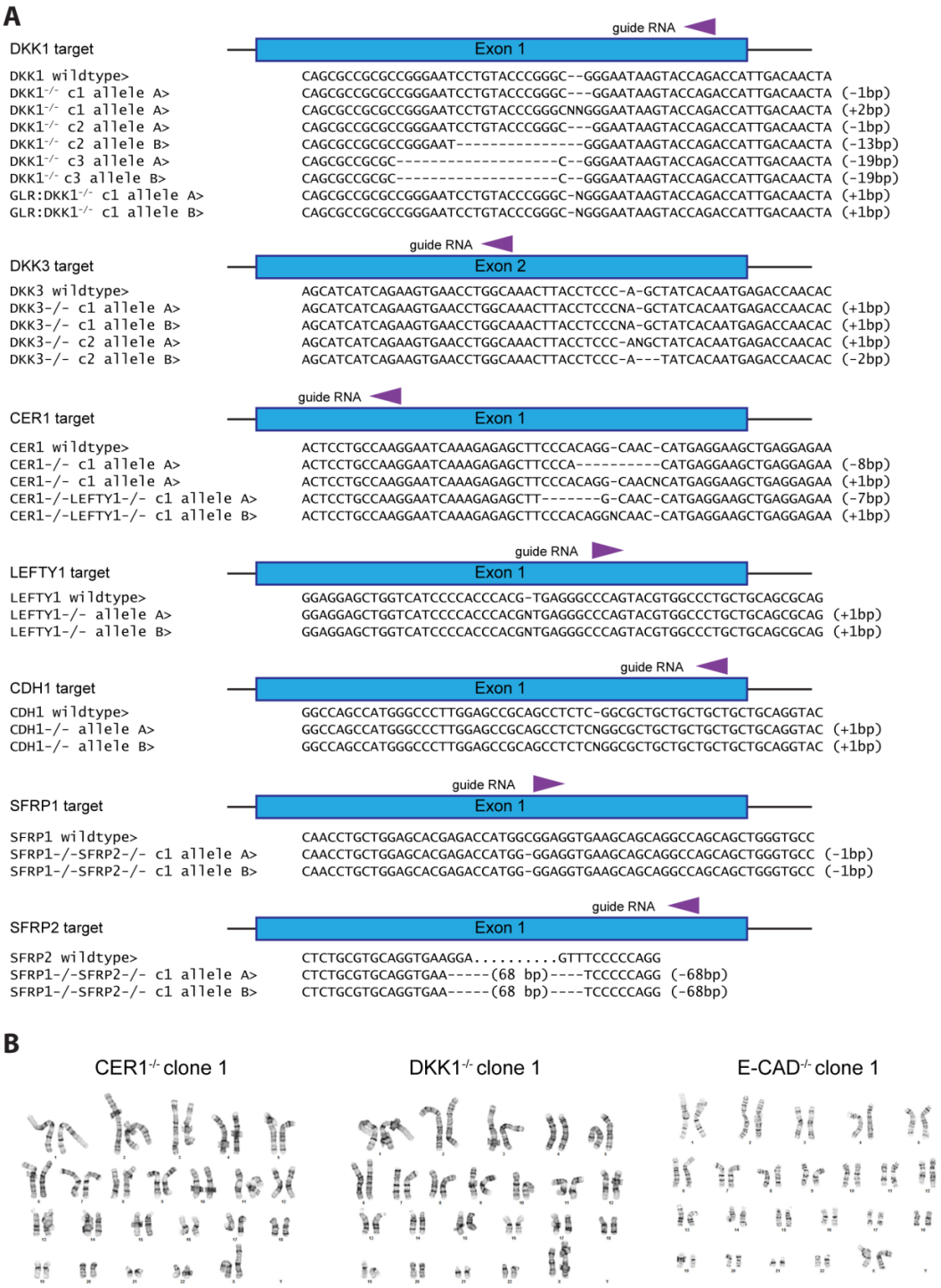

Figure S7 | Confirmation of CRISPR knockouts

(A) Sequences of the mutated alleles in the CRISPR/Cas9 knockout cell lines.

(B) The E-CAD$^{-/-}$ clone 1, DKK1$^{-/-}$ clone 1, and CER1$^{-/-}$ clone 1 cell lines were karyotypically normal.

Development • Supplementary information

Supplementary Information: Modelling

1 Overview

In this supplement we present a minimal model that fits the micropattern WNT3A phenotype data for each CRISPR knockout cell line. The four key features of this data that the model captures are:

1. The geometric edge bias mediated by E-CAD.
2. The edge restriction of the WNT response by the secreted inhibitor DKK1.
3. The edge-to-interior EMT and WNT response wave, as especially observed in the DKK1$^{-/-}$ line.
4. The bifucation of WNT differentiated cells to mesoderm versus endoderm depending on the relative levels of NODAL signal received.

To capture the first three features we need a model with two spatial diffusion terms: (1) to describe the spreading of DKK1 and its loss from the colony edge, and (2) to describe the implicit cell-cell communication via E-CAD that is responsible for the EMT wave as explained in the main text. As will be shown, this part of the model will give us the WNT signal received by cells at a given radius at a given time and can be used to determine the proportion of differentiated cells at 48hrs after stimulation. As will also be shown, this part of the model consists of 10 parameters, 4 of which can be independently fitted to the E-CAD$^{-/-}$ phenotype, 5 of which can be fitted independently to the DKK1$^{-/-}$ phenotype, and 1 which can be estimated from the E-CAD$^{-/-}$DKK1$^{-/-}$ cell line.

To capture the last feature (the bifurcation of differentiated cells into either mesoderm or endoderm), ideally one would use detailed data of the gene regulatory networks for mesendoderm formation and mesoderm and endoderm bifurcation. However, these are not known to the required level of detail, and so we instead simply use the NODAL signalling level as defined by nuclear SMAD2 to determine fates, with cells with higher nuclear SMAD2 being more likely to be directed to endoderm rather than mesoderm.

2 PDE System

In the first part of the model we need to track three quantities: the WNT response, the level of DKK1, and the level of E-CAD. We let $W(r,t)$ represent the WNT response, we let $I(r,t)$ represent DKK1, and we let $E(r,t)$ represent E-CAD. is the only quantity that we measure experimentally and that we use to fit the model (measured as nuclear LEF1 at 12hrs and at late times, the relative loss of SOX2 i.e., 1-SOX2 after rescaling). Since all of the relevant experiments were conducted on 1000μm diameter disc micropatterns, this 2D geometry is the only geometry we consider in our model as well (though it can be easily generalized to other geometries).

Initial conditions: We assume that W)and $I(r,t)$ are off everywhere and that is uniformly on. For the boundary condition on), we take this variable to be cell intrinsic, thus there is no diffusion of $W(r,t)$.

Boundary conditions: For the boundary condition on $I(r,t)$, we assume that it behaves like the BMP secreted inhibitor NOGGIN in the modelling of Etoc et al[1]. Thus DKK1 can freely diffuse over the colony

Development • Supplementary information

and is quickly lost to the media on the edge, giving the boundary condition $I(R,t) = 0$. Finally, for $r,t)$, since the E-CAD state of a cell also depends on its neighbours, we allow for a simple diffusion-like coupling with strength D_E. We do not initially know the scale of this dependence, whether it just immediate neighbours or if the coupling is long range. Thus D_E is one of the key parameters to be fitted, and, as will be shown, it has a direct effect on the speed of the EMT wave. For the boundary condition, we have experimentally that cells on the periphery of the micropatterns have a reduced inhibitory E-CAD effect and are thus more sensitive to WNT3A ligand (see Main Text and especially Figure 2 and Supplemental Figure 2). We incorporate this observation by setting $E(R,t) = 0$.

To model the interaction between the WNT response, DKK1, and E-CAD, simple Michaelis–Menten dynamics with activation and inhibition between the three species as shown in Figure 7A suffice. Mechanistically, we justify these interactions as follows: the inhibition of WNT by DKK1 is at the receptor level and is well known[3]; the activation of DKK1 by WNT is at the transcription level and was shown in Figure 4; the inhibition of E-CAD by WNT is also at the transcription level, though it operates more indirectly by WNT first turning on SNAIL and working with FGF[4] (which is always present and constant in our media); and there is extensive literature on the interaction of E-CAD with β-catenin and the effect this has on WNT signalling[5]. For this last interaction, we choose to model it as $+W \rightarrow E$, i.e. akin to simple enzymatic degradation instead of a more complicated sequestration/release mechanism that might be modelled as $E + W \rightleftharpoons C, C \rightarrow \emptyset$. We make this choice because although there is some evidence for this latter picture[6], much of the dynamic details of how E-CAD affects WNT signalling remain to be worked out. Thus in lieu of a more detailed mechanism, we use simple enzymatic degradation as a reasonable phenomenological approximation of the system, and we find that we achieve a better, more robust fit with it than with the sequestration/release model, even though the latter has more variables.

Since the scales on the three dynamical variables depend on imaging conditions and are thus arbitrary, we can adsorb certain constants into their definitions without affecting the generality of the model. We set the maximum rate of synthesis of E-CAD to be equal to ν_E, the rate of natural E-CAD decay, so that in pluripotency the E-CAD level in each cell is 1. Likewise, we set the maximum rate of the WNT response to be equal to its degradation rate ν_W so that the WNT response varies from 0 to 1. We also assume, based on our evidence of direct induction of DKK1 by WNT (Figure 4) that this WNT response rate is a good approximation for the rate of DKK1 synthesis. The coefficient of W in equation (2) can be chosen to equal the degradation rate of W in (1) by adjusting the scale of I so we do not require a DKK1 specific synthesis rate. We do though let DKK1 have its own degradation rate ν_I.

Combining all of the above we obtain:

Development • Supplementary information

Note that if we are purely interested in exploring the possible dynamics we could simplify this system further, rescaling the time for example so that $t = \tau * t_0$ with $t_0 = 1/\nu_W$. However, as we wish to use this model to fit our data, we need a match of the timescales between model and experiment, and hence we need to fit ν_W. Fortunately, we can get help in estimating its value since in the E-CAD$^{-/-}$DKK1$^{-/-}$ cell line the PDE system reduces to the one parameter equation:

A fit of the qPCR measured LEF1 response in small, unpatterned colonies of E-CAD$^{-/-}$DKK1$^{-/-}$ cells at various times results in a value of (Figure S8). The upper and lower 95% confidence bounds are 0.07 and r. Since this estimate is based on mRNA data and so represents an upper limit, we restrict our search of possible values to be between and $0.24/hr$. We find that the final best fit value is r, which means that would reaches its half-maximal value ~6 hours after stimulation if the inhibition of E-CAD and DKK1 are not included.

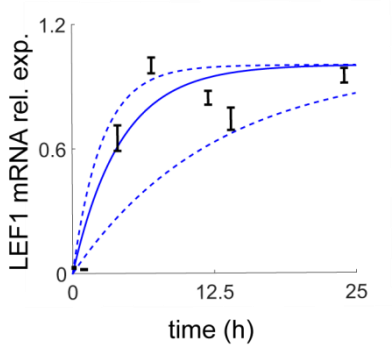

Figure S8: Solid line indicates best fit of LEF1 qPCR timecourse in unpatterned E-CAD$^{-/-}$DKK1$^{-/-}$ cells to Equation 4. Dashed lines indicate 95% confidence interval in the fit. $\nu_W = 0.24\ (0.07, 0.40)$. Error bars represent the standard deviation of three biological replicates.

2.1 Fitting DKK1 and WNT interaction with E-CAD$^{-/-}$ cell line

In the E-CAD$^{-/-}$ cell line the system reduces to just equations (1) and (2) with 0. This leaves just 4 parameters to be fitted: and ν_I. This parameter space is small enough that we can perform a simple exhaustive grid search to find the global optima where the model WNT response curve at 12 and 48hrs matches the data at 12 hours (measured by LEF1) and 48 hours (measured by BRA or SOX17 in Figure 6, which is also equivalent to 1-SOX2) as calculated by a least squares fit. Where possible, this grid search was centered on biologically relevant values for variables, or from previous similar simulations[1].

Figure S9 shows the best fit to the data. The Hill parameter n can adjust the slope of the curve, but the effects of the other parameters are less obvious. To understand these effects we do two things: (1) we

Development • Supplementary information

perturb each parameter individually and see the change to the fit, and (2), we let the remaining parameters adapt to the perturbed parameter to see if and how the perturbation can be corrected. Doing this we can see for example that doubling D_I means that more cells on the boundary respond to WNT. Allowing the other parameters to vary while holding the doubled D_I constant, we can also see that decreasing ν_I can counteract this perturbation. This makes sense as increased D_I means more inhibitor is lost and decreasing ν_I counteracts this by making the inhibitor degrade less. The opposite is also true, since halving D_I means fewer cells on the boundary respond to WNT and this effect can be counteracted by increasing ν_I. For the WNT response threshold θ_w, we find that doubling it leads to less inhibitor and more differentiation, and that this can be counteracted by lowering the DKK1 degradation rate. Halving θ_w can conversely be counteracted by increasing ν_I. Taken together, these results imply that there is some redundancy between certain parameters in our model. This is not surprising as although we formulated our model to be minimal in the number of parameters, we also based it directly on the known biology and variables that could be easily perturbed. A more abstract model with a reduced number of variables might give more independent parameter estimates, but it would be harder to explore and relate to the fundamental biology at hand.

Perturbing the E-CAD$^{-/-}$ fit

	D_I (mm^2h^{-1})	ν_I (h^{-1})	θ_W
(1)	0.0024	0.0017	0.3000
(2)	0.0046	0.0017	0.3000
(3)	0.0046	0.0009	0.2073
(4)	0.0012	0.0017	0.3000
(5)	0.0012	0.0034	0.3628
(6)	0.0024	0.0850	0.3000
(7)	0.0022	0.0850	0.1893
(8)	0.0024	0	0.3000
(9)	0.0025	0	0.3045
(10)	0.0024	0.0017	0.5442
(11)	0.0013	0.0017	0.5442
(12)	0.0024	0.0017	0.1361
(13)	0.0050	0.0066	0.1361

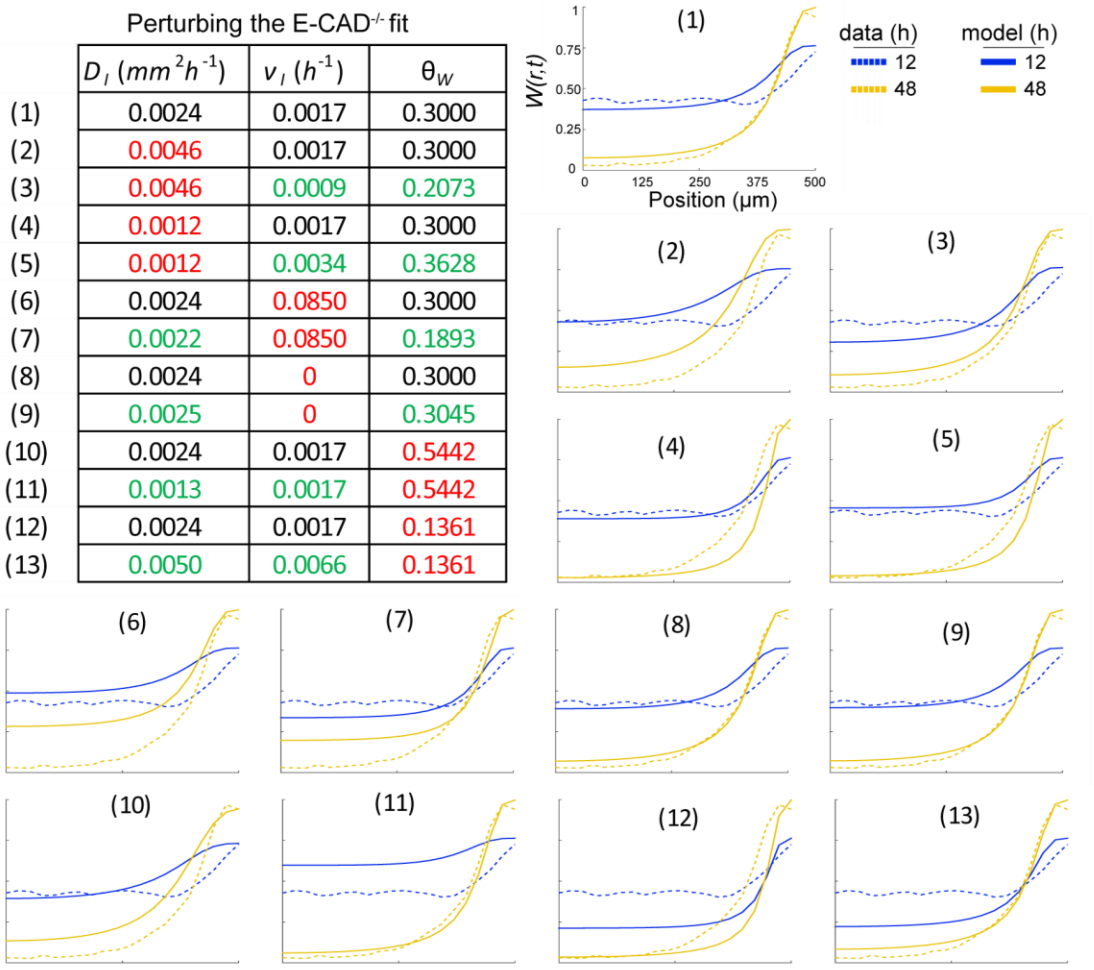

Development • Supplementary information

Figure M2: Fit of DKK1 specific parameters with E-CAD$^{-/-}$ cell line, and parameter analysis using specific perturbations. Values in black in the table are the best fit parameters, values in red are the parameters specifically perturbed, and values in green are the new best fit parameters based on the perturbed parameter.

2.2 Fitting E-CAD and WNT interaction with DKK1$^{-/-}$ cell line

In the DKK1$^{-/-}$ cell line the system reduces to just equations (1) and (3), with $I(r,\tau)=0$. As can be seen when solving for $W(r,\tau)$ in equilibrium (see Equation 5), this system undergoes a super-critical pitchfork or "cusp" bifurcation to two different WNT states (Figure S9) depending on the choice of just 3 parameters: m, θ_E, and k.

$$\frac{1}{W}=\frac{k}{v_W}*\frac{\theta_E^m}{\theta_E^m+W^m}+1 \qquad (5)$$

More interestingly, it can be shown that, depending on initial conditions or boundary conditions, this system can admit traveling wave solutions that switch from the higher equilibrium state to the lower equilibrium state[7,8]. In 1D these waves travel with a unique shape and have a speed largely dependent on the coupling constant (here D_E) and time scale of E-CAD synthesis and degradation (v_E). Since in our case we have the boundary condition $E(R,t)=0$, then we can have the situation whereby WNT stimulation directs the periphery cells to a WNT "high" equilibrium state that is more stable than the WNT "low" equilibrium state that their more central neighbours are in. This creates an unstable boundary that can only be resolved by a travelling wave solution. By adjusting $m, \theta_E, k, v_E$and D_E ,we can moderate the speed and shape of the wave to fit the profile of WNT responsive cells in the DKK1$^{-/-}$ micropatterns at 12 hours (LEF1) and 48 hours (BRA and SOX17, as measured in Figure 6). As for the previous fit, this parameter space is sufficiently small enough that we can perform a grid search to find the global optima.

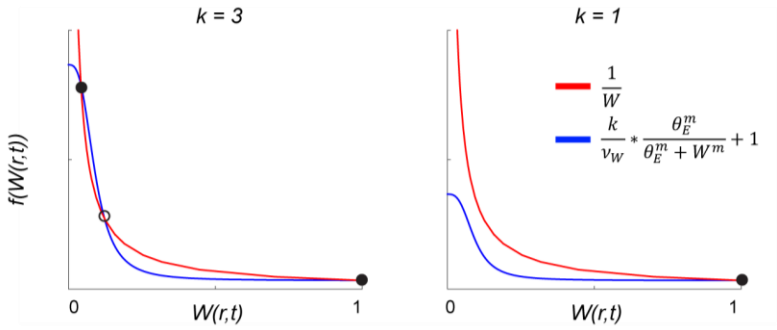

Figure S10: Examples of the cusp bifurcation in Equation 5 with different values of *k*. Solid circles mark stable points, open circles mark unstable points.

The best fit is shown in Figure S11. As for the DKK1 fit, the Hill parameter m can adjust the slope of the curve ($m=3$ in our fit), and to learn the effect of the other parameters we again use selected perturbations. As one might expect, increasing the coupling constant D_E increases the speed of the WNT response wave while decreasing it slows it down. This parameter has the largest effect on wave speed, though changing v_E , the effective turnover rate of E-CAD, also can modify speed since increasing it makes cells next in line in the wave respond faster once the wave reaches them. This can be noted in the perturbation analysis, as changing either D_E or v_E leads to a change in the other

variable to compensate for it. As one expects from Equation 5, θ_E and k are linked, so perturbing one leads to a correction from the other. Due to the non-linearity of the bifurcation they control they are also quite sensitive to perturbation, so just halving or doubling one leads to a collapse of the wave and one dominant state (i.e. either E-CAD is too strong and cells resist the WNT signal, or E-CAD is too weak and even a small WNT signal can downregulate it anywhere).

Perturbing the DKK1$^{-/-}$ fit

	D_E ($mm^2 h^{-1}$)	v_E (h^{-1})	θ_E	k
(1)	0.0043	8.0402	0.09005	2.4184
(2)	0.0086	8.0402	0.09005	2.4184
(3)	0.0086	30.0788	0.0272	9.0474
(4)	0.0021	8.0402	0.09005	2.4184
(5)	0.0021	67.0019	0.0367	6.0619
(6)	0.0043	8	0.09005	2.4184
(7)	0.0058	8	0.0272	9.0474
(8)	0.0043	4	0.09005	2.4184
(9)	0.0058	4	0.1650	1.2217
(10)	0.0043	8.0402	0.1801	20.1534
(11)	0.0332	6.0619	0.1801	1.2217
(12)	0.0043	8.0402	0.0450	20.1534
(13)	0.0045	0.0149	0.0450	6.0619
(14)	0.0043	8.0402	0.09005	4.8368
(15)	0.0548	100	0.0496	4.8368
(16)	0.0043	8.0402	0.09005	1.2092
(17)	0.0905	100	0.1650	1.2092

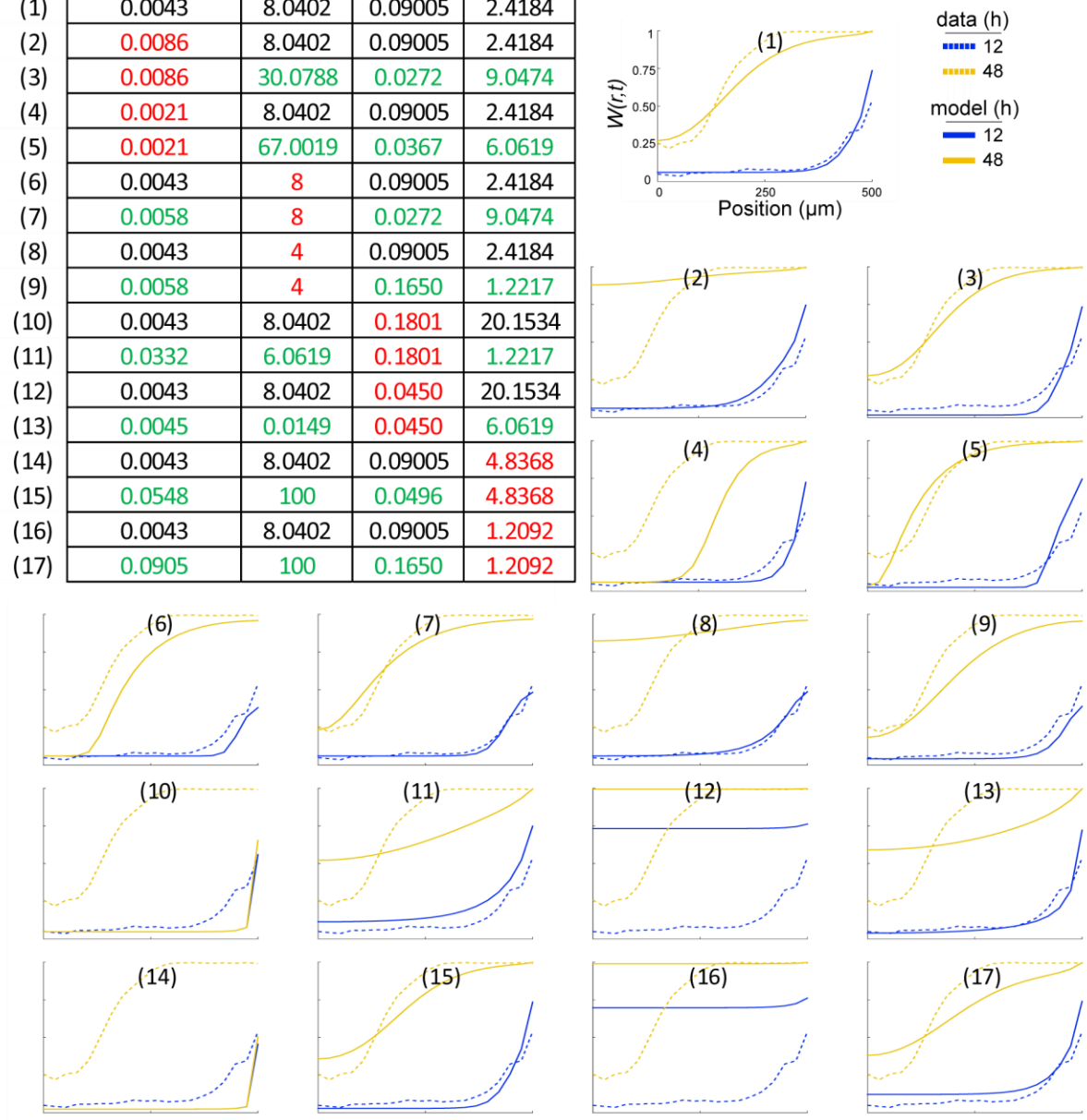

Figure S11: Fit of E-CAD specific parameters with DKK1$^{-/-}$ cell line, and parameter analysis using specific perturbations. Values in black in the table are the best fit parameters, values in red are the parameters specifically perturbed, and values in green are the new best fit parameters based on the perturbed parameter.

2.3 Applying fit to GLR:DKK1$^{-/-}$ time-lapse movie

As discussed in the main text, a further test of our fitted model was to apply it to our live-cell time-lapse GLR:DKK1$^{-/-}$ data. We found that though the model matches the data for the first 30 hours, beyond this there is a collapse of the inner SOX2 region that is quicker than what the model predicts (Figure S12). The agreement is a little better in a repeat of the experiment (Figure S12) but there is still a greater error between the model and these live cell data sets than the fixed antibody stained data we fit to. However the virtual disappearance of the SOX2 domain in the colony center at 72hrs is confirmed by the fixed data in Figure 6, which was not used in the fit. The difficulties in reproducing the movie data could entail the different dynamics of the live fluorescent reporter versus the LEF1 and the SOX2 stain, phototoxicity, or uncontrollable density differences.

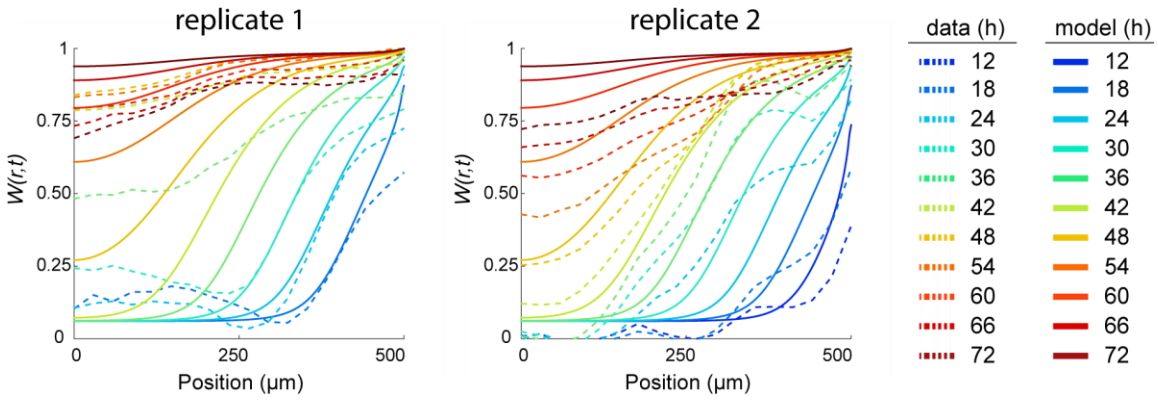

Figure S12: Comparison of the previously fitted model to two replicates of continuously imaged GLR:DKK1$^{-/-}$ micropatterns, the first replicate is an average of 7 colonies, the second replicate is an average of 10 colonies.

3 Mesoderm versus endoderm fate bifurcation

Having obtained the radial profile of differentiated cells from Eqs 1-3 for each cell line, the next question is whether these cells will commit to mesoderm (BRA) or endoderm (SOX17). In the anterior mouse primitive streak, these are two mutually exclusive states that are influenced mainly by the relative levels of WNT versus NODAL signalling, with more WNT signalling leading to mesoderm and more NODAL signalling leading to endoderm. The effect of NODAL signalling on endoderm fate choice was also shown in hESC micropatterns[9] in and reproduced in Fig 1A. Here we do not attempt to model the mechanism for this bistability or capture the dynamics. Instead, we simply let the choice depend on the ratio of WNT to NODAL signalling, letting the differentiated cells go to endoderm with probability $P(r)$ and going to mesoderm with probability $Q(r) = 1 - P(r)$. Since we are focused only on the fraction of cells at each radial position that differentiated, and in our model a differentiated cell is a cell that responded to the WNT signal, we assume that the WNT level is approximately the same across differentiated cells and thus a constant. NODAL signalling however is not the same for all cells, so we use measured nuclear SMAD2 levels for each cell line to approximate it (Figure 5 and Figure S13). Note

Development • Supplementary information

that we examine the SMAD2 levels at 24hrs rather than 48hrs, as 48hrs is too late and the fate decision has already been made. Thus our probabilities are

$$P(r) = \frac{NODAL(r)}{WNT(r) + NODAL(r)} = \frac{SMAD2_i(r) - b_1}{b_2 + (SMAD2_i(r) - b_1)} \quad (6)$$

$$Q(r) = \frac{WNT(r)}{WNT(r) + NODAL(r)} = 1 - P(r) \quad (7)$$

This effectively amounts to just a rescaled version of the measured SMAD2 profiles for each of our cell lines.

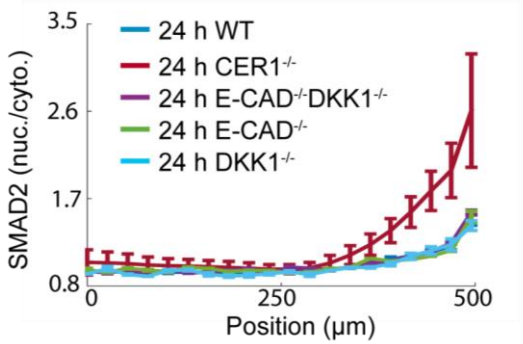

Figure S13: Radial profiles of nuclear SMAD2 in the cell lines modelled, n=20 colonies per condition.

4 Comparison of full model with data

Putting together the PDE system and the fate bifurcation parts of the model and comparing it to the measured SOX2, BRA, and SOX17 radial profiles at 48hrs for each cell line, we see that our model captures the data very well (Figure 7E). One obvious missing feature, however, is the dual SOX17 and BRA positive cell population. These are cells that express both markers and have not yet committed to one fate versus the other (though we expect they will as time progresses) and are found in most significant numbers in the DKK1$^{-/-}$ and E-CAD$^{-/-}$DKK1$^{-/-}$ cell lines. If forced to apportion this population to either mesoderm or endoderm, one can see that classifying them as mesoderm would give the better fit to the model. Interestingly the major exception to this is at the colony edges in the double knockout E-CAD$^{-/-}$DKK1$^{-/-}$ cell line, where doing so would lead the model to underestimate the number of BRA cells counted in the imaging. To further investigate this large discrepancy between the model and the data, we re-examined our E-CAD$^{-/-}$DKK1$^{-/-}$ micropattern data. We found that on the colony edge (and only on the colony edge) BRA cells sometimes lumped together in discrete clusters (Figure S14). As these clusters were immediately surrounded by a monolayer primarily composed of SOX17 cells, instead of the salt-and-pepper BRA or SOX17 pattern found further in the interior of the colony, we suppose that these clusters formed due to cell movement, i.e. cells were initially patterned in a stochastic manner but the BRA cells then moved and coalesced together while the SOX17 cells either stayed in place or underwent unbiased migration. That this only takes place on the edge of the E-CAD$^{-/-}$DKK1$^{-/-}$ micropatterns could be explained by noting that it is in this regime that cells are the least restricted from

Development • Supplementary information

moving, both by E-CAD and by existence of neighbours. The clusters are often quite 3 dimensional, and since our analysis involves just 2D segmentation on epifluorescence images, classification of cells in these clusters may be biased and introduce errors such as overcounting the number of SOX17/BRA cells. Migration was also not included in the model, and introducing a biased outward migration term for BRA cells for example might lead to an improved (though more complex) fit.

Overall, our model faithfully captures the E-CAD and DKK1 patterning dynamics as observed in our micropatterns and live-reporter lines, and in the most striking case where it does not, it still proves informative, pointing to a segregation and clustering of mesoderm versus endoderm cells that may be due to cell migration and merits further investigation.

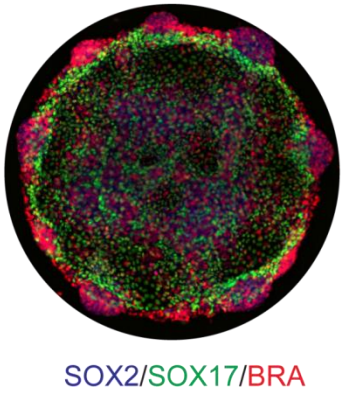

Figure S14: Example of an E-CAD$^{-/-}$DKK1$^{-/-}$ micropattern with BRA clusters on the periphery. The center remains a salt-and-pepper mix of SOX17 and BRA cells.

1. Etoc, F. *et al.* A Balance between Secreted Inhibitors and Edge Sensing Controls Gastruloid Self-Organization. *Dev. Cell* **39,** 302–315 (2016).

2. Libusova, L., Stemmler, M. P., Hierholzer, A., Schwarz, H. & Kemler, R. N-cadherin can structurally substitute for E-cadherin during intestinal development but leads to polyp formation. *Development* **137,** 2297–2305 (2010).

3. Cruciat, C. M. & Niehrs, C. Secreted and Transmembrane Wnt Inhibitors and Activators. *Cold Spring Harb. Perspect. Biol.* **5,** 39–64 (2013).

4. Arnold, S. J. & Robertson, E. J. Making a commitment: cell lineage allocation and axis patterning in the early mouse embryo. *Nat. Rev. Mol. Cell Biol.* **10,** 91–103 (2009).

5. Fagotto, F. Looking beyond the Wnt pathway for the deep nature of β-catenin. *EMBO Rep.* **14,** 422–33 (2013).

6. Kam, Y. & Quaranta, V. Cadherin-bound β-catenin feeds into the Wnt pathway upon adherens junctions dissociation: Evidence for an intersection between β-catenin pools. *PLoS One* **4,** (2009).

7. Fisher, R. A. The Wave of Advance of Advantageous Genes. *Ann. Eugen.* **7,** 355–369 (1937).

8. Tikhomirov, V. M. in *Selected Works of A. N. Kolmogorov: Volume I: Mathematics and Mechanics* (ed. Tikhomirov, V. M.) 242–270 (Springer Netherlands, 1991). doi:10.1007/978-94-011-3030-

Development • Supplementary information

1_38

9. Martyn, I., Kanno, T. Y., Ruzo, A., Siggia, E. D. & Brivanlou, A. H. Self-organization of a human organizer by combined Wnt and Nodal signalling. *Nature* **558,** 132–135 (2018).

Development • Supplementary information

Supplemental Tables

Table S1: Antibody information

Antigen	Antibody	Dilution
Active β-CATENIN	Millipore 05-665	1:400
BRACHYURY	R&D Systems AF-2085	1:300
E-CADHERIN	Cell Signalling 3195	1:200
E-CADHERIN	Abcam 40772	1:400
FRZD7	R&D Systems MAB1981	1:200
LEF1	Cell Signalling 2230	1:200
LRP6	R&D Systems 1505	1:100
N-CADHERIN	BioLegend 350802	1:200
SMAD2	BD bioscience 610842	1:100
SOX17	R&D Systems AF-1924	1:200
SOX2	Cell Signalling 3579	1:200

Table S2: RT-QPCR Primer designs

Gene Symbol	Forward primer	Reverse Primer
AXIN2	ctccccaccttgaatgaaga	tggctggtgcaaagacatag
BRACHYURY	catgcaggtgagttgtcagaa	gctgtgacaggtacccaacc
CER1	gccatgaagtacattgggaga	cacagccttcgtgggttatag
DKK1	ccttggatgggtattccaga	cctgaggcacagtctgatga
DKK3	agagcctgatggagccttg	ggcttgcacacatacaccag
LEF1	agatcaccccacctcttgg	atgagggatgccagttgtgt
LEFTY1	ctgcacaccctggacctt	atcccctgcaggtcaatgta
LEFTY2	cctggacctcagggactatg	atcccctgcaggtcaatgta
SFRP1	gctggagcacgagaccat	tggcagttcttgttgagca
SFRP2	gctagcagcgaccacctc	tttttgcaggcttcacatacc

Development • Supplementary information

Table S3: sgRNA designs

Gene Symbol	Forward primer	Reverse Primer
CER1	caccgcttcctcatggttgcctgt	aaacacaggcaaccatgaggaagc
DKK1	caccgtctggtacttattcccgcc	aaacggcgggaataagtaccagac
DKK3	caccgtctcattgtgatagctggg	aaaccccagctatcacaatgagac
E-CAD	caccgcagcagcagcagcgccgag	aaacctcggcgctgctgctgctgc
LEFTY1	caccggtcatccccacccacgtga	aaactcacgtgggtggggatgacc
SFRP1	caccggagcacgagaccatggcgg	aaacccgccatggtctcgtgctcc
SFRP2	caccggtggtcgctgctagcgagg	aaaccctcgctagcagcgaccacc

Table S4: Knockout lines

Target	Separate clones
RUES2:DKK1$^{-/-}$	3
RUES2-GLR:DKK1$^{-/-}$	2
RUES2:DKK3$^{-/-}$	2
RUES2:E-CAD$^{-/-}$	2
RUES2:CER1$^{-/-}$	1
RUES2:LEFTY1$^{-/-}$	1
RUES2:SFRP1$^{-/-}$	1
RUES2:SFRP2$^{-/-}$	1
RUES2:SFRP1$^{-/-}$SFRP2$^{-/-}$	1
RUES2:LEFTY1$^{-/-}$CER1$^{-/-}$	1

Development • Supplementary information

Supplemental Figures

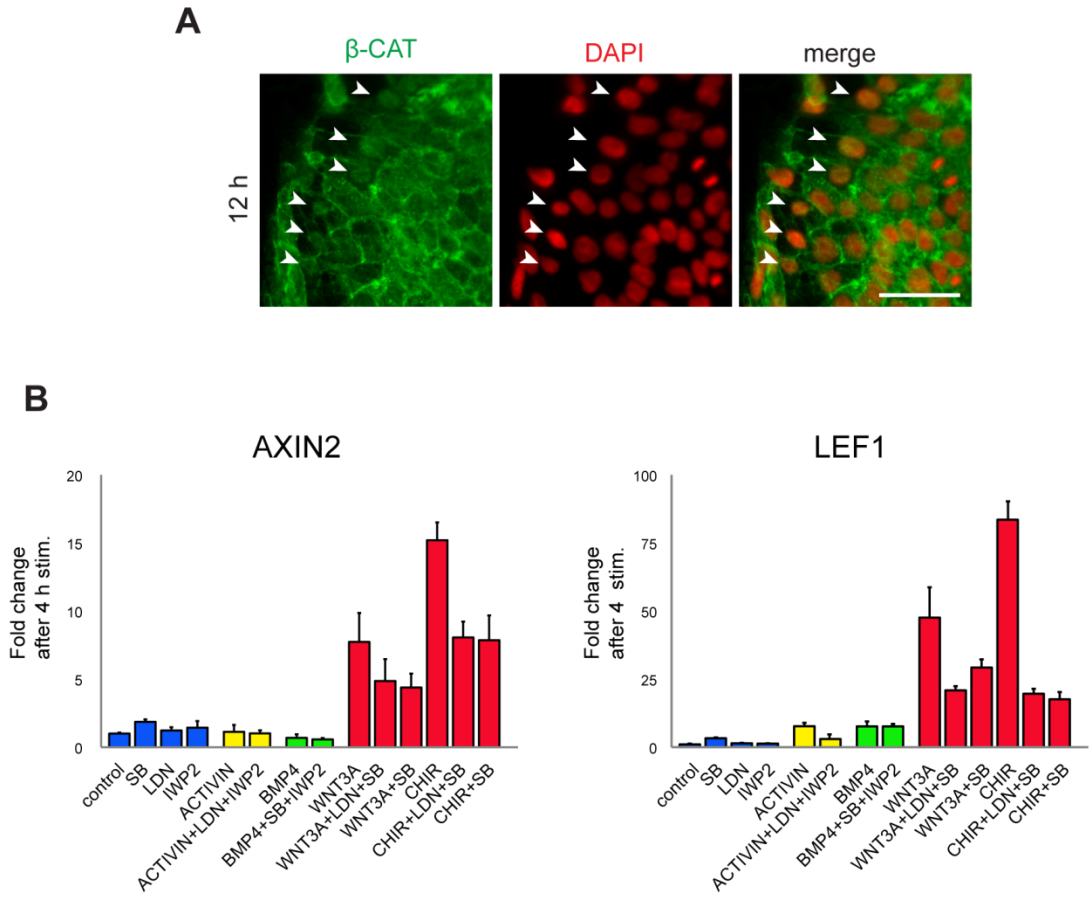

Figure S1 | WNT3A response markers

(A) Inset of an abnormally low density micropattern colony stimulated with WNT3A and fixed and stained at 12h for active β-CATENIN. Even at this low density (seeded with $6x10^5$ cells, stimulated 2 hours after seeding) an increase in β-CAT in the nucleus is only visible in loosely connected cells on the colony edge (arrows). Nuclear β-CATENIN in cells away from the periphery or at higher density (including standard low density conditions) is not easily observed, largely due to signal from membrane-bound or cytoplasmic regions. Scale bar, 50µm.

(B) qPCR of AXIN2 and LEF1 as a function of inputs arrayed on x-axis. The results show that the LEF1 and AXIN2 response is dominated by WNT3A, though synergism with the NODAL pathway is significant as well, as can be seen by comparing WNT3A or CHIR with WNT3A+SB or CHIR+SB. Thus LEF1 and AXIN2 can be used as proxies for early WNT3A response. Also note that LEF1 gives a greater positive signal than AXIN2, reaching 84-fold induction compared with 15 fold induction for CHIR condition.

Development • Supplementary information

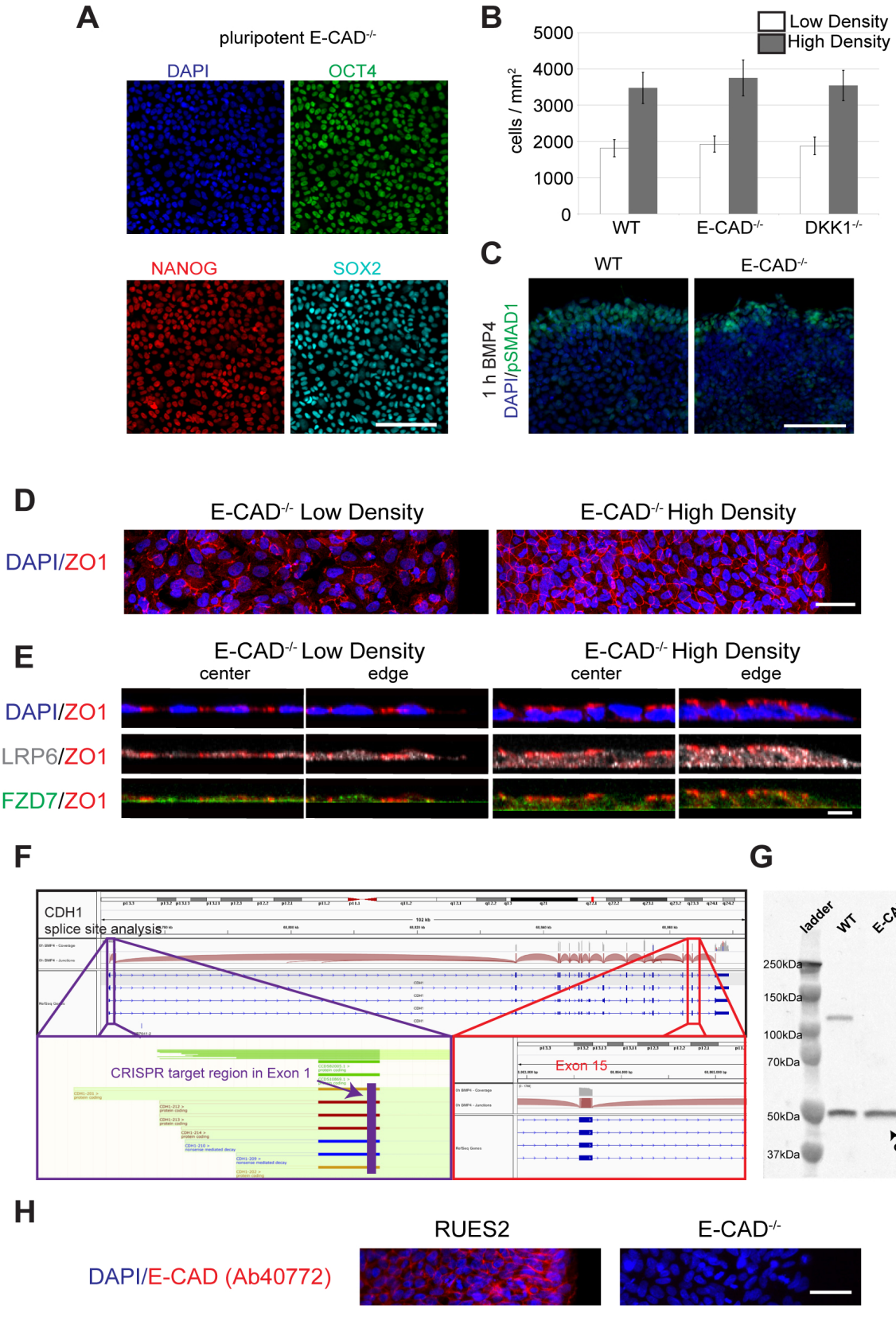

Development • Supplementary information

Figure S2 | Epithelial integrity is preserved in E-CAD$^{-/-}$ cells.

(A) E-CAD$^{-/-}$ cells maintain pluripotency markers even with continual passaging (i.e. >20 passages). Images are of unpatterned, standard hESC culture colonies. Scale bar, 100µm.

(B) E-CAD$^{-/-}$ cell seeding efficiency and growth is similar to wild type and DKK1-/- cell lines.

(C) Test of epithelial integrity and BMP4 response. Edge of high density wild type and E-CAD$^{-/-}$ micropatterns stimulated with BMP4 and fixed and stained for pSmad1 after 1h. As in the wild type, pSMAD1 expression is restricted to the periphery in E-CAD$^{-/-}$ colonies. Scale bar, 100µm.

(D) Maximum intensity projection of ZO1 and DAPI in low density and high density E-CAD$^{-/-}$ micropatterns immediately prior to stimulation. The network of tight junctions is the same as in the wild type (Figure 1C). Scale bar, 50µm.

(E) Cross-sections showing the apical-basal position of WNT receptors relative to DAPI and ZO1. Result is the same as for wild type micropaterns (Figure 1D). Scale bar, 10µm.

(F) Top: sashimi plot in Integrative Genomics Viewer of E-CAD region from previously published RNA-seq data set[1] showing exon splicing pattern observed in RUES2 cells in pluripotency conditions. Bottom left: zoom of Exon 1 region in Ensembl viewer showing the four different E-CAD isoforms and the sgRNA CRISPR targeting site used. Bottom right: zoom of Exon 15 region that the Cell Signalling 3195 E-CAD antibody targets. As one can see from the plot, there is no isoform that skips this exon.

(G) Western blot of pluripotent wild type and E-CAD$^{-/-}$ cells for E-CAD and α-tubulin. One can see that while E-CAD and α-tubulin are detected in the wild type cells, only α-tubulin is visible in the knockout cell line.

(H) Staining of pluripotent wild type and E-CAD$^{-/-}$ cells with Abcam anti-E-CADHERIN ab40772 antibody that targets amino acids 600-700. One can see that while E-CAD is detected in the wild type cells, no E-CAD is visible in the knockout cell line. Scale bar, 50µm.

Development • Supplementary information

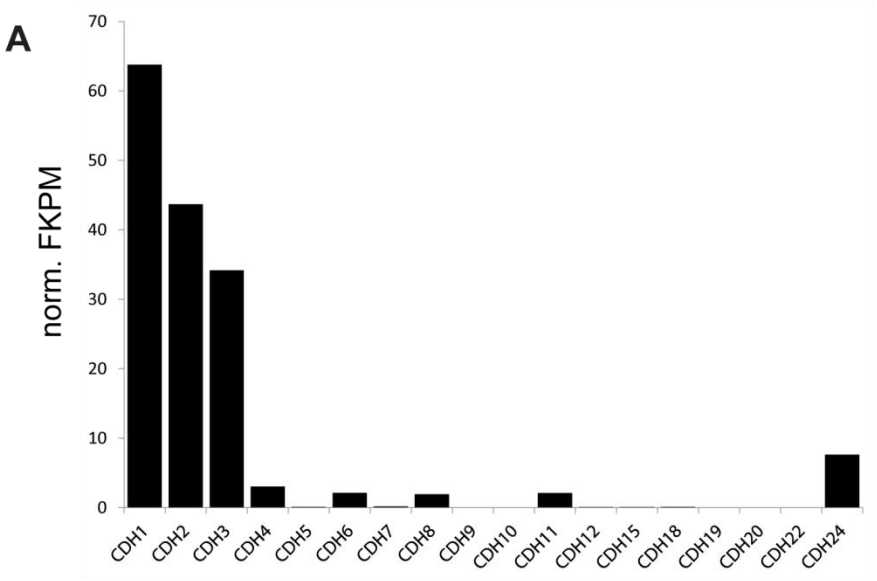

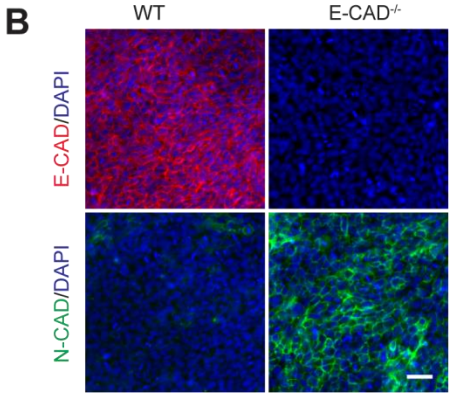

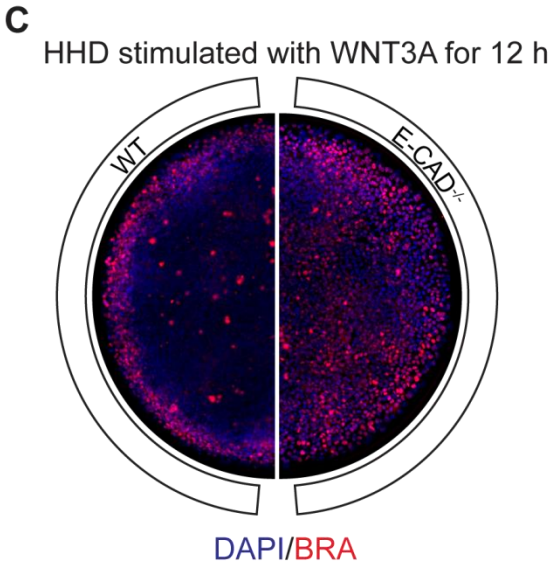

Development • Supplementary information

Figure S3 | A change in the protein expression profile of N-CADHERIN occurs in the E-CAD$^{-/-}$ cell line.

(A) RNA-seq profiling for all classic cadherins in pluripotent hESCs. Since the E-CAD (CDH1) knockout is lethal in mouse at the post-compaction stage, we were somewhat surprised at the lack of an E-CAD$^{-/-}$ pluripotent phenotype (Supplemental Figure 2). However both N-CADHERIN and P-CADHERIN (CDH2,CDH3) are substantially expressed at the mRNA level in hESCs in pluripotency.

(B) Stain for N-CAD and E-CAD in wild type and E-CAD$^{-/-}$ in unpatterned pluripotent colonies. Antibody stain for E-CAD confirms that gene is knocked out in E-CAD$^{-/-}$ cells. More interestingly, while N-CAD is barely visible in wild-type cells, N-CAD is highly expressed and membrane localized in E-CAD$^{-/-}$ cells. Thus there is a reservoir of N-CAD message in hESC that is only expressed in the absence of E-CAD, which may be a consequence of the same pathway that up regulates N-CAD during EMT when the transcription of E-CAD is abrogated by SNAIL. Interestingly, other research has shown that the artificial replacement E-CAD protein by N-CAD protein in the mouse intestine after gastrulation showed that N-CAD could fulfill the structural role of E-CAD, but the replacement lead to an up-regulation of WNT signalling that is also consistent with our findings[2]. Scale bar, 50µm.

(C) 12h WNT3A response measured by BRA in high high density (HHD) wild type and E-CAD$^{-/-}$ micropatterns. HHD micropatterns are left to grow for an additional 36h beyond that of HD micropatterns before stimulating with WNT3A. One sees that even at this extreme the knockdown of E-CAD allows a WNT3A response into the center of the micropattern.

Development • Supplementary information

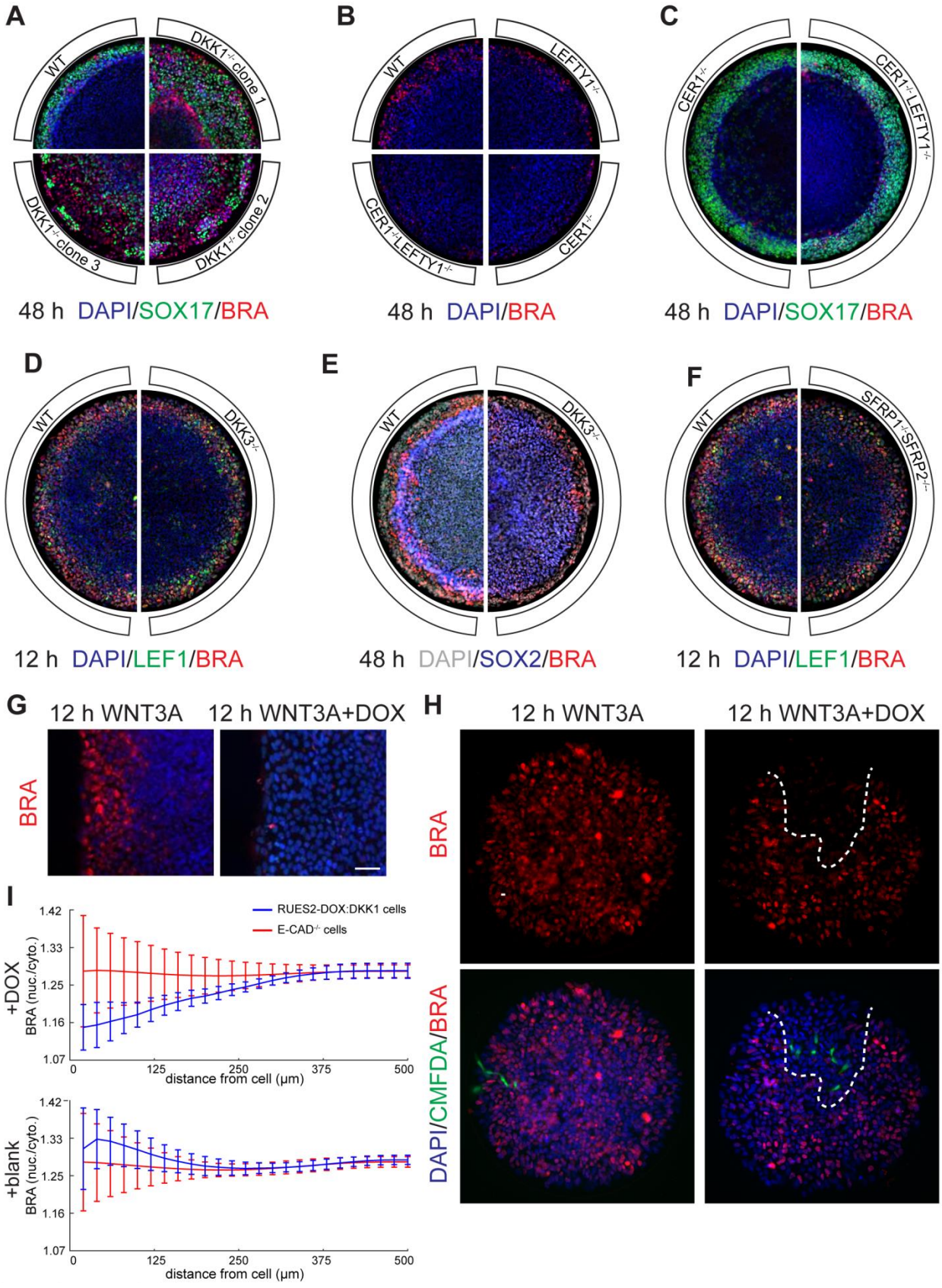

Development • Supplementary information

Figure S4 | Other inhibitor CRISPR knockout line and clones

(A) Other DKK1$^{-/-}$ clonal lines with different frameshift mutations also exhibit the same micropattern phenotype when stimulated with WNT3A at high density and fixed and stained after 48 hours.

(B) No discernible difference in SOX17 expression at 48h between CER1$^{-/-}$ and CER1$^{-/-}$LEFTY1$^{-/-}$ micropatterns under WNT3A stimulation.

(C) LEFTY1$^{-/-}$ micropatterns show no discernible difference with wild type micropatterns in number of BRA cells. However, both CER1$^{-/-}$ and CER1$^{-/-}$LEFTY1$^{-/-}$ (with a different CER1 frameshift mutation) show similar phenotype in having fewer BRA cells. Thus CER1$^{-/-}$ and not LEFTY1$^{-/-}$ is the main NODAL inhibitor during WNT induced patterning.

(D) and (E) No discernible difference at 12h or 48h between wild type and DKK3$^{-/-}$ micropatterns under WNT3A stimulation.

(F) No discernible difference at 12h between wild type and SFRP1$^{-/-}$SFRP2$^{-/-}$ micropatterns under WNT3A stimulation.

(G) Edge of a high density 1000µm diameter RUES2-DOX:DKK1-V5 micropattern. Cells were either given DOX or blank media for 12 h and then stimulated with WNT3A for a further 12 h (again with or without DOX continuing the pre-treatment). Cells were then stained for BRA. Scale bar, 50µm.

(H) 500µm diameter E-CAD$^{-/-}$ micropatterns seeded with 1% CMFDA cell tracker marked RUES2-DOX:DKK1-V5 cells (green). Cells were either given DOX or blank media for 12 h immediately after RI removal, and then stimulated with WNT3A for a further 12 h (again with or without DOX continuing the pre-treatment). Micropatterns were then fixed and stained for DAPI and BRA. In the DOX induced micropatterns one can see a BRA exclusion zone around the DKK1 expressing cells (marked roughly with dashed line).

(I) Quantification of (H). 5 DOX-induced and 5 blank stimulated micropatterns were segmented and all cells were first classified as either RUES2-DOX:DKK1-V5 (green) or E-CAD$^{-/-}$ cells. For each cell the nuclear to cytoplasmic ratio of BRA in all neighbouring cells within radius r (x-axis) was calculated and averaged. These averages were then averaged across all cells of their cell type (50 for RUES2-DOX:DKK1-V5, and 5000 for E-CAD$^{-/-}$) and plotted as shown with error bars indicating the standard deviation. One can see that in the DOX induced micropatterns the cells neighbouring the RUES2-DOX:DKK1-V5 cells show lower BRA than the average, and this effect is half-maximal at a distance of ~130µm, showing long-range action. This shielding does not happen when one looks at just neighbours of E-CAD$^{-/-}$cells, or in the blank stimulated micropatterns.

Development • Supplementary information

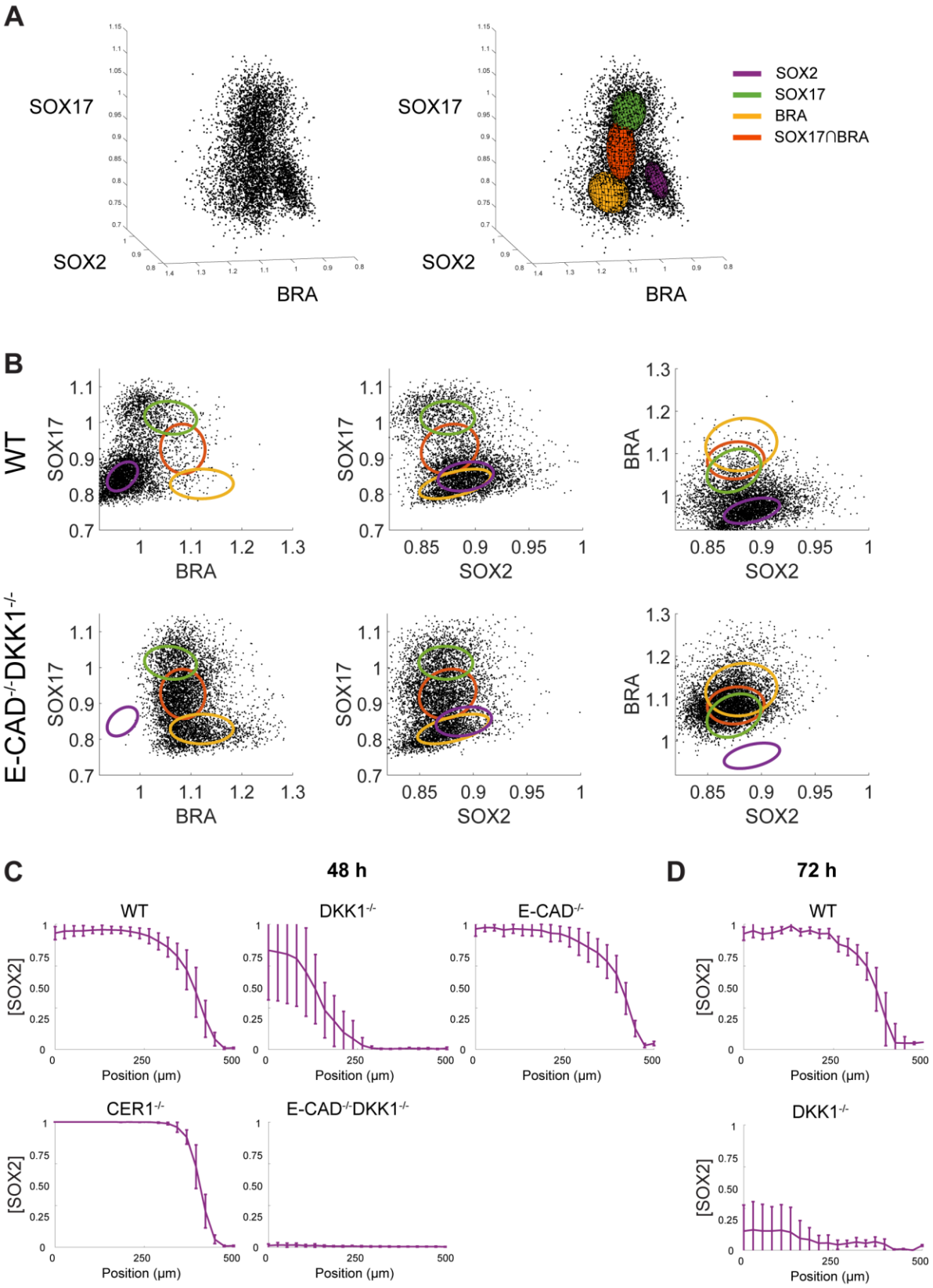

Development • Supplementary information

Figure S5 | Fate clustering and classification

(A) 3D scatterplots of combined cells from wild type, DKK1$^{-/-}$, E-CAD$^{-/-}$, E-CAD$^{-/-}$DKK1$^{-/-}$, and CER1$^{-/-}$ 48 h micropatterns data showing clustering into the Gaussian mixture model used for Figure 5D.

(B) Example scatterplots of cells from wild type and E-CAD$^{-/-}$DKK1$^{-/-}$ micropatterns projected into 2D for better visualization of the clustering.

(C) Proportion of cells classified as SOX2+ at 48 h plotted as a function of colony radius. Error bars represent the standard deviation of *n=20* colonies.

(D) Proportion of cells from micropatterns in Figure 6A classified as SOX2+ at 72 h plotted as a function of radius. Error bars represent the standard deviation of *n=20* colonies.

Development • Supplementary information

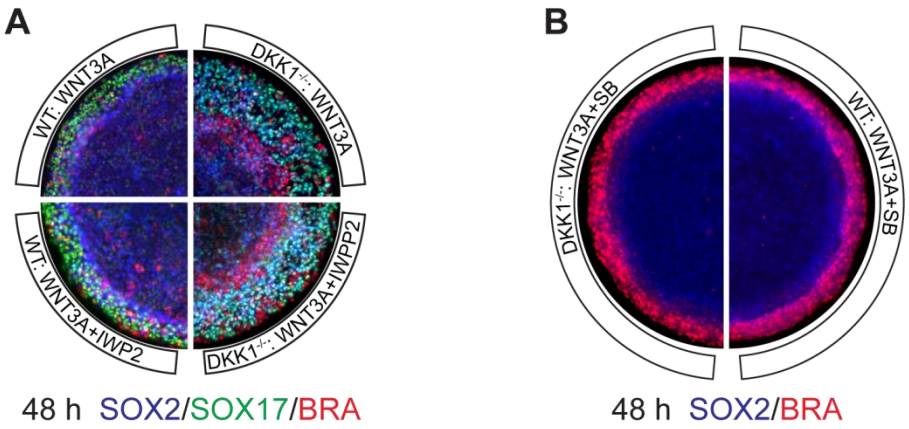

Figure S6 | Endogenous WNT signalling has little effect on patterning

(A) Wild type and DKK1$^{-/-}$ high density micropatterns stimulated with either WNT3A or WNT3A+IWP2 for 48h and stained for BRA, SOX2, and SOX17. No significant differences between wild type IWP2 and non-IWP2 or DKK1$^{-/-}$ IWP2 and non-IWP2 stimulated colonies were observed.

(B) Wild type and DKK1$^{-/-}$ high density micropatterns stimulated with WNT3A+SB for 48h and stained for BRA and SOX2.

Development • Supplementary information

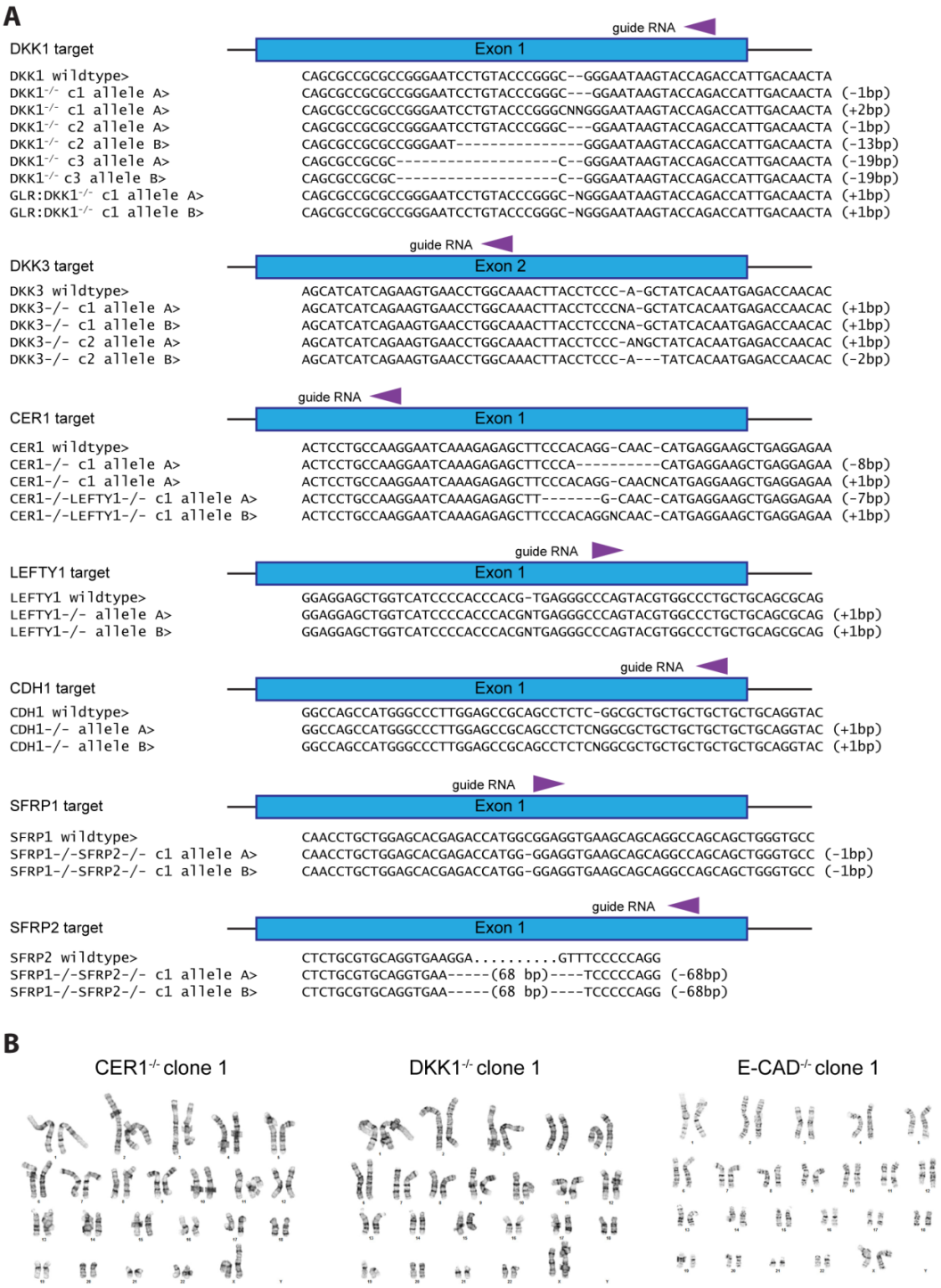

Figure S7 | Confirmation of CRISPR knockouts

(A) Sequences of the mutated alleles in the CRISPR/Cas9 knockout cell lines.

(B) The E-CAD$^{-/-}$ clone 1, DKK1$^{-/-}$ clone 1, and CER1$^{-/-}$ clone 1 cell lines were karyotypically normal.

Development • Supplementary information

Supplementary Materials and Methods: Modelling

1 Overview

In this supplement we present a minimal model that fits the micropattern WNT3A phenotype data for each CRISPR knockout cell line. The four key features of this data that the model captures are:

1. The geometric edge bias mediated by E-CAD.
2. The edge restriction of the WNT response by the secreted inhibitor DKK1.
3. The edge-to-interior EMT and WNT response wave, as especially observed in the DKK1$^{-/-}$ line.
4. The bifucation of WNT differentiated cells to mesoderm versus endoderm depending on the relative levels of NODAL signal received.

To capture the first three features we need a model with two spatial diffusion terms: (1) to describe the spreading of DKK1 and its loss from the colony edge, and (2) to describe the implicit cell-cell communication via E-CAD that is responsible for the EMT wave as explained in the main text. As will be shown, this part of the model will give us the WNT signal received by cells at a given radius at a given time and can be used to determine the proportion of differentiated cells at 48hrs after stimulation. As will also be shown, this part of the model consists of 10 parameters, 4 of which can be independently fitted to the E-CAD$^{-/-}$ phenotype, 5 of which can be fitted independently to the DKK1$^{-/-}$ phenotype, and 1 which can be estimated from the E-CAD$^{-/-}$DKK1$^{-/-}$ cell line.

To capture the last feature (the bifurcation of differentiated cells into either mesoderm or endoderm), ideally one would use detailed data of the gene regulatory networks for mesendoderm formation and mesoderm and endoderm bifurcation. However, these are not known to the required level of detail, and so we instead simply use the NODAL signalling level as defined by nuclear SMAD2 to determine fates, with cells with higher nuclear SMAD2 being more likely to be directed to endoderm rather than mesoderm.

2 PDE System

In the first part of the model we need to track three quantities: the WNT response, the level of DKK1, and the level of E-CAD. We let $W(r,t)$ represent the WNT response, we let $I(r,t)$ represent DKK1, and we let $E(r,t)$ represent E-CAD. $W(r,t)$ is the only quantity that we measure experimentally and that we use to fit the model (measured as nuclear LEF1 at 12hrs and at late times, the relative loss of SOX2 i.e., 1-SOX2 after rescaling). Since all of the relevant experiments were conducted on 1000μm diameter disc micropatterns, this 2D geometry is the only geometry we consider in our model as well (though it can be easily generalized to other geometries).

Initial conditions: We assume that $W(r,t)$and $I(r,t)$ are off everywhere and that $E(r,t)$ is uniformly on. For the boundary condition on $W(r,t)$, we take this variable to be cell intrinsic, thus there is no diffusion of $W(r,t)$.

Boundary conditions: For the boundary condition on $I(r,t)$, we assume that it behaves like the BMP secreted inhibitor NOGGIN in the modelling of Etoc et al[1]. Thus DKK1 can freely diffuse over the colony

Development • Supplementary information

and is quickly lost to the media on the edge, giving the boundary condition $I(R,t)=0$. Finally, for $E(r,t)$, since the E-CAD state of a cell also depends on its neighbours, we allow for a simple diffusion-like coupling with strength D_E. We do not initially know the scale of this dependence, whether it just immediate neighbours or if the coupling is long range. Thus D_E is one of the key parameters to be fitted, and, as will be shown, it has a direct effect on the speed of the EMT wave. For the boundary condition, we have experimentally that cells on the periphery of the micropatterns have a reduced inhibitory E-CAD effect and are thus more sensitive to WNT3A ligand (see Main Text and especially Figure 2 and Supplemental Figure 2). We incorporate this observation by setting $E(R,t)=0$.

To model the interaction between the WNT response, DKK1, and E-CAD, simple Michaelis–Menten dynamics with activation and inhibition between the three species as shown in Figure 7A suffice. Mechanistically, we justify these interactions as follows: the inhibition of WNT by DKK1 is at the receptor level and is well known[3]; the activation of DKK1 by WNT is at the transcription level and was shown in Figure 4; the inhibition of E-CAD by WNT is also at the transcription level, though it operates more indirectly by WNT first turning on SNAIL and working with FGF[4] (which is always present and constant in our media); and there is extensive literature on the interaction of E-CAD with β-catenin and the effect this has on WNT signalling[5]. For this last interaction, we choose to model it as $E+W\rightarrow E$, i.e. akin to simple enzymatic degradation instead of a more complicated sequestration/release mechanism that might be modelled as $E+W\rightleftharpoons C, C\rightarrow\emptyset$. We make this choice because although there is some evidence for this latter picture[6], much of the dynamic details of how E-CAD affects WNT signalling remain to be worked out. Thus in lieu of a more detailed mechanism, we use simple enzymatic degradation as a reasonable phenomenological approximation of the system, and we find that we achieve a better, more robust fit with it than with the sequestration/release model, even though the latter has more variables.

Since the scales on the three dynamical variables depend on imaging conditions and are thus arbitrary, we can absorb certain constants into their definitions without affecting the generality of the model. We set the maximum rate of synthesis of E-CAD to be equal to ν_E, the rate of natural E-CAD decay, so that in pluripotency the E-CAD level in each cell is 1. Likewise, we set the maximum rate of the WNT response to be equal to its degradation rate ν_W so that the WNT response varies from 0 to 1. We also assume, based on our evidence of direct induction of DKK1 by WNT (Figure 4) that this WNT response rate is a good approximation for the rate of DKK1 synthesis. The coefficient of W in equation (2) can be chosen to equal the degradation rate of W in (1) by adjusting the scale of I so we do not require a DKK1 specific synthesis rate. We do though let DKK1 have its own degradation rate ν_I.

Combining all of the above we obtain:

$$\frac{dW(r,t)}{dt}=\nu_W\frac{\theta_W^n}{\theta_W^n+I^n}-kEW-\nu_W W \qquad (1)$$

$$\frac{dI(r,t)}{dt}=D_I\nabla^2 I+\nu_W W-\nu_I I \qquad (2)$$

Development • Supplementary information

$$\frac{dE(r,t)}{dt} = D_E \nabla^2 E + \nu_E \left(\frac{\theta_E^m}{\theta_E^m + W^m} - E \right) \qquad (3)$$

Note that if we are purely interested in exploring the possible dynamics we could simplify this system further, rescaling the time for example so that $t = \tau * t_0$ with $t_0 = 1/\nu_W$. However, as we wish to use this model to fit our data, we need a match of the timescales between model and experiment, and hence we need to fit ν_W. Fortunately, we can get help in estimating its value since in the E-CAD$^{-/-}$DKK1$^{-/-}$ cell line the PDE system reduces to the one parameter equation:

$$\frac{dW(r,t)}{dt} = \nu_W (1 - W) \qquad (4)$$

A fit of the qPCR measured LEF1 response in small, unpatterned colonies of E-CAD$^{-/-}$DKK1$^{-/-}$ cells at various times results in a value of $\nu_W = 0.24/hr$ (Figure S8). The upper and lower 95% confidence bounds are 0.07 and $0.40/hr$. Since this estimate is based on mRNA data and so represents an upper limit, we restrict our search of possible ν_W values to be between 0.07 and $0.24/hr$. We find that the final best fit value is $\nu_W = 0.11/hr$, which means that $W(r,t)$ would reaches its half-maximal value ~6 hours after stimulation if the inhibition of E-CAD and DKK1 are not included.

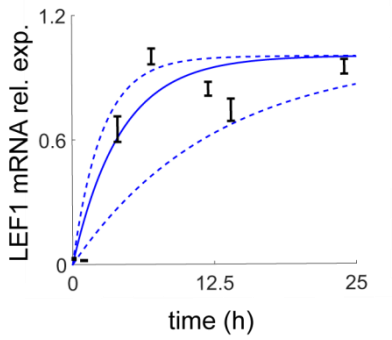

Figure S8: Solid line indicates best fit of LEF1 qPCR timecourse in unpatterned E-CAD$^{-/-}$DKK1$^{-/-}$ cells to Equation 4. Dashed lines indicate 95% confidence interval in the fit. $\nu_W = 0.24\ (0.07, 0.40)$. Error bars represent the standard deviation of three biological replicates.

2.1 Fitting DKK1 and WNT interaction with E-CAD$^{-/-}$ cell line

In the E-CAD$^{-/-}$ cell line the system reduces to just equations (1) and (2) with $E(r,\tau) = 0$. This leaves just 4 parameters to be fitted: n, θ_w, D_I and ν_I. This parameter space is small enough that we can perform a simple exhaustive grid search to find the global optima where the model WNT response curve at 12 and 48hrs matches the data at 12 hours (measured by LEF1) and 48 hours (measured by BRA or SOX17 in Figure 6, which is also equivalent to 1-SOX2) as calculated by a least squares fit. Where possible, this grid search was centered on biologically relevant values for variables, or from previous similar simulations[1].

Figure S9 shows the best fit to the data. The Hill parameter n can adjust the slope of the curve, but the effects of the other parameters are less obvious. To understand these effects we do two things: (1) we

Development • Supplementary information

perturb each parameter individually and see the change to the fit, and (2), we let the remaining parameters adapt to the perturbed parameter to see if and how the perturbation can be corrected. Doing this we can see for example that doubling D_I means that more cells on the boundary respond to WNT. Allowing the other parameters to vary while holding the doubled D_I constant, we can also see that decreasing ν_I can counteract this perturbation. This makes sense as increased D_I means more inhibitor is lost and decreasing ν_I counteracts this by making the inhibitor degrade less. The opposite is also true, since halving D_I means fewer cells on the boundary respond to WNT and this effect can be counteracted by increasing ν_I. For the WNT response threshold θ_w, we find that doubling it leads to less inhibitor and more differentiation, and that this can be counteracted by lowering the DKK1 degradation rate. Halving θ_w can conversely be counteracted by increasing ν_I. Taken together, these results imply that there is some redundancy between certain parameters in our model. This is not surprising as although we formulated our model to be minimal in the number of parameters, we also based it directly on the known biology and variables that could be easily perturbed. A more abstract model with a reduced number of variables might give more independent parameter estimates, but it would be harder to explore and relate to the fundamental biology at hand.

Perturbing the E-CAD$^{-/-}$ fit

	D_I (mm^2h^{-1})	ν_I (h^{-1})	θ_W
(1)	0.0024	0.0017	0.3000
(2)	0.0046	0.0017	0.3000
(3)	0.0046	0.0009	0.2073
(4)	0.0012	0.0017	0.3000
(5)	0.0012	0.0034	0.3628
(6)	0.0024	0.0850	0.3000
(7)	0.0022	0.0850	0.1893
(8)	0.0024	0	0.3000
(9)	0.0025	0	0.3045
(10)	0.0024	0.0017	0.5442
(11)	0.0013	0.0017	0.5442
(12)	0.0024	0.0017	0.1361
(13)	0.0050	0.0066	0.1361

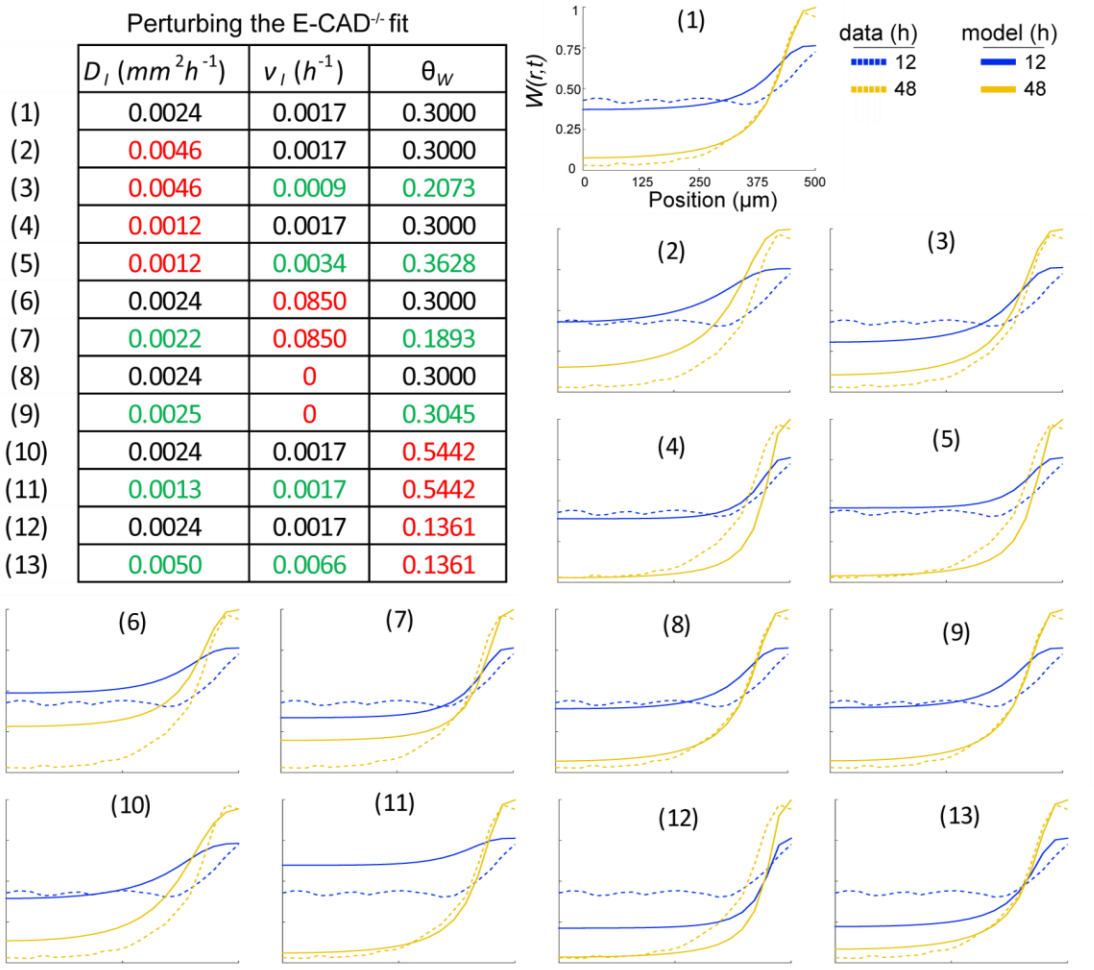

Development • Supplementary information

Figure S9: Fit of DKK1 specific parameters with E-CAD $^{-/-}$cell line, and parameter analysis using specific perturbations. Values in black in the table are the best fit parameters, values in red are the parameters specifically perturbed, and values in green are the new best fit parameters based on the perturbed parameter.

2.2 Fitting E-CAD and WNT interaction with DKK1$^{-/-}$ cell line

In the DKK1$^{-/-}$ cell line the system reduces to just equations (1) and (3), with $I(r,\tau)=0$. As can be seen when solving for $W(r,\tau)$ in equilibrium (see Equation 5), this system undergoes a super-critical pitchfork or "cusp" bifurcation to two different WNT states (Figure S9) depending on the choice of just 3 parameters: m, θ_E, and k.

$$\frac{1}{W}=\frac{k}{v_W}*\frac{\theta_E^m}{\theta_E^m+W^m}+1 \qquad (5)$$

More interestingly, it can be shown that, depending on initial conditions or boundary conditions, this system can admit traveling wave solutions that switch from the higher equilibrium state to the lower equilibrium state[7,8]. In 1D these waves travel with a unique shape and have a speed largely dependent on the coupling constant (here D_E) and time scale of E-CAD synthesis and degradation (v_E). Since in our case we have the boundary condition $E(R,t)=0$, then we can have the situation whereby WNT stimulation directs the periphery cells to a WNT "high" equilibrium state that is more stable than the WNT "low" equilibrium state that their more central neighbours are in. This creates an unstable boundary that can only be resolved by a travelling wave solution. By adjusting $m, \theta_E, k, v_E$and D_E ,we can moderate the speed and shape of the wave to fit the profile of WNT responsive cells in the DKK1$^{-/-}$ micropatterns at 12 hours (LEF1) and 48 hours (BRA and SOX17, as measured in Figure 6). As for the previous fit, this parameter space is sufficiently small enough that we can perform a grid search to find the global optima.

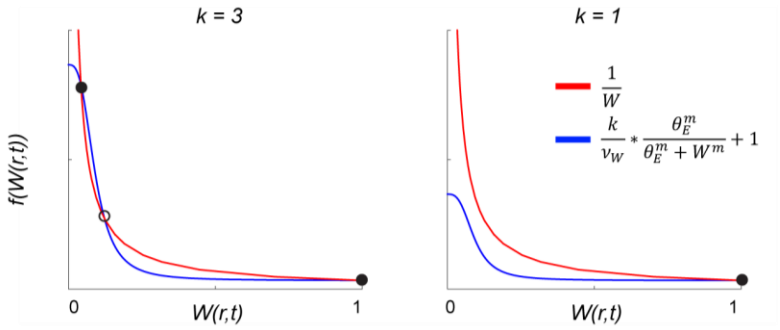

Figure S10: Examples of the cusp bifurcation in Equation 5 with different values of *k*. Solid circles mark stable points, open circles mark unstable points.

The best fit is shown in Figure S11. As for the DKK1 fit, the Hill parameter m can adjust the slope of the curve ($m=3$ in our fit), and to learn the effect of the other parameters we again use selected perturbations. As one might expect, increasing the coupling constant D_E increases the speed of the WNT response wave while decreasing it slows it down. This parameter has the largest effect on wave speed, though changing v_E , the effective turnover rate of E-CAD, also can modify speed since increasing it makes cells next in line in the wave respond faster once the wave reaches them. This can be noted in the perturbation analysis, as changing either D_E or v_E leads to a change in the other

variable to compensate for it. As one expects from Equation 5, θ_E and k are linked, so perturbing one leads to a correction from the other. Due to the non-linearity of the bifurcation they control they are also quite sensitive to perturbation, so just halving or doubling one leads to a collapse of the wave and one dominant state (i.e. either E-CAD is too strong and cells resist the WNT signal, or E-CAD is too weak and even a small WNT signal can downregulate it anywhere).

Perturbing the DKK1$^{-/-}$ fit

	D_E ($mm^2 h^{-1}$)	v_E (h^{-1})	θ_E	k
(1)	0.0043	8.0402	0.09005	2.4184
(2)	0.0086	8.0402	0.09005	2.4184
(3)	0.0086	30.0788	0.0272	9.0474
(4)	0.0021	8.0402	0.09005	2.4184
(5)	0.0021	67.0019	0.0367	6.0619
(6)	0.0043	8	0.09005	2.4184
(7)	0.0058	8	0.0272	9.0474
(8)	0.0043	4	0.09005	2.4184
(9)	0.0058	4	0.1650	1.2217
(10)	0.0043	8.0402	0.1801	20.1534
(11)	0.0332	6.0619	0.1801	1.2217
(12)	0.0043	8.0402	0.0450	20.1534
(13)	0.0045	0.0149	0.0450	6.0619
(14)	0.0043	8.0402	0.09005	4.8368
(15)	0.0548	100	0.0496	4.8368
(16)	0.0043	8.0402	0.09005	1.2092
(17)	0.0905	100	0.1650	1.2092

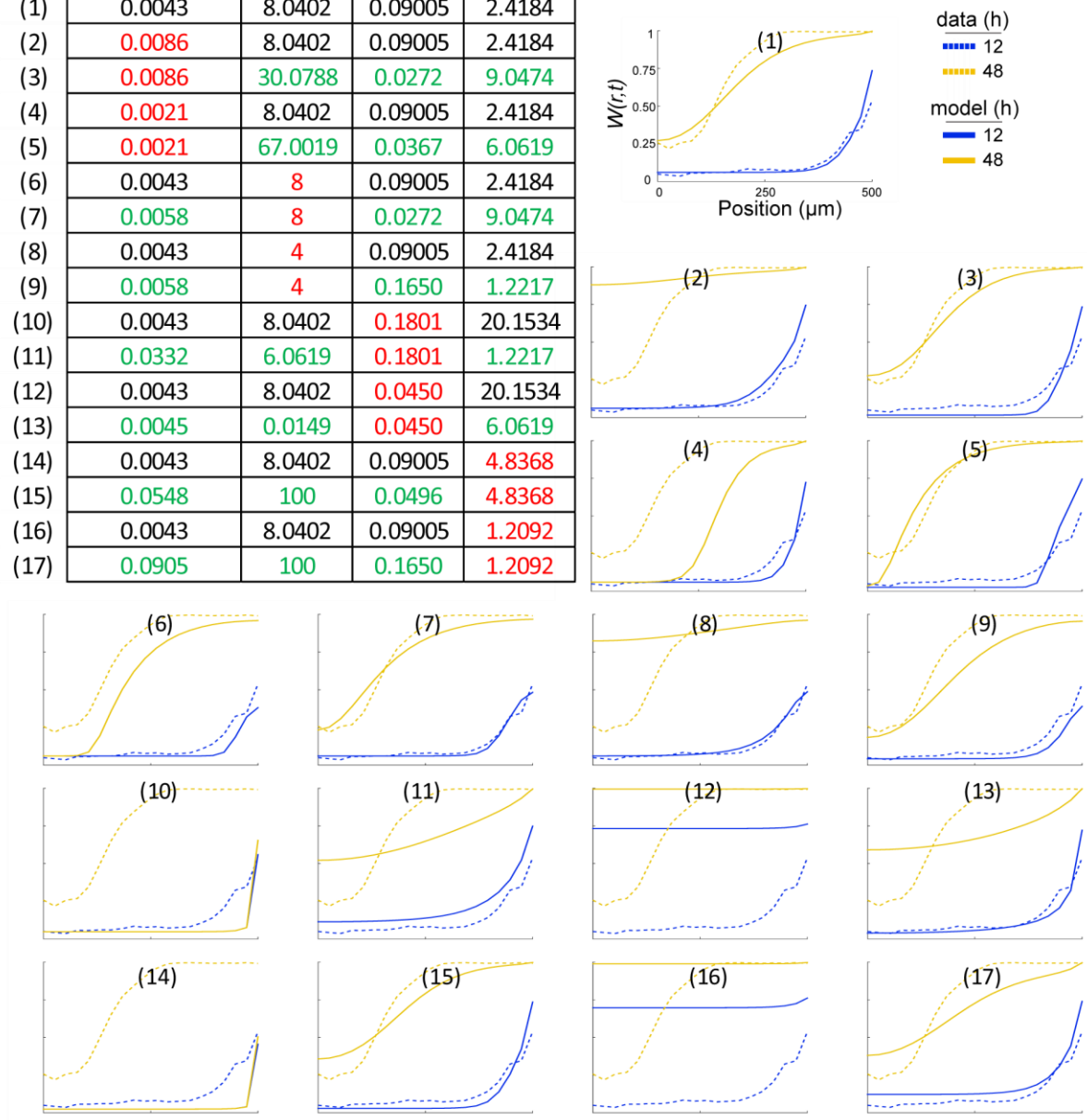

Figure S11: Fit of E-CAD specific parameters with DKK1$^{-/-}$ cell line, and parameter analysis using specific perturbations. Values in black in the table are the best fit parameters, values in red are the parameters specifically perturbed, and values in green are the new best fit parameters based on the perturbed parameter.

2.3 Applying fit to GLR:DKK1$^{-/-}$ time-lapse movie

As discussed in the main text, a further test of our fitted model was to apply it to our live-cell time-lapse GLR:DKK1$^{-/-}$ data. We found that though the model matches the data for the first 30 hours, beyond this there is a collapse of the inner SOX2 region that is quicker than what the model predicts (Figure S12). The agreement is a little better in a repeat of the experiment (Figure S12) but there is still a greater error between the model and these live cell data sets than the fixed antibody stained data we fit to. However the virtual disappearance of the SOX2 domain in the colony center at 72hrs is confirmed by the fixed data in Figure 6, which was not used in the fit. The difficulties in reproducing the movie data could entail the different dynamics of the live fluorescent reporter versus the LEF1 and the SOX2 stain, phototoxicity, or uncontrollable density differences.

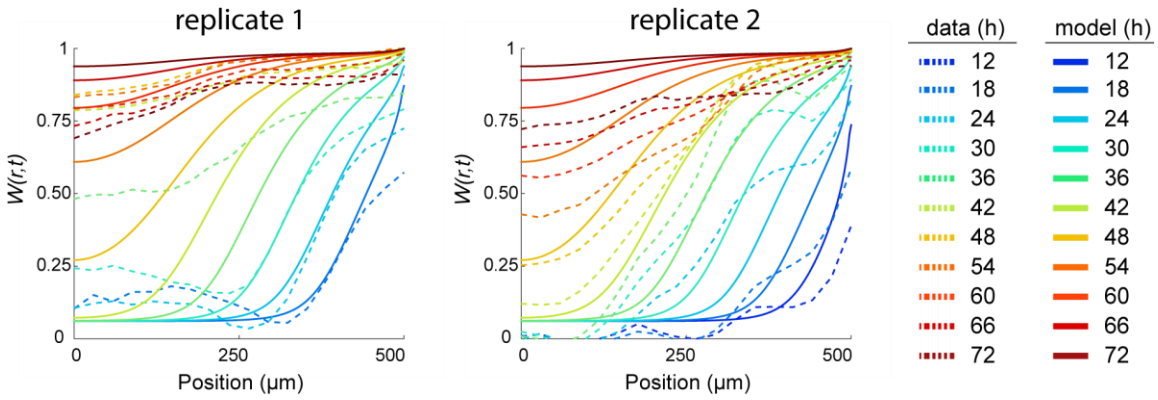

Figure S12: Comparison of the previously fitted model to two replicates of continuously imaged GLR:DKK1$^{-/-}$ micropatterns, the first replicate is an average of 7 colonies, the second replicate is an average of 10 colonies.

3 Mesoderm versus endoderm fate bifurcation

Having obtained the radial profile of differentiated cells from Eqs 1-3 for each cell line, the next question is whether these cells will commit to mesoderm (BRA) or endoderm (SOX17). In the anterior mouse primitive streak, these are two mutually exclusive states that are influenced mainly by the relative levels of WNT versus NODAL signalling, with more WNT signalling leading to mesoderm and more NODAL signalling leading to endoderm. The effect of NODAL signalling on endoderm fate choice was also shown in hESC micropatterns[9] in and reproduced in Fig 1A. Here we do not attempt to model the mechanism for this bistability or capture the dynamics. Instead, we simply let the choice depend on the ratio of WNT to NODAL signalling, letting the differentiated cells go to endoderm with probability $P(r)$ and going to mesoderm with probability $Q(r) = 1 - P(r)$. Since we are focused only on the fraction of cells at each radial position that differentiated, and in our model a differentiated cell is a cell that responded to the WNT signal, we assume that the WNT level is approximately the same across differentiated cells and thus a constant. NODAL signalling however is not the same for all cells, so we use measured nuclear SMAD2 levels for each cell line to approximate it (Figure 5 and Figure S13). Note

Development • Supplementary information

that we examine the SMAD2 levels at 24hrs rather than 48hrs, as 48hrs is too late and the fate decision has already been made. Thus our probabilities are

$$P(r) = \frac{NODAL(r)}{WNT(r) + NODAL(r)} = \frac{SMAD2_i(r) - b_1}{b_2 + (SMAD2_i(r) - b_1)} \quad (6)$$

$$Q(r) = \frac{WNT(r)}{WNT(r) + NODAL(r)} = 1 - P(r) \quad (7)$$

This effectively amounts to just a rescaled version of the measured SMAD2 profiles for each of our cell lines.

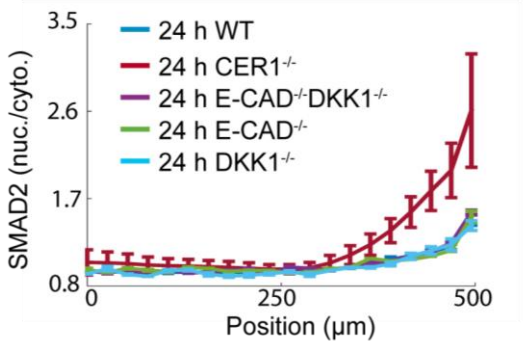

Figure S13: Radial profiles of nuclear SMAD2 in the cell lines modelled, n=20 colonies per condition.

4 Comparison of full model with data

Putting together the PDE system and the fate bifurcation parts of the model and comparing it to the measured SOX2, BRA, and SOX17 radial profiles at 48hrs for each cell line, we see that our model captures the data very well (Figure 7E). One obvious missing feature, however, is the dual SOX17 and BRA positive cell population. These are cells that express both markers and have not yet committed to one fate versus the other (though we expect they will as time progresses) and are found in most significant numbers in the DKK1$^{-/-}$ and E-CAD$^{-/-}$DKK1$^{-/-}$ cell lines. If forced to apportion this population to either mesoderm or endoderm, one can see that classifying them as mesoderm would give the better fit to the model. Interestingly the major exception to this is at the colony edges in the double knockout E-CAD$^{-/-}$DKK1$^{-/-}$ cell line, where doing so would lead the model to underestimate the number of BRA cells counted in the imaging. To further investigate this large discrepancy between the model and the data, we re-examined our E-CAD$^{-/-}$DKK1$^{-/-}$ micropattern data. We found that on the colony edge (and only on the colony edge) BRA cells sometimes lumped together in discrete clusters (Figure S14). As these clusters were immediately surrounded by a monolayer primarily composed of SOX17 cells, instead of the salt-and-pepper BRA or SOX17 pattern found further in the interior of the colony, we suppose that these clusters formed due to cell movement, i.e. cells were initially patterned in a stochastic manner but the BRA cells then moved and coalesced together while the SOX17 cells either stayed in place or underwent unbiased migration. That this only takes place on the edge of the E-CAD$^{-/-}$DKK1$^{-/-}$ micropatterns could be explained by noting that it is in this regime that cells are the least restricted from

moving, both by E-CAD and by existence of neighbours. The clusters are often quite 3 dimensional, and since our analysis involves just 2D segmentation on epifluorescence images, classification of cells in these clusters may be biased and introduce errors such as overcounting the number of SOX17/BRA cells. Migration was also not included in the model, and introducing a biased outward migration term for BRA cells for example might lead to an improved (though more complex) fit.

Overall, our model faithfully captures the E-CAD and DKK1 patterning dynamics as observed in our micropatterns and live-reporter lines, and in the most striking case where it does not, it still proves informative, pointing to a segregation and clustering of mesoderm versus endoderm cells that may be due to cell migration and merits further investigation.

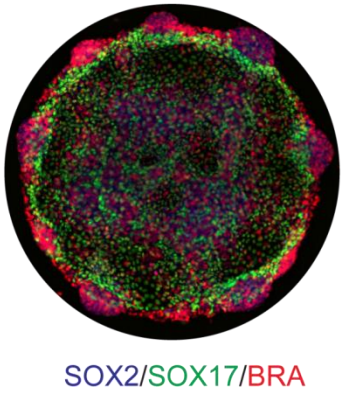

Figure S14: Example of an E-CAD$^{-/-}$DKK1$^{-/-}$ micropattern with BRA clusters on the periphery. The center remains a salt-and-pepper mix of SOX17 and BRA cells.

1. Etoc, F. *et al.* A Balance between Secreted Inhibitors and Edge Sensing Controls Gastruloid Self-Organization. *Dev. Cell* **39,** 302–315 (2016).

2. Libusova, L., Stemmler, M. P., Hierholzer, A., Schwarz, H. & Kemler, R. N-cadherin can structurally substitute for E-cadherin during intestinal development but leads to polyp formation. *Development* **137,** 2297–2305 (2010).

3. Cruciat, C. M. & Niehrs, C. Secreted and Transmembrane Wnt Inhibitors and Activators. *Cold Spring Harb. Perspect. Biol.* **5,** 39–64 (2013).

4. Arnold, S. J. & Robertson, E. J. Making a commitment: cell lineage allocation and axis patterning in the early mouse embryo. *Nat. Rev. Mol. Cell Biol.* **10,** 91–103 (2009).

5. Fagotto, F. Looking beyond the Wnt pathway for the deep nature of β-catenin. *EMBO Rep.* **14,** 422–33 (2013).

6. Kam, Y. & Quaranta, V. Cadherin-bound β-catenin feeds into the Wnt pathway upon adherens junctions dissociation: Evidence for an intersection between β-catenin pools. *PLoS One* **4,** (2009).

7. Fisher, R. A. The Wave of Advance of Advantageous Genes. *Ann. Eugen.* **7,** 355–369 (1937).

8. Tikhomirov, V. M. in *Selected Works of A. N. Kolmogorov: Volume I: Mathematics and Mechanics* (ed. Tikhomirov, V. M.) 242–270 (Springer Netherlands, 1991). doi:10.1007/978-94-011-3030-

Development • Supplementary information

1_38

9. Martyn, I., Kanno, T. Y., Ruzo, A., Siggia, E. D. & Brivanlou, A. H. Self-organization of a human organizer by combined Wnt and Nodal signalling. *Nature* **558,** 132–135 (2018).

Development • Supplementary information